2019

Entanglement complexity of quantum states, dynamics and quantum computation

BOSTON UNIVERSITY

GRADUATE SCHOOL OF ARTS AND SCIENCES

Dissertation

ENTANGLEMENT COMPLEXITY OF QUANTUM STATES, DYNAMICS AND QUANTUM COMPUTATION

by

ZHI-CHENG YANG

B.S., Peking University, 2013

Submitted in partial fulfillment of the

requirements for the degree of

Doctor of Philosophy

2019

Approved by

First Reader

Claudio Chamon, Ph.D.
Professor of Physics

Second Reader

Andrei Ruckenstein, Ph.D.
Professor of Physics

Acknowledgments

I am deeply indebted to my advisor, Claudio Chamon. Ever since the first day I started working with him, he has always been encouraging and willing to spend time discussing with me, in spite of the tons of other stuff he has to deal with. I still remember the early days when I was junior and immature in research, his open-mindedness and lack of even the tiniest bit of intellectual pretension helped me build confidence and encouraged me to always speak up, no matter how seemingly trivial or half-baked an idea is. His optimism, genuine curiosity and passion for scientific research have influenced me in a profound way, and led to my own commitment to an academic career. Apart from science, he sincerely cares about life and general wellbeing of his students, and is always able to guide me through the up and downs during my life as a PhD. Claudio has been an indispensible mentor of me.

I am also extremely lucky to have worked with many intelligent and responsible collaborators during my PhD. Eduardo Mucciolo and Alioscia Hamma guided me through the very first paper I wrote after I came to BU, as well as many subsequent collaborations, which contribute to the majority of this dissertation. Their insightful comments, patience and encouragement whenever I got anxious with research eventually led to the completion of these projects. Armin Rahmani and Alireza Shabani had brought my attention to variational quantum algorithms well before the majority of the community became interested in this direction, and generously shared their related expertise during our collaboration. Andrei Ruckenstein has always been supportive of me. His insightful remarks on various physics and non-physics topics as a senior scientist have shaped my opinions in an important way. I am grateful for the hospitality of Christopher Mudry during my visit at Paul Scherrer Institute. His high standard on the final presentation of every single project has greatly improved the overall quality of the paper. It has also been a pleasure working with Stefanos Kour-

tis, who is always hands-on in our projects and available to chat whenever there is something random on my mind. I have also learned a lot during seminars and various informal discussions from other faculty in the Physics Department, especially Anatoli Polkovnikov, Chris Laumann, Anushya Chandran, Ami Katz and Anders Sandvik.

An essential component leading to the maturity of a scientist is the discussions among peers. Over the past few years, I have benefited tremendously from countless interactions with my friends in physics, in particular: Meng Cheng, Stefanos Kourtis, Jyong-Hao Chen, Po-Hao Huang, Thomas Iadecola, Quntao Zhuang, Yi-Nan Wang, Zi-Wen Liu, Dries Sels, Constantin Schrade, Ruixing Zhang, Guanyu Zhu, Yi-Zhuang You, Xu Yang, Ya-Hui Zhang, Xiaoqi Sun, Yingfei Gu, Zhen Bi, Yizhi You, Xueyang Song, Jong-Yeon Lee and many others. Their insights and complementary expertise have broadened my knowledge and reshaped my tastes and viewpoints.

I would also like to thank the awesome Physics Department staff at BU, especially Mirtha Cabello and Anita Gupta, for their support and care during my stay here. My friends in the department, especially Lei Zhang, Mingzhu Cui, Jingjin Wei, Rashi Verma, Rajita Menon, Clover Su, Chon Kit Pun, Nathan Frey, Paul Hanakata, Yue Liu, Tianchi Chen, Bowen Zhao, Shan Huang, Marin Bukov, Phillip Weinberg, Manuel Buen Abad Najar, Tamiro Villazon Scholer, Ashish George, Alex Becker, Joe Boales, and many others have made my life at BU an enjoyable and unforgettable experience.

I am especially grateful to my special group of Chinese friends in Boston, the majority of whom are from my undergraduate university. In particular, Jiahua Guo, Chuteng Zhou, Jing Wang, Zheng Li, Quntao Zhuang, Yichen Zhang, Yi-Nan Wang, Xinmei Niu, Chris Chan, and Packard Chan. And also, my close friends ever since undergrad, Handuo Shi and Shenxiu Liu, although they are currently on the west coast of the country. I could hardly imagine PhD life in a foreign country without their

company over the past six years. Their everlasting love and friendship have always been the dearest to my heart. I would like to thank Tianyao Pei, whose genuine appreciation and respects for education and scientific research, as a successful person from a different field, have deeply impressed me and further strengthened my faith in an academic career.

Finally, I am grateful to my parents, for always being supportive and respect my choice at various important moments in my life. They were strict on me when I was a child so that I was able to benefit from the best educational resources in college, yet they gave me full freedom in choosing what I want to do later in my life. I would not have gotten this far in my life without their effort, love and wisdom.

ENTANGLEMENT COMPLEXITY OF QUANTUM STATES, DYNAMICS AND QUANTUM COMPUTATION

ZHI-CHENG YANG

Boston University, Graduate School of Arts and Sciences, 2019

Major Professor: Claudio Chamon, Ph.D., Professor of Physics

ABSTRACT

Quantum entanglement has become the key notion bridging originally distinct fields of research over the last decade, namely, quantum information and computation, condensed matter physics, and quantum gravity. Previous studies on quantum entanglement have largely focused on the entanglement entropy, which quantifies the amount of entanglement. However, a natural question arises: is there additional information of a quantum state that is not captured by the entanglement entropy alone? For ground states of gapped Hamiltonians, this question has been answered in the affirmative. In this dissertation, I extend this idea to study highly entangled states typically having volume law entropy, and demonstrate that there is indeed much richer information on the complexity of a quantum state beyond the entanglement entropy.

In the first part, I study the entanglement spectrum of highly entangled states corresponding to highly excited eigenstates of non-integrable Hamiltonians, time-evolved states after a quantum quench with Hamiltonians exhibiting different dynamical phases, and random unitary circuits consisting of random braids of non-Abelian anyons. I demonstrate that the entanglement spectrum is able to capture the degree of randomness of a quantum state, which we call the entanglement complexity.

In the context of scrambling, this quantifies the degree of randomness produced by scrambling beyond entropic diagnostics.

Our understanding of quantum entanglement in condensed matter systems and high energy physics have largely benefited from the field of quantum computation. In the second part of the dissertation, I present two examples of novel platforms for quantum computation using state-of-the-art experimental technologies. I demonstrate how one can use hybrid quantum-classical architecture to solve computational problems based on an optimal variational ansatz of the evolution protocol. I also present a hierarchical architecture of constructing logical Majorana zero modes which can be used for demonstrating non-Abelian braiding statistics experimentally.

Contents

List of Tables

List of Figures

List of Abbreviations

1D	.....	one dimension
AL	.....	Anderson localization
BdG	.....	Bogoliubov-de Gennes
EPR	.....	Einstein-Podolsky-Rosen
ETH	.....	eigenstate thermalization hypothesis
ES	.....	entanglement spectrum
ESS	.....	entanglement spectrum statistics
GOE	.....	Gaussian orthogonal ensemble
GUE	.....	Gaussian unitary ensemble
IPMM	.....	interior-point minimization method
KL	.....	Kullback-Leibler
MBL	.....	many-body localization
MC	.....	Monte Carlo
MZM	.....	Majorana zero mode
OTOC	.....	out-of-time-ordered correlator
QA	.....	quantum annealing
QAA	.....	quantum adiabatic algorithm
QAOA	.....	quantum approximate optimization algorithm
QMZM	.....	quasi-Majorana zero mode
QREM	.....	quantum random energy model
REM	.....	random energy model
RK	.....	Rokhsar-Kivelson
RMT	.....	random matrix theory
SK	.....	Sherrington-Kirkpatrick
SSETM	.....	scanning single-electron transistor microscopy
STM	.....	scanning tunnelling microscopy
SYK	.....	Sachdev-Ye-Kitaev
VQA	.....	variational quantum algorithm
VQE	.....	variational quantum eigensolver
WD	.....	Wigner-Dyson

Chapter 1

Introduction

The notion of quantum entanglement dates all the way back to the early stage of quantum mechanics. The existence of "spooky" nonlocal correlations between degrees of freedom at distance has led to skepticism and criticisms of quantum mechanics, until subsequent experimental tests of Bell's inequality supported its correctness [1, 2]. With the growing interest and developments in quantum information and quantum computation, various properties of quantum entanglement have been understood [3]. In this context, quantum entanglement quantifies the physical resources needed for quantum information processing. For example, quantum teleportation is possible only with the help of maximally entangled Einstein-Podolsky-Rosen (EPR) pairs [4].

It was not until slightly more than a decade ago when people realized that quantum entanglement may provide further insights into seemingly unrelated fields, such as quantum field theory and condensed matter physics [5]. Conventionally, a central topic of condensed matter physics is to understand and classify distinct phases of matter that emerge when a huge number of degrees of freedom are correlated via interactions. Defined as a measure of quantum correlations between different degrees of freedom, it turns out that the entanglement entropy of the ground state of a many-body Hamiltonian is able to identify novel phases of matter that cannot be classified by a local order parameter or its correlation functions [6, 7]. Moreover, quantum entanglement provides a measure of the number of parameters needed to simulate a given quantum state, which further inspired a plethora of powerful numerical ap-

proaches to study strongly-correlated systems, e.g. matrix product states and tensor network states [8–14].

The important role of quantum entanglement goes beyond equilibrium phenomena. The recent revival of the old subject of quantum chaos once again initiated a cross-fertilization among quantum information, condensed matter physics and high energy physics. Information scrambling in systems exhibiting chaotic behaviors can be partially captured by the growth of entanglement entropy under unitary evolution, which falls into different universality classes [15, 16]. It is believed that chaotic systems will eventually thermalize at late times under unitary evolution, and their properties at thermal equilibrium (e.g. expectation value of local operators) is encoded only in the *eigenstates*. This statement is known as the "Eigenstate Thermalization Hypothesis (ETH)" [17, 18]. Recent studies have unveiled a broad class of non-integrable models where ETH fails, which is now dubbed "many-body localization (MBL)" [19, 20]. As it turns out, thermalization and the lack thereof are also manifest in the entanglement growth behavior after a quantum quench [21].

The fontier of our understanding of quantum entanglement in non-equilibrium dynamics is currently expanding rapidly. While a lot has been known in terms of the entanglement entropy, the finer structure of entanglement beyond entropic diagnostics has remained unexplored until very recently. In particular, the entanglement spectrum (ES) of a given quantum state contains much richer information than the entropy alone, as was demonstrated for ground states [22]. In the context of non-equilibrium phenomena, one may thus expect that the ES also reveals more information of the underlying dynamics.

In this dissertation, we shall investigate the ES of highly-entangled states typically in non-equilibrium settings, as well as novel architectures and dynamical protocols for quantum computation. The first part of the dissertation discusses the ES of (1)

highly-excited eigenstates of Hamiltonians exhibiting a thermalization-to-MBL phase transition; (2) time-evolved states after a quantum quench with Hamiltonians exhibiting different dynamical phases; (3) random unitary circuits consisting of random braids on non-Abelian anyons. In the second part, we shall switch gears and present (1) designs of novel dynamical protocols based on optimal control theory to solve certain computational problems, and (2) a hierarchical construction of logical Majorana zero modes (MZMs) for topological quantum computation.

Below we present motivations and outline the structures and main results of each part separately.

1.1 Part I: Entanglement complexity of quantum states

In numerical simulations of many-body systems or computations, the amount of entanglement, or the entanglement entropy, often quantifies the amount of resources needed, e.g. in terms of the maximum bond dimensions of matrices in matrix product states [8, 23] or tensors in tensor network algorithms [14, 24–26]. In this sense, the entanglement entropy defines a notion of *complexity*. In the context of quantum chaos and scrambling, this is also the complexity generated by the underlying unitary evolution.

Indeed, completely random (or Haar random) states have nearly maximal entanglement entropy [27], for which approximations would require quantum circuits whose number of gates scale exponentially with the number of qubits [3]. However, the converse is not true: complexity is not all about the *amount* of entanglement. There exits ensembles of states that are not truly Haar random, yet still have nearly maximal entanglement entropy. A well-known example is the Clifford circuit, under which the entanglement entropy also reaches that of Haar random states [28] although the Clifford group does not generate a Haar random ensemble [3]. This indicates that

there must be a complexity gap between complete randomness and maximal entropy, which, in the context of quantum chaos, implies that scrambling can exhibit different complexities depending on the degree of randomness it produces. Recent progress suggests that the Rényi entropies could potentially be a measure of this additional complexity [29, 30].

The ES, defined as the full set of eigenvalues of the reduced density matrix, contains richer information than the entanglement entropy, a single number. Historically this was first realized in the study of ground states of gapped Hamiltonians with nontrivial topological orders [22]. More recently, the idea has been further extended to include highly excited eigenstates of thermalizing Hamiltonians [31], Floquet systems [32], and states evolved under random unitary circuits [28, 33]. In the first part of the dissertation, we study the density of states and level spacing statistics of the ES in different settings, and demonstrate that the deviation of the ES statistics from random matrix theory (RMT) quantifies the degree of randomness of a given quantum state, even at the same amount of entanglement entropy.

In Chapter 2, we focus on the density of states of the ES of highly excited eigenstates of generic non-integrable Hamiltonians in one dimension (1D). In particular, in the presence of quenched disorder, the Hamiltonians that we study typically undergo a dynamical phase transition from thermalization to MBL as the strength of disorder is increased. We find that the ES of highly-excited eigenstates shows a two-component structure: a universal part that is associated with RMT, and a nonuniversal part that is model dependent. The nonuniversal part manifests the deviation of the highly-excited eigenstate from a true random state even in the thermalized phase. We further use the fraction of the universal part of the ES to measure the degree of randomness of an eigenstate, and demonstrate that it gives good predictions of the location of the phase transition point.

Chapter 3 considers the ES of time-evolved states, i.e. states obtained after a quantum quench with a certain Hamiltonian. For different choices of parameters, the Hamiltonian that we study exhibits three different dynamical phases: Anderson localization, thermalization and MBL. We look at the ES level spacing statistics at long enough times when the entanglement entropy saturates. We find that the ES displays a Poisson distribution for the Anderson localization case, and a Wigner-Dyson (WD) distribution for both thermalization and MBL. We argue that the different ES distributions defines a notion of *entanglement complexity*, which can be probed by whether or not it is possible to efficiently *disentangle* a given time-evolved state without precise knowledge of the time evolution operator.

Based on the definition of entanglement complexity in Chapter 3, Chapter 4 further quantifies this complexity in terms of the degree of randomness produced by a given unitary dynamics, and studies the *dynamics* of the ES under time evolution. In particular, we define the Kullback-Leibler (KL) divergence between the ES level spacing distribution and the WD distribution as a measure of the degree of randomness, and apply this measure to quantum circuits consisting of random braids of non-Abelian anyons. We show that there is indeed a hierarchy of entanglement complexity produced by different dynamics at the same amount of entanglement entropy, as is revealed by the KL divergence.

1.2 Part II: Novel architectures for quantum computation

Our understanding of quantum entanglement and operator spreading has largely benefited from ideas in quantum computation. For example, a wealth of analytical results are accessible by considering quantum circuit models [15, 16, 34, 35]. Quantum computation aims at utilizing quantum mechanics to solve problems that are intractable classically. In spite of the surge of interests and advances in quantum computation

over the past decade, building a full-fledged universal quantum computer would likely require significant advances in both theoretical understanding and experimental technologies. In Part II of the dissertation, I present two examples of novel platforms for quantum computation using state-of-the-art experimental technologies.

In addition to circuit model quantum computation, there exists an alternative platform known as the "Quantum Adiabatic Algorithm (QAA)" [36]. QAA directly makes use of the adiabatic theorem in quantum mechanics, which states that for sufficiently slow evolution under a time-dependent Hamiltonian starting from the initial ground state, the system will remain close to its instantaneous ground state. The total evolution time for the adiabatic theorem to hold, and hence the complexity of the algorithm, is controlled by the minimum energy gap along the evolution path. It has been shown that QAA is equivalent to circuit model quantum computation [37]. However, the advantage of the QAA over the best up-to-date classical algorithms has remained unclear so far [38]. When applied to typical NP-complete problems, it turns out that the system often undergoes a first-order transition into a glassy phase, which yields an exponentially small energy gap either at the phase transition or due to avoided crossings within the glassy phase and hence an exponential scaling of time-to-solution [39–43].

Upon realizing the limitations of QAA, a number of groups proposed alternative time evolution protocols that do not require adiabaticity. Quite surprisingly, for certain hard instances of problems, fast, nonadiabatic protocols can outperform QAA [44, 45]. Further explorations along the line of thinking have led to several systematic algorithms in contrast to QAA, namely, Quantum Approximate Optimization Algorithm (QAOA) [46], Variational Quantum Algorithm (VQA) [47–51], and counterdiabatic drivings [52], etc.

In Chapter 5, we prove that the optimal time evolution protocol for a given total

time generically has a bang-bang form, which coincides with the protocol of QAOA. The proof is a direct consequence of the Pontryagin's minimum principle in optimal control theory. We further demonstrate the optimality of the bang-bang protocol by applying it to the Sherrington-Kirkpatrick spin glass model [53]. This protocol is an example of the more general VQA, which can be implemented on a near-term hybrid quantum-classical device.

Another route towards quantum computing is the so-called topological quantum computation [54]. In topological quantum computation, qubits are built out of non-Abelian anyons of topologically ordered systems. Unitary operations on a given state is implemented via braiding of non-Abelian anyons. Due to the topological nature of the systems hosting such anyons, this platform is less prone to decoherence from local perturbations or coupling to the environment. So far, one of the most promising platforms for topological quantum computing the the MZMs at the endpoints of superconductor-proximitized semiconductor nanowires [55]. However, in spite of the tremendous experimental progress on probing the existence of such MZMs, there remains the important open question of demonstrating their non-Abelian fusion and braiding statistics.

In Chapter 6, we present a hierarchical architecture for building logical MZMs using physical MZMs at the Y-junctions of a hexagonal network of semiconductor nanowires. This has the advantage of being fully tunable by gating the individual wires. We demonstrate that selecting the gate voltages that generate a Kekulé pattern in the hybridization of the MZMs at opposite endpoints of a wire yields an emergent "logical" MZM bound to the vortex core. The position of a logical Majorana can be tuned adiabatically by programming the gate voltages to change as a function of time, thereby demonstrating non-Abelian braiding statistics.

Part I: Entanglement complexity of quantum states

Chapter 2

Two-component structure in the entanglement spectrum of highly-excited states

Abstract

We study the entanglement spectrum of highly excited eigenstates of two known models that exhibit a many-body localization transition, namely the one-dimensional random-field Heisenberg model and the quantum random energy model. Our results indicate that the entanglement spectrum shows a "two-component" structure: a universal part that is associated with random matrix theory, and a nonuniversal part that is model dependent. The nonuniversal part manifests the deviation of the highly excited eigenstate from a true random state even in the thermalized phase where the eigenstate thermalization hypothesis holds. The fraction of the spectrum containing the universal part decreases as one approaches the critical point and vanishes in the localized phase in the thermodynamic limit. We use the universal part fraction to construct an order parameter for measuring the degree of randomness of a generic highly excited state, which is also a promising candidate for studying the many-body localization transition. Two toy models based on Rokhsar-Kivelson type wave functions are constructed and their entanglement spectra are shown to exhibit the same structure.[1]

[1]The contents of this chapter were published in Physical Review Letters, **115**, 267206 (2015).

2.1 Introduction

Quantum entanglement, a topic of much importance in quantum information theory, has also gained relevance in quantum many-body physics in the past few years [56, 57]. In particular, the entanglement entropy provides a wealth of information about physical states, including novel ways to classify states of matter that do not have a local order parameter [58, 59]. However, it has been realized only recently in various physical contexts that the entanglement entropy is not enough to fully characterize a generic quantum state. For example, the quantum complexity corresponding to the geometric structure of black holes cannot be fully encoded just by the entanglement entropy [60]. One natural step beyond the amount of entanglement is the specific pattern of entanglement, i.e., the entanglement spectrum. A recent result that motivates this direction is the relationship between irreversibility and entanglement spectrum statistics in quantum circuits [28, 33]. It was shown that irreversible states display Wigner-Dyson statistics in the level spacing of entanglement eigenvalues, while reversible states show a deviation from Wigner-Dyson distributed entanglement levels and can be efficiently disentangled.

Are there universal features in the entanglement spectrum of a generic eigenstate of a quantum Hamiltonian? Highly excited eigenstates of a generic quantum Hamiltonian are believed to satisfy the "eigenstate thermalization hypothesis" (ETH) [17, 18, 61], which states that the expectation value $\langle\psi_\alpha|\hat{O}|\psi_\alpha\rangle$ of a few-body observable $\hat{O}$ in an energy eigenstate $|\psi_\alpha\rangle$ of the Hamiltonian with energy E_α equals the microcanonical average at the mean energy E_α. So one could as well ask the following question: What is the structure of the entanglement spectrum of highly excited eigenstates of a thermalized system? Here we find a quandary. Completely random states are generically not physical, namely, they cannot be the eigenstates of Hamiltonians with local interactions. For the ETH to be a physical scenario for ther-

malization, highly excited eigenstates of physical local Hamiltonians cannot always be completely random, yet they have to contain enough entropy. Deviations from a completely random state can be quantified by the entanglement entropy, more precisely by the amount that it deviates from the maximal entropy in the subsystem, derived by Page, which we will refer to as the Page entropy hereafter [27]. But are there features that cannot be captured by the entanglement entropy alone? Can one identify remnants of randomness in the full entanglement spectrum? What about in states that violate the ETH?

In this chapter, we address the above questions using as a case study the problem of many-body localization (MBL) [19–21, 62, 63]. We study two known models that were shown to exhibit a MBL transition, namely, the Heisenberg spin model with random fields, and the quantum random energy model (QREM) [64–66]. In the delocalized phase, high-energy eigenstates are thermalized according to the ETH. The deviation from completely random states manifests itself in a "two-component" structure in the entanglement spectrum: a universal part that corresponds to random matrix theory[67], and a nonuniversal part that is model dependent. We show that the universal part fraction decreases as one approaches the transition point and vanishes in the localized phase in the thermodynamic limit. We therefore propose an order parameter that is able to measure the degree of randomness of a generic highly excited state and capture the many-body localization-delocalization transition based on the entanglement spectrum, and show that it gives predictions consistent with previous results. We further construct two toy models in terms of Rokhsar-Kivelson- (RK) type wavefunctions [68, 69] and the same structure in the entanglement spectra is observed.

2.2 Heisenberg spin chain

A well-studied model that shows a MBL transition is the isotropic Heisenberg spin-1/2 chain with random fields along a fixed direction,

$$\mathcal{H} = \sum_{i=1}^{L} \left(h_i \, S_i^z + J \, \vec{S}_i \cdot \vec{S}_{i+1} + \Gamma S_i^x \right), \tag{2.1}$$

where the random fields h_i are independent random variables at each site, drawn from a uniform distribution in the interval $[-h, h]$. Γ is a uniform transverse field along the x direction, which breaks total S_z conservation. We assume periodic boundary condition and set the coupling $J = 1$ and $\Gamma = 0.1$. In the absence of the transverse field Γ, previous work located the critical point at $h = h_c \approx 3.5$ in the $S_z = 0$ sector [19, 70]. We consider two different regimes by varying the disorder strength parameter h: (i) within the thermalized phase ($h < h_c$), and (ii) in the localized phase ($h > h_c$). In each regime, we focus on eigenstates of Hamiltonian (5.9) at the middle of the spectrum, namely, on highly excited states.

We consider a bipartition of the system into subsystems A and B of equal size ($L/2$ sites each). For a generic eigenstate $|\psi\rangle = \sum_{\boldsymbol{\sigma}} \psi(\boldsymbol{\sigma})|\boldsymbol{\sigma}\rangle$, where $\boldsymbol{\sigma} \equiv \sigma_1 \sigma_2 \ldots \sigma_L$ labels the 2^L possible spin configurations of the system, we cast the wave function as $\psi(\boldsymbol{\sigma}) \equiv \psi(\boldsymbol{\sigma}_A \, \boldsymbol{\sigma}_B)$, where $\boldsymbol{\sigma}_A \equiv \sigma_1 \ldots \sigma_{L/2}$ and $\boldsymbol{\sigma}_B \equiv \sigma_{L/2+1} \ldots \sigma_L$. The entanglement spectrum is obtained from the eigenvalues of the reduced density matrices $\rho_A = \mathrm{tr}_B |\psi\rangle\langle\psi|$ and $\rho_B = \mathrm{tr}_A |\psi\rangle\langle\psi|$: $\{p_k = \lambda_k^2\}, k = 1, \ldots 2^{L/2}$. In this work, we are primarily concerned with the density of states and level statistics of the $\{\lambda_k\}$ for highly excited eigenstates for different strengths of disorder. For each value of h analyzed, the spectra were averaged over 10 realizations of disorder for $L = 16$, and 100 realizations for $L = 14$. For each spectrum, the eigenstate with energy closest to zero was obtained by a Lanczos projection [71]. This eigenstate corresponds to a highly excited state.

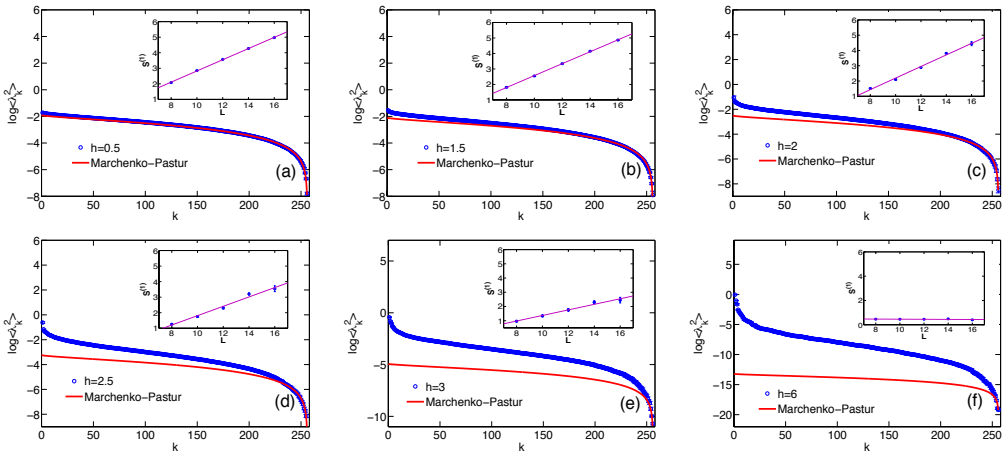

Figure 2·1: (Color online) Average entanglement spectrum of highly excited eigenstates for a system of size $L = 16$, averaged over 10 realizations of disorder (plotted in logarithmic scale). Panels a–f show the spectrum for $h = 0.5, 1.5, 2, 2.5, 3$ and 6, respectively. The solid lines correspond to the spectrum of a completely random state (derived from a Marchenko-Pastur distribution), and is shown for reference. Insets: scaling of the average entanglement entropy $S^{(1)}$ with system size.

2.3 Thermalized phase

We start by considering the weakly disordered case, $h \ll h_c$. Only a small amount of disorder is necessary to break the integrability of the clean Hamiltonian. However, conservation of the total S_z also plays a crucial role in making eigenstates completely random. A small transverse field Γ is applied to break this conservation without substantially altering the many-body localization transition. In this regime, we find that the entanglement spectrum of the highly excited state with eigenenergy near zero is close to that of a completely random quantum state, as shown in Fig. 2·1(a) for systems of size $L = 16$ and $h = 0.5$. The entanglement spectrum follows closely a Marchenko-Pastur distribution (with proper normalization), which describes the asymptotic average density of eigenvalues of a Wishart matrix [72, 73]. (The expression for the entanglement spectral density for the random state is presented in the Appendix) One can also check that, in this regime, the von Neumann entanglement

entropy $S^{(1)} = -\sum_k p_k \ln p_k$ is in good agreement with the Page entropy for random states: $S_{m,n} = \sum_{k=n+1}^{mn} \frac{1}{k} - \frac{m-1}{2n} \approx \ln(m) - \frac{m}{2n}$, where m and n are the Hilbert space dimensions of subsystem A and B, respectively [27]. For example, our computed average entropy for 16 sites is $\langle S^{(1)} \rangle = 4.9719 \pm 0.0015$, while the corresponding Page entropy is $S_{\text{Page}} = 5.0452$.

As the disorder strength is increased, but still $h < h_c$, the system remains in the thermalized phase where it is supposed to obey the ETH and yield volume-law scaling of the entanglement entropy with system sizes [74], which is verified in the insets of Figs. 2·1(a) to 2·1(e). However, in spite of the volume-law scaling of the entanglement entropy and the thermalization of eigenstates, the entanglement entropy is much lower than the Page entropy. This indicates that the pattern of entanglement must have changed, which is manifest in the spectra shown in Figs. 2·1(b) to 2·1(e). The entanglement spectrum shows a striking "two-component" structure: (i) a universal tail in agreement with random matrix theory, and (ii) a nonuniversal part. The non-universal part dominates the weights in the spectrum (large λ_k values), resulting in low entanglement entropy, as it decays much faster than the universal part. Therefore, we find that although thermalized states are not necessarily random states, they partially retain a component that is reminiscent of a random state: the entanglement spectrum follows the Marchenko-Pastur level density distribution. In addition, the universal part of the entanglement spectrum follows a Wigner-Dyson distribution of level spacings (see the Appendix).

2.4 Localized phase

In this regime, the entanglement entropy exhibits an area-law scaling with the system size [see inset of Fig. 2·1(f)], which in one spatial dimension implies a constant entropy and, at most, weakly logarithmic corrections, in accordance with Ref. [75].

The entanglement spectrum in the localized regime, depicted in Fig. 2·1(f) for $h = 6$, shows a different scenario from that in the thermalized phase: the universal part of the spectrum disappears completely, leaving only the nonuniversal part characterized by its fast decay rate.

2.5 QREM

The QREM describes L spins in a transverse field Γ with the following Hamiltonian:

$$\mathcal{H} = E(\{\sigma^z\}) + \Gamma \sum_{i=1}^{L} \sigma_i^x \tag{2.2}$$

where $E(\{\sigma^z\})$ is the classical REM term that takes independent values from a Gaussian distribution of zero mean and variance $L/2$ [76]. This model was first studied in the context of a mean-field spin glass, and was shown to exhibit a first-order quantum phase transition as a function of Γ [64]. More recently, it was further demonstrated to have a MBL transition when viewed as a closed quantum system [65]. Numerical and analytical arguments show that the transition happens at an energy density $|\epsilon| = \Gamma$ in the microcanonical ensemble. Since there is no support for the many-body localized phase at energy density $\epsilon = 0$, we examine the eigenstates with energy density closest to $\epsilon = 0.5$ instead, and study the entanglement spectrum as Γ is tuned. The two-component structure and its evolution as a function of Γ similar to Fig. 2·1 are again observed (see the Appendix).

2.6 An order parameter

The above picture unveils a new aspect of the MBL transition. The two parts of the entanglement spectrum of a highly excited state clearly evolve as the disorder strength h is increased, namely, the universal part shrinks and the nonuniversal part grows. This fact suggests that one could use the fraction of each component as an

order parameter.

Figures 2·1(a) to 2·1(e) indicate an h dependent value k_h that separates the nonuniversal ($k \leq k_h$) from the universal ($k > k_h$) parts of the rank-ordered entanglement levels (see the Appendix for the protocol for determining k_h). One can thus define the partial Rényi entropies

$$S_{\leq}^{(q)} = \frac{1}{1-q} \ln \sum_{k \leq k_h} p_k^q \, , \tag{2.3}$$

with $q \geq 0$. Because the universal part of the spectrum is where the eigenvalues with low entanglement reside, this part of the spectrum is obscured by any measure that relies on the eigenvalues as weights. A good measure of the fraction of the two components that does not depend on these weights is given by the $q = 0$ Rényi entropy, which simply measures the ranks: $S_{\leq}^{(0)} = \ln k_h$. Therefore, an order parameter that measures the fraction of the universal component is

$$\mathcal{O}_{\mathrm{MBL}} = 1 - \frac{S_{\leq}^{(0)}}{S^{(0)}} = 1 - \frac{\log_2 k_h}{L/2} \, . \tag{2.4}$$

Figure 2·2 shows the order parameter as defined above for the Heisenberg spin model and the QREM, respectively. For the QREM, all curves at different system sizes cross at $\Gamma_c \approx 0.5$, in excellent agreement with Ref. [65]. We have also looked at energy density $\epsilon = 0.3$, and the curves cross at $\Gamma_c \approx 0.25$, giving the same numerical prediction as in Refs. [65] and [66] (plot shown in the Appendix). For the random-field Heisenberg model, however, the fact that the transition happens at the point where the order parameter is nearly zero makes it harder to accurately locate the critical point using our order parameter. We see from Fig. 2·2 that the curves cross at $h_c \approx 3.3$, which is also consistent with previous studies. This indicates that, by considering the full entanglement spectrum at high energies, our order parameter reveals a novel property that is promising for studying the MBL transition.

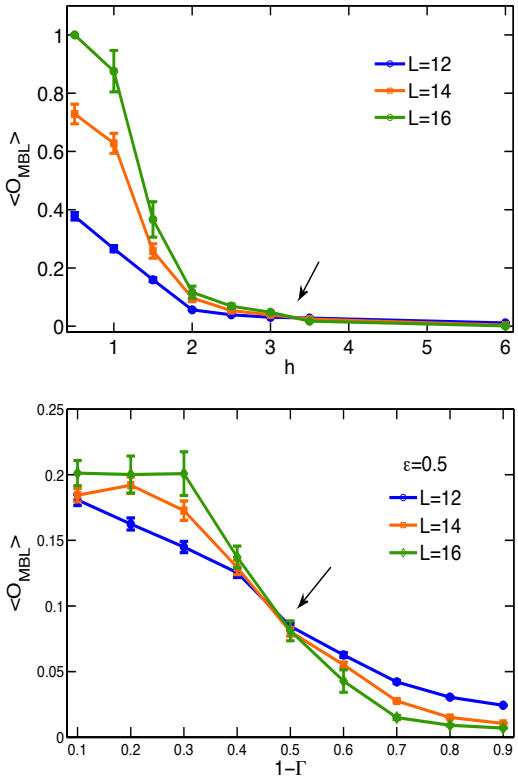

Figure 2·2: (Color online) The order parameter defined as the fraction of the universal component in the full entanglement spectrum for the Heisenberg spin model (upper panel) and the QREM (lower panel).

We remark that, although the MBL transition can also be captured by the scaling property of the entanglement entropy, our order parameter seems to be applicable even for models with nonlocal interactions, which could obscure the connection between the volume-to-area law transition of the entropy and the MBL transition.

2.7 Toy models

We construct two RK-type model wave functions that are shown to have (i) the two-component structure in their entanglement spectra, and (ii) a phase transition as a

function of the tuning parameter. The wave functions take the following form:

$$|\Psi\rangle = \frac{1}{\sqrt{\mathcal{Z}}} \sum_{\boldsymbol{\sigma}} s_{\boldsymbol{\sigma}} \mathrm{e}^{-\frac{\beta}{2} E(\boldsymbol{\sigma})} |\boldsymbol{\sigma}\rangle, \tag{2.5}$$

where $E(\boldsymbol{\sigma})$ is the energy for the classical configuration $\boldsymbol{\sigma}$ and $\mathcal{Z}$ is the corresponding partition function of the classical statistical system [69]. $s_{\boldsymbol{\sigma}}$ is a random sign for each configuration, such that the wave function represents a highly excited state. We consider the following two cases: (i) $E(\boldsymbol{\sigma}) = E_{\mathrm{REM}}(\boldsymbol{\sigma})$, and (ii) $E(\boldsymbol{\sigma}) = -\frac{J}{L}\sum_{i<j}\sigma_i^z\sigma_j^z$. In the first case, the energy is taken to be that of the REM, while in the second case the energy is that of an infinite-range uniform ferromagnetic interaction.

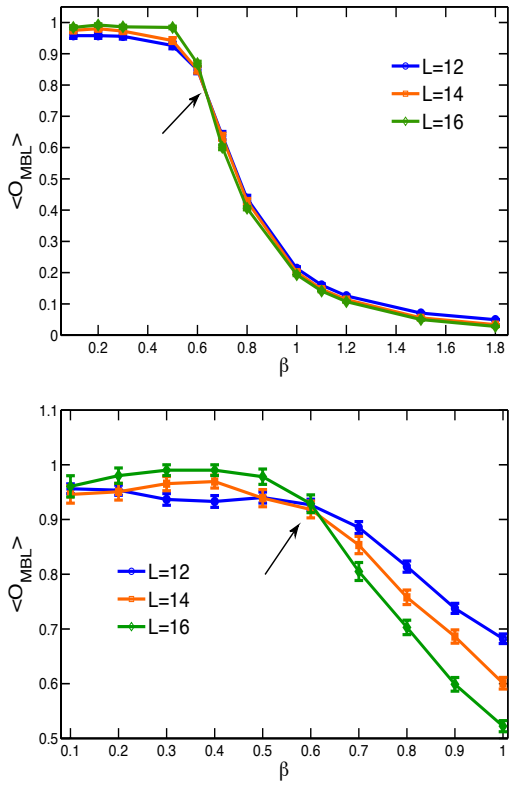

Figure 2·3: (Color online) The order parameter for the random-sign RK-type wave functions. Upper panel: $E(\boldsymbol{\sigma}) = E_{\mathrm{REM}}(\boldsymbol{\sigma})$. Lower panel: $E(\boldsymbol{\sigma}) = -\frac{J}{L}\sum_{i<j}\sigma_i^z\sigma_j^z$, with $J = 1$.

In the small β regime, the above RK-type wave functions are close to completely

random states; upon increasing β, the wave functions are pushed towards product states and start to deviate from completely random states. Therefore, the tuning parameter β here plays the role of the "disorder strength". Indeed, we find the same two-component structure in the entanglement spectrum (see the Appendix), and the order parameter is shown in Fig. 2·3. The REM case was recently studied by Chen *et al.* where the MBL transition was obtained numerically using other measures [77]. Here we clearly see that, in both cases, the curves cross at some critical β, indicating the existence of a similar phase transition.

2.8 Summary and discussion

The details of the structure of the entanglement spectrum, especially the universal part at the tails of the spectrum, have long been overlooked. The main focus has been primarily on the dominating nonuniversal component, and the universal tail has thus far been discarded. For example, in the density matrix renormalization group [8] and tensor network methods [9, 13, 78, 79], the density matrix is truncated to avoid uncontrolled growth of its dimensions. While this procedure is certainly justified when the purpose is to obtain ground state properties, it discards important information about the behavior of the system at higher energy states. In this chapter we showed that the full entanglement spectrum, directly computable from the wave function, provides information that is often invisible in the entanglement entropy alone.

On the other hand, much has been known about random quantum states, e.g., the Page entropy and volume-law scaling entropy. Nevertheless, the Page entropy is often an overestimate of the actual entanglement entropy computed from generic quantum states. Therefore, a natural question that arises is as follows: How random does a given quantum state look? In this chapter, we show that a generic quantum state that satisfies ETH does not necessarily mean a completely random state. We

present an order parameter to quantify the degree of randomness by using information about the full entanglement spectrum. In the context of MBL, our order parameter is able to locate the critical point, consistent with previous results. Our work may provide a novel way of studying MBL, and may shed new light on the understanding many-body systems at the level of wave functions.

Acknowledgments

Z.-C.Y. is indebted to Bernardo Zubillaga, Alexandre Day, Shenxiu Liu, and Yi-Zhuang You for generous help and useful discussions. We thank Christopher Laumann for useful comments.

A Marchenko-Pastur distribution and random states

The Marchenko-Pastur distribution describes the asymptotic (large-N) average density of eigenvalues of an $N \times N$ matrix of the form $Y = XX^\dagger$, known as a Wishart matrix, where X is a $N \times M$ random rectangular matrix with independent but identically distributed entries [72]. Let σ^2 be the variance of the entries in X. When $N = M \to \infty$, the Marchenko-Pastur distribution takes the form

$$\mathcal{D}(p) = \left\langle \frac{1}{N} \sum_{k=1}^{N} \delta(p - p_k) \right\rangle_{N\to\infty} = \frac{2}{\pi p_{\max}} \sqrt{\frac{p_{\max}}{p} - 1}, \tag{6}$$

where $\{p_k\}$ are the eigenvalues of Y, $0 \leq p \leq p_{\max}$ and $p_{\max} = 2\sigma^2$. From this distribution we can obtain the average number function associated to the eigenvalues

of Y. Let $p_1 \geq p_2 \geq \cdots \geq p_N$ and $\eta_k = k/N$. Then,

$$\begin{aligned}
\eta(p) &= 1 - \left\langle \frac{1}{N} \sum_{k=1}^{N} \theta(p - p_k) \right\rangle_{N\to\infty} && (7)\\
&= \left[1 - \int_0^p dp'\, \mathcal{D}(p') \right] && (8)\\
&= \int_p^{p_{\max}} dp'\, \mathcal{D}(p') && (9)\\
&= 1 - \frac{2}{\pi} \left[u\sqrt{1-u^2} + \arcsin(u) \right]_{u=\sqrt{p/p_{\max}}}. && (10)
\end{aligned}$$

Thus, introducting the rescaled variable $x = \sqrt{p/p_{\max}}$, we find

$$\eta(x) = 1 - \frac{2}{\pi} \left[x\sqrt{1-x^2} + \arcsin(x) \right]. \tag{11}$$

It is straightforward to relate the average number function derived from the Marchenko-Pastur distribution with that obtained from the entanglement spectrum of a bipartitioned random vector. Let $\psi(x_A, x_B)$ be the wavefunction of the bipartite system. Then, the reduced density matrix is given by

$$\rho_A(x_A, x'_A) = \sum_{x_B} \psi(x_A, x_B)\, \psi^*(x'_A, x_B). \tag{12}$$

We can see that, for completely random wavefunctions, the reduced density matrix is a random Wishart matrix and therefore its eigenvalues should follow a Marchenko-Pastur distribution[73]. Thus, we expect the average number function to provide an accurate description of the average spectrum.

Let $\{p_k\}$, $k = 1, \ldots, d$, be the set of eigenvalues of ρ_A in decreasing order, with $p_k \geq 0$, $\sum_{k=1}^{d} p_k = 1$, and $d \leq 2^{L/2}$. It is straightforward to relate the eigenvalues $\{p_k\}$ to the singular values $\{\lambda_k\}$ resulting from the Schmidt decomposition of the

bipartite wavefunction,

$$\psi(x_A, x_B) = \sum_{k=1}^{d} \lambda_k \, \phi_A^{(k)}(x_A) \, \phi_B^{(k)}(x_B), \tag{13}$$

by simply setting $p_k = \lambda_k^2$ (notice that $\lambda_k \geq 0$), where $\phi_A^{(k)}(x_A)$ and $\phi_B^{(k)}(x_B)$ are the left-singular and right-singular vectors, respectively. For the purpose of comparing the average spectra to Eq. (11), it is necessary to rescale the singular values and their indices as follows:

$$p_k = \frac{4}{d} x^2(\eta_k) \tag{14}$$

where $x(\eta)$ is the inverse function of $\eta(x)$. The prefactor is chosen to guarantee the normalization of p_k:

$$\begin{aligned} \sum_{k=1}^{d} p_k &\rightarrow 4 \int_0^1 \mathrm{d}\eta \, x^2(\eta) \\ &= \frac{16}{\pi} \int_0^1 \mathrm{d}x \, x^2 \sqrt{1 - x^2} \\ &= 1. \end{aligned} \tag{15}$$

We tested this formulation by plotting the numerical results for p_k obtained from a random state against the analytical expression in Eq. (11). Figure ·4 shows $\eta_k = \frac{k}{d}$ versus $x_k = \frac{1}{2}\sqrt{p_k d}$. There is very good agreement with the analytical prediction.

Notice that in the cases considered in the main text, the random part of the entanglement spectrum alone is not normalized. However, by plotting $\log \lambda_k$ versus k, the missing normalization factor only amounts to a trivial shift of the entire spectrum.

B Level spacing statistics

We studied the statistics of the entanglement spectrum by looking at the level spacing distribution in the set $\{\lambda_k\}$. To avoid having to perform spectral unfolding, we

chose to evaluate the distribution of ratios of adjacent level spacings [62]: $r_k = (\lambda_{k+1} - \lambda_k)/(\lambda_k - \lambda_{k-1})$. Accurate surmises exist for the distribution of these ratios in the case of Gaussian ensembles [80]. They are given by

$$P_{\rm WD}(r) = \frac{1}{Z}\frac{(r+r^2)^\beta}{(1+r+r^2)^{1+3\beta/2}}, \tag{16}$$

where $Z = \frac{8}{27}$ for the Gaussian Orthogonal Ensemble (GOE) with $\beta = 1$, and $Z = \frac{4}{81}\frac{\pi}{\sqrt{3}}$ for the Gaussian Unitary Ensemble (GUE) with $\beta = 2$. The corresponding distribution for the Poisson distributed spectrum is given by the exact form

$$P_{\rm Poisson} = \frac{1}{(1+r)^2}. \tag{17}$$

Notice that for the Gaussian ensembles, level repulsion manifests itself in the asymptotic behavior $P(r \to 0) \sim r^\beta$, which is absent in the case of Poisson statistics.

Results are shown in Fig. ·5 for disordered Heisenberg chains with $L = 16$ and 100 disorder realizations. A completely random real state follows a GOE statistics.

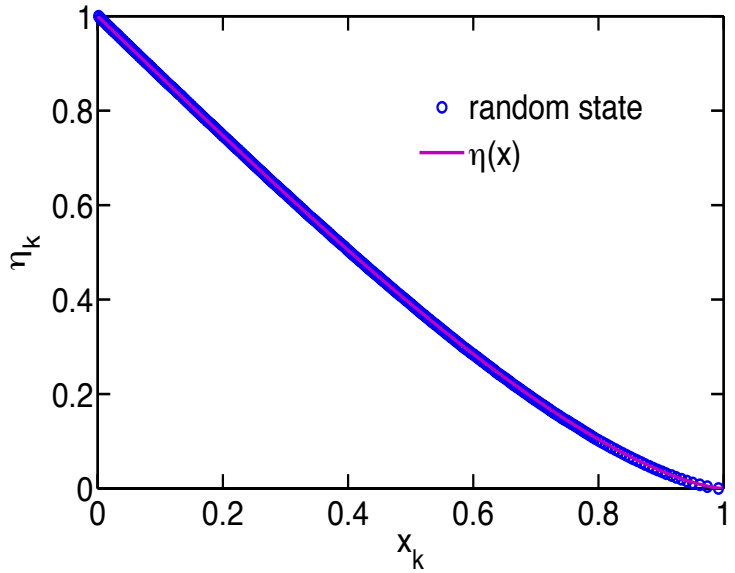

Figure ·4: Average entanglement pectrum of completely random wavefunction ($L = 16$, 100 realizations used).

The universal part of the spectrum at $h = 0.5$ also follows a GOE distribution.

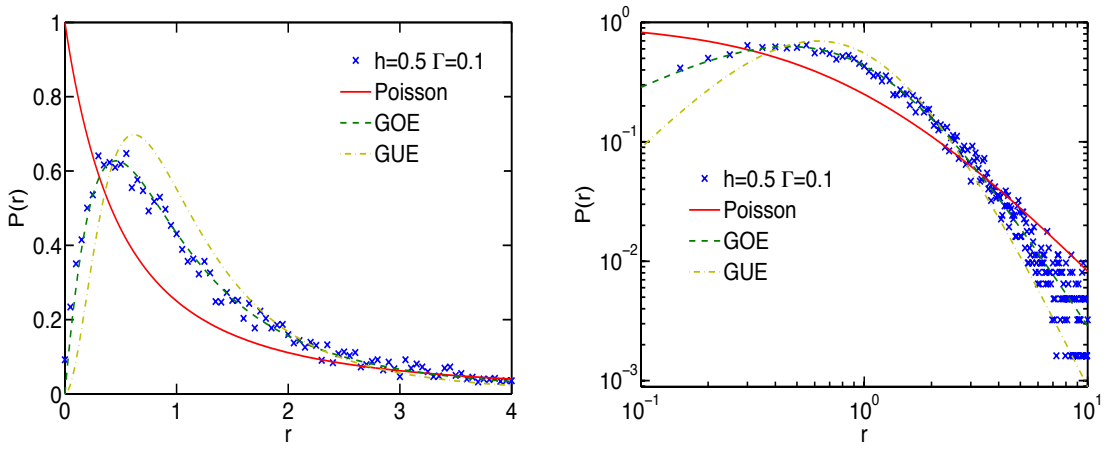

Figure ·5: Left panel: Distribution of the ratios of consecutive spacings for the entanglement spectrum of Heisenberg spin chains with disorder parameter $h = 0.5$ and transverse field $\Gamma = 0.1$ (crosses). Right panel: the same data in a logarithmic scale. $L = 16$ and 500 realizations used.

C Protocol for determining k_h

The definition of the order parameter in this Letter required a protocol for determining the point k_h which separates the non-universal part ($k \leq k_h$) from the universal ($k > k_h$) part of the rank-ordered entanglement levels. We use the following protocol: we took the spectrum obtained from each random state considered and multiply it by a factor s such that the rescaled smallest singular value coincided in value with that obtained from a completely random state. Then we swept through the spectrum, starting from the tail, and computed the relative deviation from the completely random state prediction, until it exceeded a certain amount. That is, until

$$\frac{(\lambda_k)^2 - s(\lambda_k^{MP})^2}{s(\lambda_k^{MP})^2} > \epsilon, \tag{18}$$

where ϵ is a number of order 1. In our case, we set $\epsilon = 1$.

However, we would like to point out one subtlety of this methodology. In cases where the universal component of the spectrum almost vanishes near the transition, it is hard to accurately locate the critical point. That is because the last few points at the tail of the spectrum show large sample-to-sample fluctuations, and our protocol requires strictly matching a single point close to the tail. Therefore, k_h can be very sensitive to our choice of the matching point and can even yield incorrect predictions under finite-size scaling. On the other hand, we find that in cases such as the QREM, where there is still a large fraction of the universal component at the transition, this methodology is not very sensitive to the choice of matching point. For the Heisenberg model, we locate the critical point k_h by choosing the matching point away from the tail end, thus effectively discarding the smallest eigenvalues. For example, for $L = 16$ we discarded the last 16 eigenvalues. In order to demonstrate that this does not lead to a sizable errors in determining the MBL critical point, we also computed the the order parameter directly from the *averaged* entanglement spectrum, where the fluctuations are smoothened out (Fig. ·6). The critical point found this way is very close to the one we show in the main text. We believe that the result can be further improved if more realizations are include in the averaring, which we hope to attempt in the future.

D Entanglement spectra for QREM and RK-type toy models

In this section, we present in Fig. ·7 through Fig. ·9 the entanglement spectra for the QREM and two RK-type toy models that were discussed in the main text.

We clearly see the following: (1) the two-component structure shows up in all three cases; (2) the same evolution behavior as explained in the main text happens here as well. Namely, the universal fraction shrinks as one increases the strength of disorder, thereby pushing the states further away from completely random states.

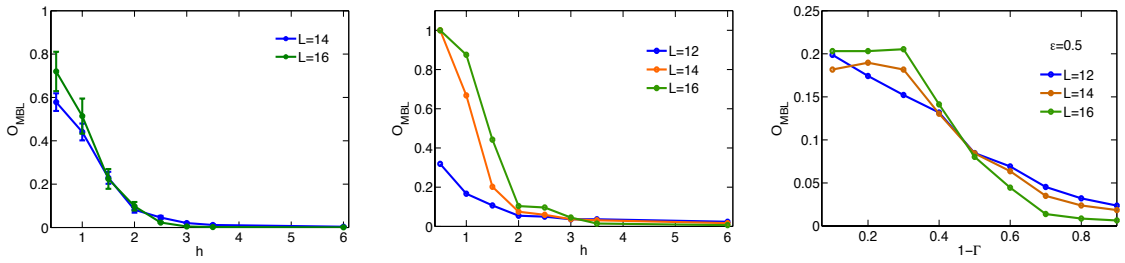

Figure ·6: Left: Results obtained when the matching point is chosen too close to the last eigenvalue for each entanglement spectrum, yielding a wrong transition point under finite-size scaling. Middle: the order parameter computed from the *averaged* entanglement spectrum of the random-field Heisenberg model, where fluctuations are smoothened out and not many small eigenvalues need to be eliminated. Right: the order parameter computed from the average entanglement spectrum of the QREM. One can see that in this case our approach is robust and the result is very close to that shown in the main text.

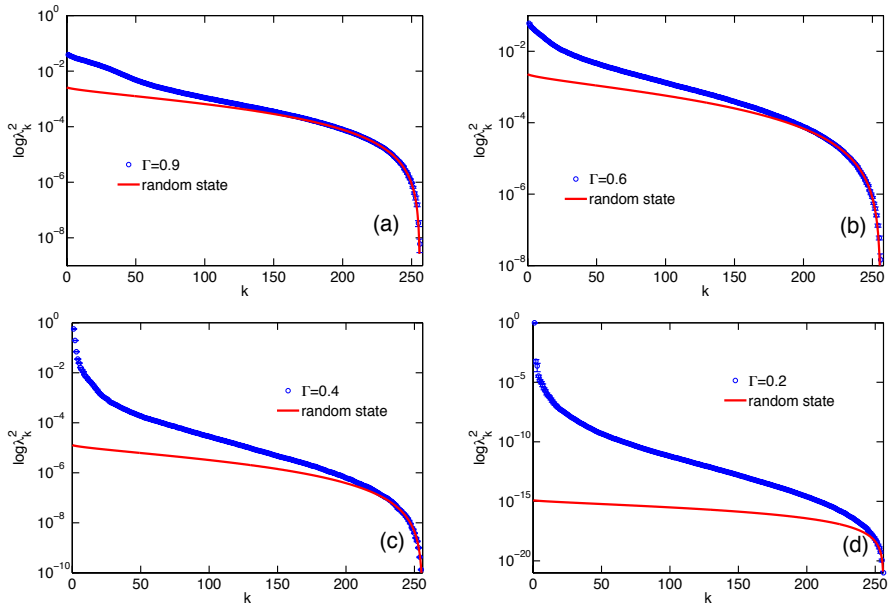

Figure ·7: Averaged entanglement spectrum of eigenstates with energy density $\epsilon = 0.5$, for the QREM. The system size $L = 16$, and $\Gamma = 0.9,\ 0.6,\ 0.4$, and 0.2, averaging over 10 realizations of disorder.

We also show the order parameter for the QREM at energy density $\epsilon = 0.3$, which is different from the one shown in the main text. We clearly see from Fig. ·10 that the

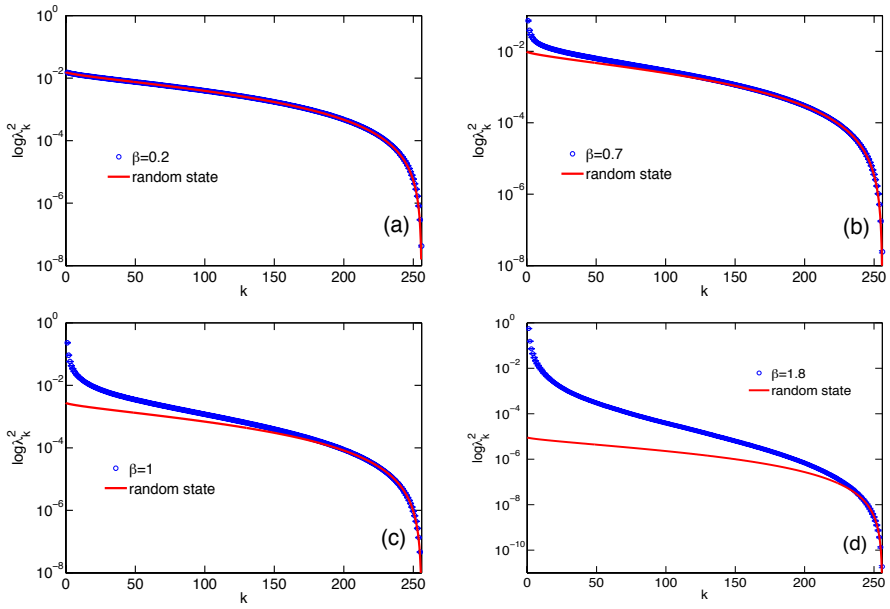

Figure ·8: Averaged entanglement spectrum of the RK-type wavefunction, with $E(\boldsymbol{\sigma}) = E_{\rm REM}(\boldsymbol{\sigma})$. The system size $L = 16$, and $\beta = 0.2,\ 0.7,\ 1$, and 1.8, averaging over 100 realizations of disorder.

curves for different system sizes cross at around $\Gamma_c \approx 0.25$, which is again in excellent agreement with previous known results.

E Randomness versus non-randomness: another toy model

In this section, we view the emergence of the non-universal component in the entanglement spectrum from a different perspective: the degree of randomness in the wavefunctions. The physical intuition can be understood as follows. A completely random state is supposed to yield a Marchenko-Pastur distribution in its entanglement spectrum, i.e. only the universal component exits. This implies that for states whose entanglement spectra deviate from Marchenko-Pastur distribution, they cannot be completely random. Therefore we construct another toy model which captures this feature, by borrowing ideas from spin glasses.

First let us start with a truly random (real) wavefunction that we denote by

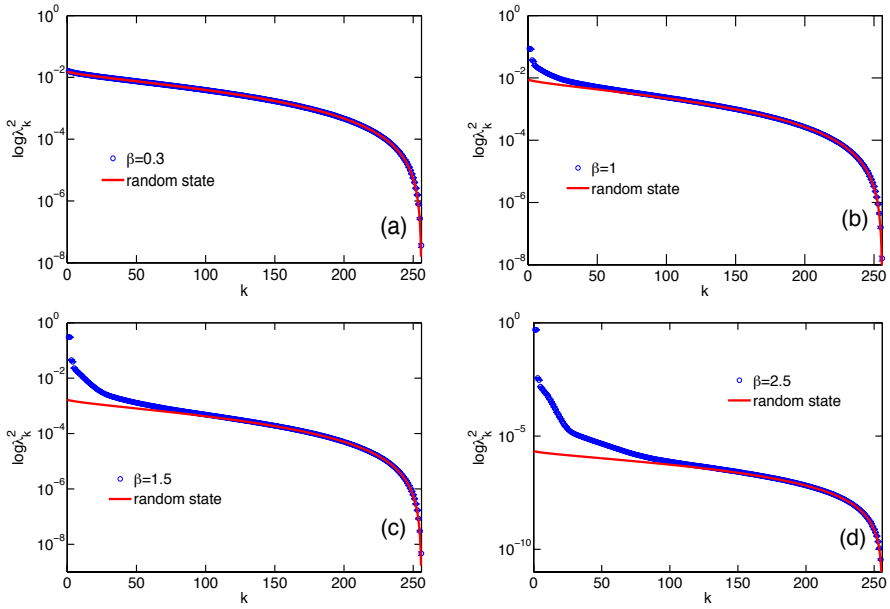

Figure ·9: Averaged entanglement spectrum of the RK-type wavefunction, with $E(\boldsymbol{\sigma}) = -\frac{J}{L}\sum_{i<j}\sigma_i^z\sigma_j^z$. The system size $L = 16$, and $\beta = 0.3,\ 1,\ 1.5$, and 2.5, averaging over 100 realizations of random sign.

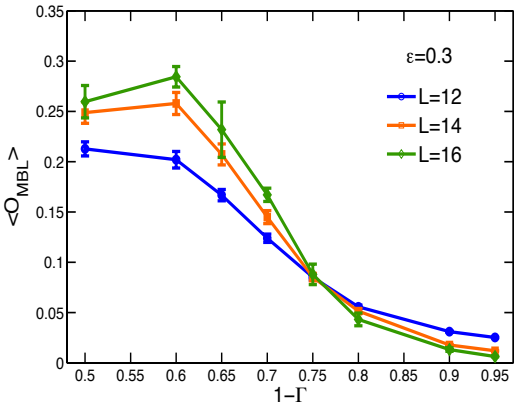

Figure ·10: The order parameter for QREM with target energy density $\epsilon = 0.3$.

$\Psi_{\rm REM}(\boldsymbol{\sigma}) = {\rm sgn}(E_{\rm REM})$, where ${\rm sgn}(x)$ is the sign function and $E_{\rm REM}$ are identically independently distributed with probability $P(E_{\rm REM}) = \frac{1}{\sqrt{\pi L}}{\rm e}^{-E_{\rm REM}^2/L}$, with L being the number of spins. The wavefunction $\Psi_{\rm REM}$ is, by construction, random. The

subscript REM is used to draw an analogy to the Random Energy Model (REM) in spin glass systems.

Next, we note that the REM is a limiting case of a spin glass with p-spin interactions as $p \to \infty$, which eliminates correlations between configurations. So we can take a step back and consider the following "less random" Sherrington-Kirkpatrick (SK) spin glass model with infinite-range two-spin interactions [53], and construct the following wavefunction:

$$\Psi_{\rm SK}(\boldsymbol{\sigma}) = \mathrm{sgn}\left(E_{\rm SK}(\boldsymbol{\sigma})\right) = \mathrm{sgn}\left(\sum_{i<j} J_{ij}\ \sigma_i\,\sigma_j\right), \tag{19}$$

where the J_{ij} are drawn from uniform distribution in the interval $[-1, 1]$. The amplitudes computed from the SK-like model are obviously not as random as in the REM-like one; there are only $L(L-1)/2$ independent random J_{ij}'s in the former as opposed to 2^L independent random amplitudes in the latter. Nevertheless, the amplitudes of $\Psi_{\rm SK}$ do inherit some randomness from the J_{ij}, and the energy distribution of the SK-like model also follows accurately a Gaussian distribution for any *one* given $\boldsymbol{\sigma}$, similarly to those in the REM-like model. But the correlations between the amplitudes for *different* $\boldsymbol{\sigma}$ exist in the case of the SK-like model, and these correlations are manifest in the entanglement spectrum computed from $\Psi_{\rm SK}$, as shown in the left panel of Fig. ·11.

The entanglement entropy follows a volume-law scaling (see inset of Fig. ·11) and, again, we see the emergence of a two-component structure in the spectrum. The universal part agrees with RMT. The non-universal part is different from that found for the high energy eigenstates of a disordered Heisenberg spin chain, reflecting its non-universal, model dependent nature. Yet, this component is still characterized by its fast decay rate. The toy model shows that non randomness can be present in a generic quantum state when there are correlations between components of the

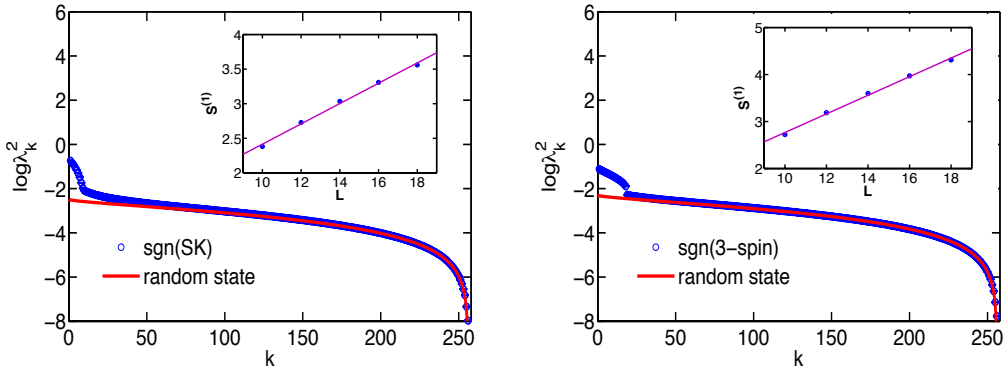

Figure ·11: (Color online) Entanglement spectrum of: $\Psi_{\rm SK}$ (left) and $\Psi_{3-{\rm spin}}(\boldsymbol{\sigma})$ (right), for a system of size $L = 16$, averaged over 500 realizations of disorder. The order parameter as defined in Eq. (3) is: $\langle \mathcal{O} \rangle = 0.3888 \pm 0.0067$, with a threshold $k \approx 30$ for $\Psi_{\rm SK}$; and $\langle \mathcal{O} \rangle = 0.4279 \pm 0.0060$, with a threshold $k \approx 24$ for $\Psi_{3-{\rm spin}}(\boldsymbol{\sigma})$. The insets show the volume-law scaling of the von Neumann entanglement entropy.

wavefunction. The entanglement spectrum captures the non randomness and its structure can be well described by a two-component picture.

Another interesting manifestation of the mixing between universal and non-universal components in the SK wavefunction is revealed by employing a color map. In Fig. ·12 we show the amplitude of the wavefunction $\Psi_{\rm SK}(\boldsymbol{\sigma}_A, \boldsymbol{\sigma}_B)$ plotted in a $\boldsymbol{\sigma}_A \times \boldsymbol{\sigma}_B$ grid, and compared it to the amplitude of a REM wavefunction. The existence of a structure, similar to wefts in a tapestry, is clearly visible for the $\Psi_{\rm SK}$ wavefunction, but completely absent for the REM wavefunction.

One can further consider wavefunctions built with three-spin interactions,

$$\Psi_{3-{\rm spin}}(\boldsymbol{\sigma}) = {\rm sgn}\left(\sum_{i<j<k} J_{ijk}\, \sigma_i\, \sigma_j\, \sigma_k \right), \tag{20}$$

where the J_{ijk} are drawn from a uniform distribution in the interval $[-1, 1]$. As shown in the right panel of Fig. ·11, the spectrum again shows a two-component structure, very similar to the cases discussed in the main text.

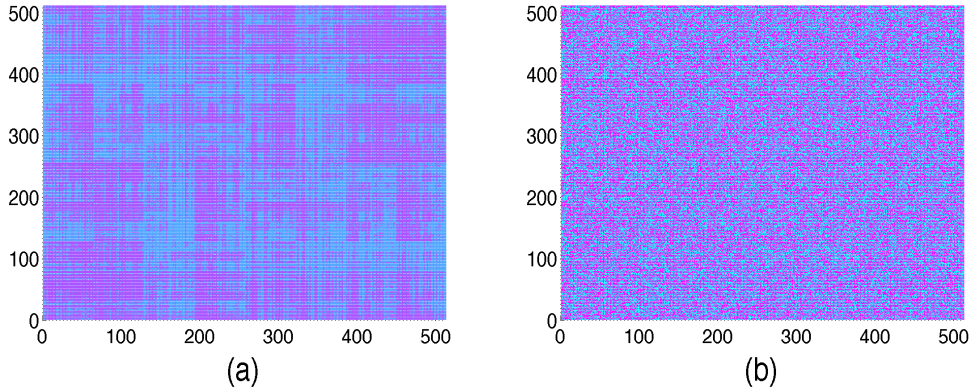

Figure ·12: (Color online) Color map of the matrix $\Psi(\boldsymbol{\sigma}_A, \boldsymbol{\sigma}_B)$ for typical realizations of the (a) SK and (b) REM wavefunctions ($L = 18$).

Chapter 3

Entanglement complexity in quantum many-body dynamics, thermalization and localization

Abstract

Entanglement is usually quantified by von Neumann entropy, but its properties are much more complex than what can be expressed with a single number. We show that the three distinct dynamical phases known as thermalization, Anderson localization, and many-body localization are marked by different patterns of the spectrum of the reduced density matrix for a state evolved after a quantum quench. While the entanglement spectrum displays Poisson statistics for the case of Anderson localization, it displays universal Wigner-Dyson statistics for both the cases of many-body localization and thermalization, albeit the universal distribution is asymptotically reached within very different time scales in these two cases. We further show that the complexity of entanglement, revealed by the possibility of disentangling the state through a Metropolis-like algorithm, is signaled by whether the entanglement spectrum level spacing is Poisson or Wigner-Dyson distributed.[1]

[1]The contents of this chapter were published in Physical Review B, **96**, 020408 (2017).

3.1 Introduction

Entanglement is usually quantified by a number, the entanglement entropy, defined as the von Neumann entropy of the reduced density matrix ρ_A of a subsystem, and it is a key concept in many different physical settings, from novel phases of quantum matter [6, 7, 81, 82] to cosmology [60, 83]. However, there is a lot more information in the entanglement spectrum of ρ_A, namely the full set of its eigenvalues (or its logarithms) [22]. Recently, a measurement protocol to access the entanglement spectrum of many-body states using cold atoms has been proposed [84]. The main goal of this letter is to explore the relationship between entanglement spectrum and dynamical behavior of a quantum many-body system.

In Refs. [28, 33] it was shown that the entanglement of a state generated by a quantum circuit can be simple or complex, in the sense that the state either can or cannot be disentangled by an *entanglement cooling* algorithm that resembles the Metropolis algorithm for finding the ground state of a Hamiltonian. The success or failure of the disentangling procedure is signaled by the so called entanglement spectrum statistics (ESS) [28, 33], namely the distribution of the spacings between consecutive eigenvalues of ρ_A. When such a distribution is Wigner-Dyson (WD), the cooling algorithm fails. This situation occurs when the gates in the circuit are sufficient for universal computing, either classical or quantum. On the other hand, for circuits that are not capable of universal computing, the states can be disentangled and they feature a (semi-)Poisson ESS.

In this chapter, we focus on systems whose dynamics is controlled by a time-independent quantum many-body Hamiltonian, as opposed to a random circuit. We study the entanglement complexity revealed by the ESS of the time-evolved state for Hamiltonians whose eigenstates yield one of three behaviors: 1) eigenstate thermalization (ETH) [18, 85–88], 2) Anderson localization (AL), or 3) many-body localization

(MBL) [19, 20, 62]. We find that the time-evolved states under Hamiltonians that feature AL follow a Poisson ESS, and that they can be disentangled by applying the entanglement cooling algorithm which uses only the unitaries generated from one-and two-body terms in the Hamiltonian. On the other hand, the time-evolved states under Hamiltonians that satisfy ETH follow a WD distribution, and the entanglement cooling algorithm fails. Remarkably, the dynamics generated by MBL Hamiltonians results in ESS approaching asymptotically in time a WD distribution, the same distribution that time-evolved states with ETH Hamiltonians reach in shorter times. We find that the rate of such approach to WD scales with the inverse of the logarithm of time. We further find that the state generated by MBL Hamiltonians cannot be disentangled using a cooling algorithm.

3.2 Quantum Quench of the Heisenberg spin chain

We shall focus on a quantum state that is time-evolved after a *quantum quench*, namely, a sudden switch of the Hamiltonian so as to throw the initial state away from equilibrium. We consider the XXZ spin-1/2 chain of L sites with open boundary conditions,

$$H = J\sum_{i=1}^{L-1}(\sigma_i^x\sigma_{i+1}^x + \sigma_i^y\sigma_{i+1}^y + \Delta\sigma_i^z\sigma_{i+1}^z + z_i\sigma_i^z + x_i\sigma_i^x)\ . \tag{3.1}$$

We consider three distinct regimes of parameters: (i) In the absence of a transverse field and interaction ($\Delta = x_i = 0, z_i \neq 0$), the Hamiltonian in Eq. (3.1) maps onto free fermions via a Jordan-Wigner transformation [89, 90]. The complexity of the problem is reduced from that of diagonalizing a $2^L \times 2^L$ matrix to that of diagonalizing a $L \times L$ matrix. In the limit case of no disorder, $z_i = \text{const}$, the system is completely integrable while in the presence of disorder it shows AL [91]. In the case of AL, the Hamiltonian is noninteracting in the basis of local conserved quantities. The presence of constants

of motion prevents the system from thermalizing. (ii) In the presence of interactions and weakly disordered external fields ($z_i \in [-1, 1]$ and $\Delta = 0.5$), the Hamiltonian in Eq. (3.1) is nonintegrable and thermalizes. Its eigenstates obey ETH. (iii) Finally, in the presence of interactions and strong disorder ($z_i \in [-10, 10]$ and $\Delta = 0.5$), the system features MBL: Even the high-energy eigenstates of such a system are weakly entangled, obey an area law and thus do not follow ETH [17, 18, 61]. The dynamical behavior of the MBL phase is also apparent in the fact that during the evolution, the entanglement grows only logarithmically in time [21, 63, 92].

The quantum evolution is studied as follows. We consider the state $|\Psi(t)\rangle = \exp(-iHt)|\Psi_0\rangle$, where $|\Psi_0\rangle = \otimes_j |\psi\rangle_j$ is a random factorized state. By quenching to different values of $\{x_i, z_i, \Delta\}$, we can obtain all possible dynamics we want to study. The marginal state $\rho_A(t)$ corresponds to the reduced density matrix of one half of the total chain. The set of eigenvalues of ρ_A are then denoted by $\{p_i\}_{i=1}^{2^{L/2}}$ and ordered in decreasing order. At the same time, we also consider the eigenenergies $\{E_j\}_{j=1}^{2^L}$ of the full Hamiltonian.

3.3 Entanglement spectrum statistics

At $t = 0$, the state contains initially no entanglement and gets entangled only through the dynamics. After a time $t_0 = 1000$ in units of $1/J$, we study the ESS of the spectrum $\{p_i\}_{i=1}^{2^{L/2}}$ [28, 33], here obtained from the distribution $P(r) = R^{-1} \sum_{i=1}^{R} \langle \delta(r - r_i) \rangle$ of the ratios of consecutive spacings, $r_i = (p_{i-1} - p_i)/(p_i - p_{i+1})$. In an analogous fashion, we obtain the statistics of ratios of the energy spectrum $\{E_j\}_{j=1}^{2^L}$ and compare it to the ESS. Our results are summarized in Table 3.1.

We first consider case (i), the XX spin chain ($\Delta = x_i = 0$) in the presence of a random field $z_i \in [-h, h]$. This model can be brought into the form of free fermions in one dimension and features AL for every value of h. Here, we choose $h = 1$. In Fig. 3·1a,

	Dynamical phases		
Features	AL	ETH	MBL
Entanglement spectrum	Poisson	WD	WD
Energy spectrum	Poisson	Poisson *or* WD	Poisson
Entanglement cooling	✓	✗	✗

Table 3.1: Summary of the main results presented in this chapter. The ESS of Hamiltonians featuring AL shows a Poisson distribution, while for both ETH and MBL Hamiltonians it displays a WD distribution. In particular, the deviation from the WD distribution in the MBL case decays as $1/\log(t)$. The energy level spacing statistics yields a Poisson distribution for both AL and MBL, while for ETH case it can be either Poisson (in the presence of additional conserved quantities) or WD (with no conserved quantities). Finally, the states generated by AL Hamiltonians can be disentangled using an entanglement cooling algorithm, while the states generated by ETH and MBL Hamiltonians cannot.

we show $P(r)$ of the final states after a long time evolution ($t_0 J = 1000$). The ESS fits the distribution expected for uncorrelated eigenvalues, $P_{\text{Poisson}}(r) = (1+r)^{-2}$, which can be straightforwardly derived assuming a Poisson distribution of spacings. In Refs. [28, 33] such statistics corresponds to simple patterns of entanglement that are easily reversible under the entanglement cooling algorithm. In the quantum quench scenario, such pattern results in the failure to reach thermalization. Indeed, the distribution of the spacings in the energy spectrum is also Poisson (see Fig. 3·1b), which is a typical feature of integrable systems [93, 94]. As we can see, in the integrable case, the ESS and the energy level spacings convey the same information. Similarly, we find that in the completely integrable case ($z_i = 0$) both ESS and energy spectrum are still Poisson. However, because of the absence of localization, entanglement propagates and fulfills volume law like in a thermal system [95], though no thermalization can happen. This shows that it is the finer structure of entanglement in the ESS that is able to diagnose dynamical phases, instead of just the amount of entanglement.

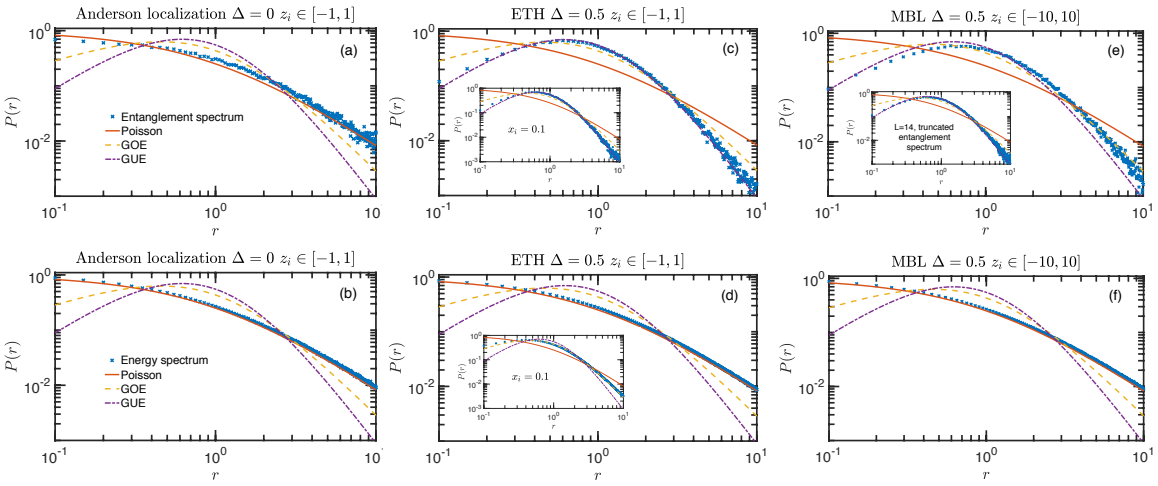

Figure 3·1: (Color online) Comparison between ESS and energy level spacing statistics after a quantum quench at $t_0 = 1000$ starting from a random product state in systems that are Anderson localized (a-b), nonintegrable and featuring ETH (c-d), featuring MBL (e-f). ESS follows three different distributions, namely Poisson (a), WD (c), and a non-universal one (e), thus perfectly classifying the three different dynamical phases. On the other hand, the distribution of the energy level spacings is always Poisson in all three cases. It becomes WD in the nonintegrable, ETH case shown in inset of panel (d) only if total magnetization S_z conservation is broken by a field in the x direction. In the MBL case, the ESS approaches WD upon discarding the largest eigenvalues values of the spectrum (inset of (e)). All simulations are done with 2000 realizations of disorder and $L = 12$ unless otherwise specified.

When the interaction Δ is switched on, the system can be made nonintegrable by introducing a random field z_i [96, 97]. Although nonintegrable, there is still a simple conserved quantity in the model, namely, the total magnetization S_z in the z direction. If the disorder is weak (we choose $h = 1$) we are in case (ii): The model obeys ETH and thermalizes. At this point we are confronted with a shortcoming of the energy level statistics. For a nonintegrable system, the distribution of energy level spacings is expected to follow a WD distribution and very accurate surmises exist in this case [80]: $P_{\mathrm{WD}}(r) = Z^{-1}(r + r^2)^{\beta}(1 + r + r^2)^{-1-3\beta/2}$, where $Z = 8/27$

for the Gaussian Orthogonal Ensemble (GOE) with $\beta = 1$, and $Z = 4\pi/81\sqrt{3}$ for the GUE with $\beta = 2$. However, to find such a result one needs to diagonalize the Hamiltonian only in the subspace of fixed total magnetization [98]. If one does not know what the conserved quantities are – and this is a generic case – and diagonalizes the Hamiltonian in the full Hilbert space, one would find again Poisson statistics, see Fig. 3·1d. However, if one breaks the S_z conservation by a small uniform field in the x direction, one does find the WD distribution, see inset of Fig. 3·1d. Thus, for nonintegrable systems, one is required to know all conserved quantities in order to check the ETH through the energy level statistics. The presence of just one (local) constant of motion makes the system behave as integrable (Poisson statistics) from the viewpoint of the energy gaps if we consider the full spectrum, even though the system indeed thermalizes, while breaking all conservation laws results in WD, see Table 3.1.

In contrast, we find that the ESS is more robust and captures that thermalization should not be impaired by the fact that there is one conserved quantity. We find that the ESS data agrees well with a WD distribution with $\beta = 2$, see Fig. 3·1c. Breaking the last constant of motion by introducing a small constant field $x_i = 0.1$ in the x direction results in the same distribution (see inset). Therefore, it is clear that ESS already gives us an advantage in comparison to the energy level statistics, as it can discriminate between integrable and nonintegrable models without requiring the knowledge of the local conserved quantities.

Finally, keeping fixed $\Delta = 0.5$ and increasing the range of z_i we enter in the MBL case (iii). In spite of the system being still nonintegrable, the energy eigenstates stay very localized breaking ergodicity and hence thermalization. Moreover, the eigenstates are weakly entangled (they obey an area law [57, 99], which for a one-dimensional chain implies an entanglement entropy nearly independent of the system

size). Thus the mechanism behind ETH breaks down and the system does not thermalize, at least within reasonable time scales, that is, nonexponential in system size. At such time scales, the system shows some features of the integrable systems, as there is an extensive number of quasilocal conserved quantities [99–103]. This is also reflected in the distribution of the energy level spacings. We computed that distribution and show it in Fig. 3·1f, which reveals a Poisson statistics, just like for an integrable system (or AL, that is, integrable).

Let us now analyze the ESS for MBL. We shall find that MBL can be distinguished from both AL/integrable systems and ETH. The analysis that we present below shows that the ESS for MBL approaches asymptotically a WD distribution at rather long time scales, which we quantify below. The ESS is shown in Fig. 3·1e, and show the following features. At the given time scale ($t_0 J = 1000$), the ESS appears to deviate from WD statistics (as well as from Poisson statistics); the deviation is reduced if one considers a fraction of the full spectrum, retaining lowest eigenvalues values of the spectrum and discarding the largest ones (see inset). In order to quantify the approaching of the entanglement spectrum to WD (GUE) distribution upon truncation, we consider the statistical distance between two probability distributions given by the Kullback-Leibler (KL) divergence: $D_{\mathrm{KL}}(p\|q) = \sum_i p_i \log(p_i/q_i)$. In Fig. 3·2a, we show the KL divergence between $P(r)$ of MBL and the WD distribution as function of the fraction of the cutoff. As more of the largest eigenvalues values are discarded, we get closer to universal statistics. Moreover, we find that, as function of evolution time, all the D_{KL} decreases as $1/\log(t)$ (see Fig. 3·2b), and thus the ESS of MBL asymptotically approaches a WD (GUE) distribution. (We remark that the D_{KL} divergence between $P(r)$ and the WD distribution in the ETH regime goes to zero at a time scale of order $1/J$.) Indeed, in the infinite time limit, time-evolved states in the MBL regime also have to equilibrate, as the time fluctuations of typical observables

go to zero, though the scaling with both time and system size are different in MBL from ETH [104].

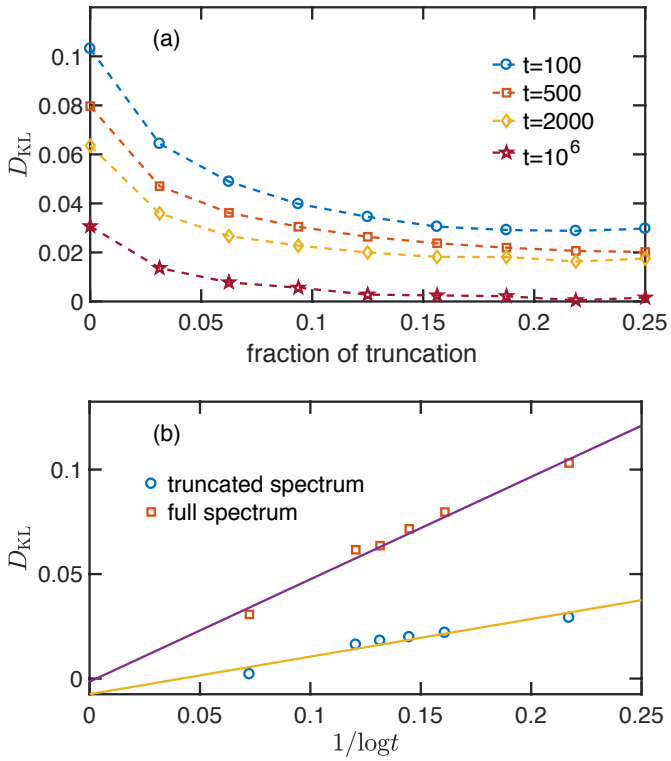

Figure 3·2: (Color online) (a) The KL divergence D_{KL} as function of the fraction of truncation of the full spectrum for different total evolution times ($L = 14$ and $z_i \in [-8, 8]$). The data are averaged over 100 realizations of disorder and 2000 realizations of the initial product state, evolved for times $t = 100, 500, 1000$, and 10^6. (b) scaling of D_{KL} with $1/\log(t)$ for the full spectrum and for the truncated spectrum at fraction 0.1875, consistent with the KL divergence vanishing at long times and the ESS asymtoptically reaching the WD distribution.

We interpret the slow approach to universal WD (GUE) statistics of the ESS of a state following unitary evolution with a Hamiltonian in the MBL regime as follows. At reasonable time scales, the system has approximately local conserved integrals of motion, and may look like an integrable one. However, unlike AL, the MBL Hamiltonian remains interacting even in the basis of conserved quantities. Eventually, for

long time scales, information propagates along the full chain [105], and the interaction between far away quasilocal conserved quantities is revealed by the slow $1/\log(t)$ approach to the universal WD distribution. The ESS detects the presence of interaction *already* at short time scales, because the deviations from the universal distribution are small and decreasing in time. None of these aspects can be captured by the study of the energy level spacings. We remark that this feature of the ESS is a truly dynamical one, and depends on the fact that the system is away from equilibrium. If one truncates the entanglement spectrum of a high energy *eigenstate* of MBL, the spectrum stays nonuniversal [31, 106, 107].

3.4 Complexity of Entanglement

The different statistics in the ESS correspond to different complexity of the entanglement generated by the time evolution. In Refs. [28, 33], it was shown that the entanglement generated by a quantum circuit can be undone by an entanglement cooling algorithm when the ESS shows (semi-)Poisson statistics. On the other hand, if one uses a quantum circuit obtained by a universal set of gates, the ESS displays WD statistics and the simple algorithm for disentangling fails, so the ESS is complex.

How does the disentangling algorithm perform in the case of Hamiltonian evolution? We start from the final state obtained after a quantum quench for running time $t_0 = 1000$, like in the previous analysis for ESS. Notice that a similar amount of entanglement (averaged over all possible contiguous bipartitions of the system) is reached in both the MBL and the AL case (see Fig. 3·3), while the average entanglement is much higher for the ETH case. The disentangling (cooling) algorithm works as follows. We pick randomly a one-or two-body term from the model Eq. (3.1), and evolve the state for a time $\delta t = \pi/10$. Then we accept such an attempt with probability $\min\{1, \exp(-\beta\Delta\bar{S})\}$, where $\Delta\bar{S}$ is the change of the amount of von Neumann

entropy averaged over all possible bipartitions of the system, and β^{-1} is a fictitious temperature that is gradually reduced to zero.

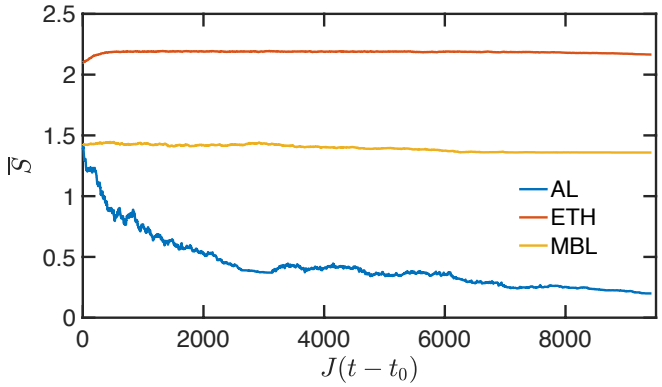

Figure 3·3: (Color online) Attempt of disentangling using the entanglement cooling algorithm starting from the states at $t_0 = 1000$. $\bar{S}$ is the von Neumann entropy averaged over all possible bipartitions of the system with $L = 12$.

Let us look first at the cooling in the disordered XX model, which at time $t_0 = 1000$ after the quench features Poisson statistics for the ESS – what we would call a non-complex entanglement pattern. The performance of the cooling algorithm is shown in the blue curve in Fig. 3·3. As the data show, the state can be disentangled almost completely by this kind of entanglement cooling algorithm. It is a remarkable fact that entanglement can be undone after Hamiltonian evolution even without knowledge of the precise Hamiltonian.

What happens for ETH and MBL? Figure 3·3 shows that the entanglement entropy reached at $t_0 = 1000$ using both the MBL and ETH Hamiltonians cannot be undone by the cooling algorithm, even though the value of the entanglement entropy is smaller in the case of MBL. States generated from evolutions using MBL or ETH Hamiltonians cannot be disentangled, and in both cases, the ESS shows some degree of universality (both reach a WD distribution, albeit at rather different time scales). We conclude that what determines how easy or hard it is to disentangle a state is not

the level of entanglement, as measured by the entanglement entropy, but instead that information is contained in the ESS, like in the case for states generated by quantum circuits.

Chapter 4

Scrambling via braiding of nonabelions

Abstract

We study how quantum states are scrambled via braiding in systems of non-Abelian anyons through the lens of entanglement spectrum statistics. In particular, we focus on the degree of scrambling, defined as the randomness produced by braiding, at the same amount of entanglement entropy. To quantify the degree of randomness, we define a distance between the entanglement spectrum level spacing distribution of a state evolved under random braids and that of a Haar-random state, using the Kullback-Leibler divergence D_{KL}. We study D_{KL} numerically for random braids of Majorana fermions (supplemented with random local four-body interactions) and Fibonacci anyons. For comparison, we also obtain D_{KL} for the Sachdev-Ye-Kitaev model of Majorana fermions with all-to-all interactions, random unitary circuits built out of (a) Hadamard (H), $\pi/8$ (T), and CNOT gates, and (b) random unitary circuits built out of two-qubit Haar-random unitaries. To compare the degree of randomness that different systems produce beyond entanglement entropy, we look at D_{KL} as a function of the Page limit-normalized entanglement entropy S/S_{max}. Our results reveal a hierarchy of scrambling among various models — even for the same amount of entanglement entropy — at intermediate times, whereas all models exhibit the same late-time behavior. In particular, we find that braiding of Fibonacci anyons randomizes initial product states more efficiently than the universal H+T+CNOT

set. [1]

4.1 Introduction

The notion of many-body quantum chaos plays a central role in understanding the emergence of statistical mechanical descriptions and thermodynamics of quantum systems under unitary time evolution (see for example [108–111]). A precise quantitative formulation of quantum many-body chaos, in particular, remains an important problem. One possible diagnostic of chaos that has attracted recent interest is the "out-of-time-ordered" correlator (OTOC) [112, 113], which generalizes the classical butterfly effect and Lyapunov exponent to quantum systems [114–117]. Indeed, the exponential growth behavior of the OTOC with a corresponding quantum Lyapunov exponent λ_L has been confirmed in several large-N theories (including large-N gauge theories, as well as theories holographically dual to black holes [114–121]), and weakly interacting disordered systems [122].

A notion intimately related to chaos is *scrambling*, which refers to the phenomenon that initially localized information of a system becomes undetectable under its own dynamics without measuring a significant fraction of all degrees of freedom [123]. It was shown that the butterfly effect necessarily implies scrambling in quantum systems [124]. Scrambling can be captured by local entropy production under time evolution in chaotic systems [125]. Remarkably, the entanglement growth under random unitary dynamics belongs to the same universality class of Kardar-Parisi-Zhang equation for classical surface growth [15, 126]. One may be tempted then to characterize the degree of scrambling for different systems in terms of the growth rates of entanglement. However, the entanglement growth can behave in the same fashion in systems that are not truly chaotic, for example, under random Clifford dynam-

[1] The contents of this chapter were published in Physical Review B, **99**, 045132 (2019).

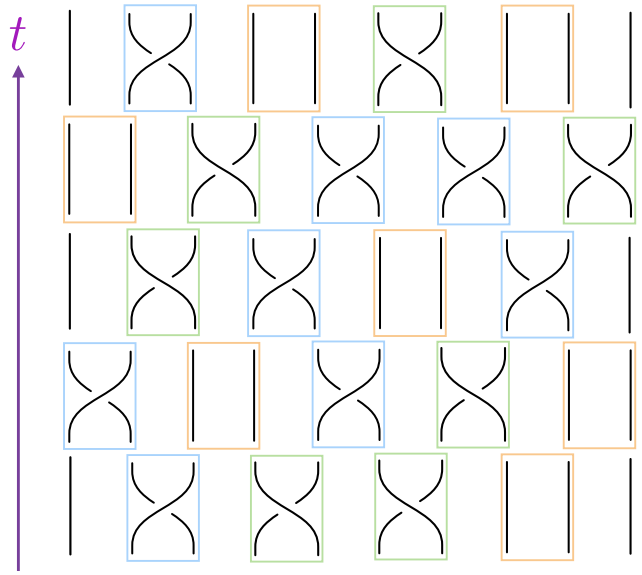

Figure 4·1: (Color online) Depiction of braidings as a brick wall lattice of tiles representing elementary strand exchanges: 1 (no exchange), T (overpass), and T^{-1} (underpass) respectively. A random braid corresponds to a random choice of these tilings.

ics [15, 28].

Indeed, scrambling can exhibit different complexities depending on the randomness it produces, and there is a gap between maximal entanglement entropy and complete randomization [29, 30]. In this chapter, we propose a measure of the degree of scrambling that employs the entanglement spectrum (ES) statistics. We shall mainly focus on dynamics generated by random unitary circuits without additional conserved quantities, although we do present an example of Hamiltonian dynamics as well. Random unitary circuits serve as an excellent theoretical playground in recent studies of quantum chaos, from which lots of insights on deterministic dynamics can be obtained [15, 34, 35, 127]. For chaotic random circuits, one expects that the long time evolution *samples uniformly* from the ensemble of Haar-random states [128, 129]. Therefore, the entanglement level spacing distribution of the final states of a sufficiently long evolution should be that of Haar-random states, which are described

by random matrix theory, in particular, the Gaussian unitary ensemble (GUE) in the present case [31, 130, 131]. Crucially, this observation will allow us to define a *distance* between the entanglement level spacing distribution of unitarily evolved states at *intermediate* times — when the entanglement entropy is far from reaching its maximum — and the GUE distribution. In this work, we choose as the measure of distance the Kullback-Leibler (KL) divergence, or relative entropy, defined as

$$D_{\mathrm{KL}}(p||q) = \sum_i p_i \ln \frac{p_i}{q_i}, \tag{4.1}$$

and satisfying $D_{\mathrm{KL}} \geq 0$, where $\{p_i\}$ and $\{q_i\}$ are two sets of discrete probability distributions p, q. To compare the degree of randomness that different systems produce under time evolution, we look at D_{KL} as a function of the Page limit-normalized entanglement entropy S/S_{max}. This allows for an umambiguous comparison of the degree of randomization between systems under drastically different unitary dynamics beyond the entanglement entropy.

The entanglement level spacing distribution reveals important information regarding the complexity of entanglement that is not captured by the entanglement entropy alone. More precisely, it signals whether a time-evolved state (even if maximally entangled) can be efficiently disentangled *without precise knowledge of the time evolution operator*, which is a highly non-trivial task for generic highly entangled states [28, 33, 130]. Therefore, the distance of the entanglement level distribution to the GUE distribution as a function of the amount of entanglement entropy should be viewed as the distance to the fixed point under chaotic quantum dynamics, that is, the *degree of scrambling*. In fact, we show in this work that D_{KL} can vary considerably between different chaotic systems *even at the same level of entanglement entropy*.

We demonstrate our results by studying dynamics generated by various random unitary circuits that are chaotic, starting from unentangled product states. Con-

cretely, we investigate two types of random circuits operating on non-Abelian anyons (Fig. 4·1): (1) Majorana fermions with random braidings supplemented with random four-body interactions on every four contiguous sites; (2) Fibonacci anyons with random braidings. It is well-known that braidings of Fibonacci anyons alone are capable of universal quantum computation, but braidings of Majorana fermions are not [54, 132]. In the latter case, in order for the final states to reach GUE entanglement spectra, we supplement braidings with random *local* four-Majorana interactions. To gain further insights, we also compare the degree of scrambling of anyon braidings with those of the Sachdev-Ye-Kitaev model of Majorana fermions with all-to-all interactions [133, 134], and random unitary circuits built out of (a) Hadamard (H), $\pi/8$ (T), and CNOT gates, and (b) random unitary circuits built out of two-qubit Haar-random unitaries. We find that, at intermediate times (when the entanglement entropy is still far from maximum), the D_{KL} for the above systems are drastically different at the same normalized entanglement entropy S/S_{max}. This indicates that there is indeed a hierarchy in the degree of randomness produced by different systems at the same amount of entanglement entropy. Interestingly, we find that braiding of Fibonacci anyons randomizes initial product states more efficiently than the universal H+T+CNOT set, which sheds new light on the potential computational power of topological quantum computation. The SYK model, on the other hand, randomizes more efficiently comparing with local random circuit models.

The rest of this chapter is organized as follows. We first introduce the concept of ES statistics and its relevance to entanglement complexity in both quantum circuits and Hamiltonian dynamics in Sec. 4.2. In Sec. 5.4, we introduce the models that we study in this work. The numerical results for D_{KL} are presented in Sec. 4.4. Finally we close with a few remarks regarding future directions (Sec. 4.5).

4.2 Entanglement spectrum statistics and entanglement complexity

We start by introducing the basic concepts of ES statistics and the significance of GUE level spacing statistics in both quantum circuits and Hamiltonian dynamics.

Consider a pure state $|\psi\rangle$ written in some complete local basis $|\psi\rangle = \sum_{\{\sigma\}} \psi(\{\sigma\})|\{\sigma\}\rangle$. From now on we shall drop the "{ }" and denote a collection of degrees of freedom simply as σ, which should be clear from the context. Under a bipartition of the system into two subsystems A and B with Hilbert space dimensions d_A and d_B, we have:

$$\begin{aligned} |\psi\rangle &= \sum_{\sigma} \psi(\sigma)|\sigma\rangle \\ &= \sum_{\sigma_A,\sigma_B} \Psi(\sigma_A,\sigma_B)|\sigma_A\rangle|\sigma_B\rangle, \end{aligned} \tag{4.2}$$

where in the second line we have recasted the wavefunction $\psi(\sigma)$ as a $d_A \times d_B$ matrix $\Psi(\sigma_A,\sigma_B)$. We define the ES of $|\psi\rangle$ under this bipartition as the set of singular values $\{\lambda_k\}$ obtained from a Schmidt decomposition of the matrix $\Psi(\sigma_A,\sigma_B)$ [135]. The entanglement entropy can then be defined using the ES as

$$S = -\sum_k \lambda_k^2 \ln \lambda_k^2 \,. \tag{4.3}$$

Notice that the reduced density matrix of subsystem A is related to Ψ as $\rho_A = \mathrm{tr}_B|\psi\rangle\langle\psi| = \Psi\Psi^\dagger$, so the eigenvalues of ρ_A are simply related to the ES as $\{p_k = \lambda_k^2\}$. Depending on how one partitions the system, Ψ is not necessarily a square matrix. However, in this chapter we restrict ourselves to equi-bipartitions, so that $d_A = d_B$.

Historically, the usefulness of the ES was first recognized in the study of *ground states of gapped systems*, and was proposed as a fingerprint of topological order, and even more generally, symmetry breaking order [22, 136–143]. The entanglement

entropy of ground states of gapped local Hamiltonians is typically low (area law), which means that the ES decays very fast, usually with a large gap separating the dominant singular values, which capture universal aspects of the underlying system, from the rest of the spectrum. Highly excited states, on the other hand, typically have high entanglement entropy (volume law), and in general the ES is not gapped [144].

Important physical characteristics encoded in the ES of highly excited states can be revealed in entanglement level spacing statistics. Let the singular values of an ES be rank-ordered in descending order: $\lambda_i > \lambda_{i+1}$; define the ratio of adjacent gaps in the spectrum as

$$r_k = \frac{\lambda_{k-1} - \lambda_k}{\lambda_k - \lambda_{k+1}}, \tag{4.4}$$

so that $r_k \geq 0$. It was shown [31, 33, 106, 130, 131] that for Haar-random states, the ES can be described in terms of random matrix theory, where the density of states follows the Marchenko-Pastur distribution [72], and the level spacing statistics is given by the Wigner-Dyson distribution [80]

$$P_{\mathrm{WD}}(r) = \frac{1}{Z} \frac{(r + r^2)^\beta}{(1 + r + r^2)^{1+3\beta/2}}, \tag{4.5}$$

with $Z = 4\pi/81\sqrt{3}$ and $\beta = 2$ for GUE distribution. For Poisson distributed spectra, on the other hand, the distribution function takes the form

$$P_{\mathrm{Poisson}} = \frac{1}{(1 + r)^2}, \tag{4.6}$$

which displays no level repulsion as $r \to 0$ and decays as a different power compared to the GUE distribution as $r \to \infty$. The ratio (4.4) probes local (nearest-neighbor) correlations between the singular values in the ES. There exists complementary quantities such as the spectral form factor [131, 145] and spectral rigidity [33] which can probe level repulsion at longer ranges. However we will not study these quantities in this work.

The ES level statistics (4.4) contains information on the "complexity" of a state, that is, states with GUE distributed ES have complex structures of entanglement, whereas states with Poisson distributed ES have simple structures of entanglement, regardless of the *amount* of entanglement. We define the entanglement complexity as the inefficiency of *disentangling* a given state evolved under certain unitary dynamics, *without precise knowledge of the time evolution operator*. In general, this is a highly non-trivial task for generic highly entangled states. However, in Refs. [28, 33], it was shown that one can efficiently disentangle states generated by certain classes of random unitary circuits that are not capable of universal quantum computation (e.g., the Clifford circuits) using a simple Metropolis-like algorithm, *even though these states also reach maximal entanglement entropy*. On the other hand, for states evolved under circuits that are capable of universal quantum computation, such a disentangling algorithm fails. The entanglement entropy growth shows identical behavior in both cases, yet the ES exhibits Poisson distribution in the first case and GUE distribution in the second. Later, Ref. [130] extended this ES-based diagnostic to distinguish between Hamiltonian dynamics that are integrable or non-integrable (either many-body localized or thermalized).

These observations suggest that, in addition to reaching maximal entanglement entropy, time-evolved states of truly chaotic systems should have a GUE distributed ES after a sufficiently long time evolution, i.e., the GUE distributed ES is the fixed point under time evolution, when the initial product states are completely randomized. This motivates us to define the KL divergence between the ES in the process of time evolution and GUE distribution $D_{\mathrm{KL}}[P(r)||P_{\mathrm{GUE}}(r)]$ as a measure of the degree of randomness produced by the evolution. In particular, when compared at the same fraction of maximal entropy S/S_{max}, the difference in D_{KL} reveals the hierarchy of the complexity of scrambling beyond entanglement entropy.

4.3 Non-Abelian random circuit models

In this section, we describe the non-Abelian random circuit models that we use for numerical demonstrations of our results. The basic setup we adopt here is to start from unentangled product states, and then evolve under certain types of unitary dynamics. Random unitary circuits have been intensively studied recently as a theoretical handle to understand quantum chaos [15, 16, 34, 35, 127]. In this work, we will mainly focus on systems of non-Abelian anyons, with braidings and local interactions acting as unitaries operating on anyonic qubits. These systems provide insights into the degree of scrambling in a context that is also relevant to topological quantum computation.

4.3.1 Majorana fermions with random braidings and local interactions

The simplest non-Abelian anyons carrying a multidimensional representation of the braid group are Majorana fermions, or Ising anyons [54, 146]. These are quasiparticle excitations believed to exist in $\nu = 5/2$ fractional quantum Hall systems [147], as well as vortex cores of $p + ip$ topological superconductors [148]. Consider $2n$ Majorana fermions γ_i $(i = 1, 2, \ldots, 2n)$ satisfying $\gamma_i^\dagger = \gamma_i$ and $\{\gamma_i, \gamma_j\} = 2\delta_{ij}$. These can be combined into n complex fermions, such that two Majorana fermions fuse into $i\gamma_{2k-1}\gamma_{2k} = 1 - 2n_k = \pm 1$, where n_k is the fermion occupation number. Hence the total Hilbert space dimension is 2^{n-1} within each fermion parity sector.

Unitary evolutions or "computations" are implemented by adiabatically braiding anyons around one another, which induces a transformation on the Hilbert space corresponding to an element of the braid group B_{2n} [149]. The group B_{2n} is generated by elementary interchanges of neighboring anyons which we denote by T_i (see Fig. 4·2),

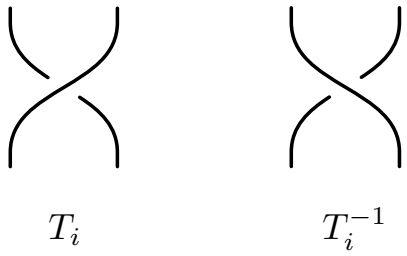

Figure 4·2: (Color online) Generator of the braid group T_i and its inverse T_i^{-1}.

which satisfy the following relations:

$$\begin{aligned} T_iT_j &= T_jT_i, \quad |i-j|>1, \\ T_iT_jT_i &= T_jT_iT_j, \quad |i-j|=1. \end{aligned} \tag{4.7}$$

A nonlocal exchange can be achieved via a sequence of nearest-neighbor exchanges; namely, for exchanging anyons p and q, one has $T_{p,q} = T_{q-1}T_{q-2}\cdots T_{p+1}T_pT_{p+1}^{-1}T_{p+2}^{-1}\cdots T_{q-1}^{-1}$.

Physically, we are interested in unitary representations of the braid group. For the case of Majorana fermions, the braid group representation for the generators is given by [150]:

$$\rho(T_i) = \exp\left(\frac{\pi}{4}\gamma_{i+1}\gamma_i\right) = \frac{1}{\sqrt{2}}(1+\gamma_{i+1}\gamma_i). \tag{4.8}$$

Written explicitly under qubit basis, the braid element can act as either a single-qubit gate or a two-qubit gate, depending on whether the two anyons that are braided belong to the same qubit or not. For example, consider four Majorana fermions $\gamma_1,\ldots,\gamma_4$ defining a four-dimensional Hilbert space $|n_1,n_2\rangle$. One can work out the

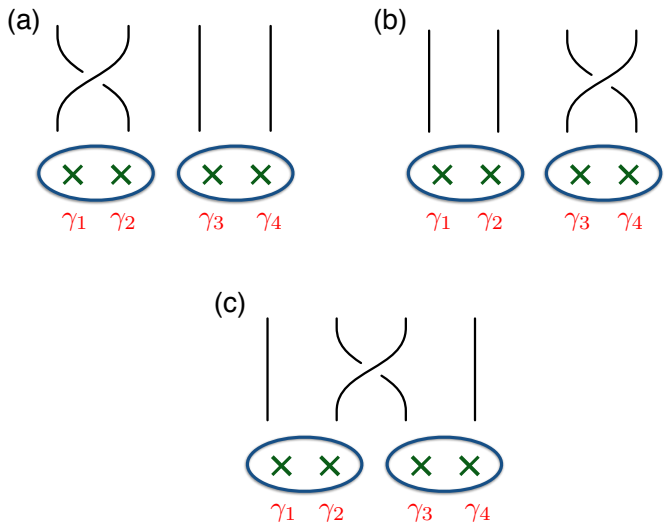

Figure 4·3: (Color online) All possible braid elements acting on four Majorana fermions. (a) $\rho(T_1)$; (b)$\rho(T_3)$; (c)$\rho(T_2)$. The ovals indicate how qubit basis is defined. (a) & (b) act as single-qubit gates, and (c) acts as a two-qubit gate.

action of all possible braids on this Hilbert space as given by (see Fig. 4·3):

$$\begin{aligned}
\rho(T_1)|n_1,n_2\rangle &= e^{i\frac{\pi}{4}(1-2n_1)}|n_1,n_2\rangle, \\
\rho(T_3)|n_1,n_2\rangle &= e^{i\frac{\pi}{4}(1-2n_2)}|n_1,n_2\rangle, \\
\rho(T_2)|n_1,n_2\rangle &= \frac{1}{\sqrt{2}}\left(|n_1,n_2\rangle + i|1-n_1,1-n_2\rangle\right),
\end{aligned} \tag{4.9}$$

where the braids in the first two lines correspond to single-qubit gates, and the third line corresponds to a two-qubit gate. Applying Eq. (4.9) to $2n$ Majorana fermions, one can calculate the unitary transformation under circuits of arbitrary braidings of $2n$ anyons.

Braidings of Majorana fermions are insufficient to create circuits capable of universal quantum computation, which is necessary to fully randomize arbitrary initial states. In fact, the braiding representation presented in Eq. (4.8) essentially cor-

responds to a free fermion system, which fails to even maximally entangle initial product states. Therefore, we must supplement braidings with local interactions in order to have truly chaotic random circuits [151]. We add random local four-body interaction terms involving every four contiguous Majorana fermions $\gamma_j, \ldots, \gamma_{j+3}$, which corresponds to unitary operators

$$U_j = \exp\left(-i\alpha_j \gamma_j \gamma_{j+1} \gamma_{j+2} \gamma_{j+3}\right), \tag{4.10}$$

where $\alpha_j \in [0, 2\pi]$ are random interaction strengths. Now each realization of the random unitary circuit operating on $2n$ Majorana fermions can be built by acting on the anyons with either braiding [Eq. (4.9)] or four-body interaction [Eq. (4.10)] at every single step.

4.3.2 Fibonacci anyons with random braidings

A particular type of non-Abelian anyon that allows for universal quantum computation, and is thus capable of fully randomizing arbitrary initial states, is the Fibonacci anyon [132, 152, 153]. The Fibonacci anyon belongs to the quasiparticle spectrum of $SU(2)_3$ Chern-Simons theory whose non-Abelian part is also equivalent to the $\mathbb{Z}_3$ parafermion theory [154]. It may also be related to the $\nu = 12/5$ fractional quantum Hall state observed in experiments.

The quasiparticle contents in this model are very simple: it contains a single nontrivial quasiparticle denoted as τ and the identity, or vacuum, denoted by $\mathbf{1}$. The nontrivial fusion rule is given by:

$$\tau \times \tau = \mathbf{1} + \tau. \tag{4.11}$$

To define the Hilbert space of a system of multiple anyons, we consider the Fibonacci chain [155, 156] with open boundary condition as shown in Fig. 4·4. This is

essentially a fusion tree drawn in a slightly different orientation. We label states in

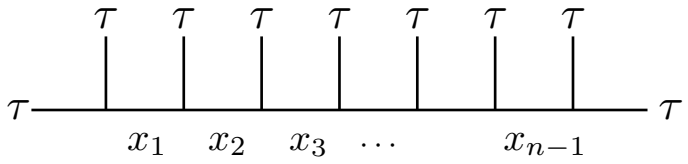

Figure 4·4: (Color online) The fusion tree of a Fibonacci chain consisting of n anyons. States in the Hilbert space are labeled by the degrees of freedom on the horizontal links $|x_1 x_2 \dots x_{n-1}\rangle$, with the additional constraint that there cannot be two **1**'s next to each other.

the Hilbert space corresponding to Fig. 4·4 as $|x_1 x_2 \dots x_{n-1}\rangle$, with $x_i = \tau$ or **1**, for a system of n anyons (the τ's on the two endpoints are considered as boundary conditions). Due to the fusion rule in Eq. (4.11), the allowed configuration must satisfy an additional constraint, namely, there cannot be two **1**'s next to each other. Hence the Hilbert space dimension of n anyons is $\mathrm{Fib}(n+1)$, where $\mathrm{Fib}(n)$ are Fibonacci numbers satisfying $\mathrm{Fib}(n+1) = \mathrm{Fib}(n) + \mathrm{Fib}(n-1)$ and $\mathrm{Fib}(1) = \mathrm{Fib}(2) = 1$. For large n, the Hilbert space dimension of Fibonacci anyons grows as ϕ^n, where the quantum dimension $\phi = (1+\sqrt{5})/2$ is the golden ratio.

The unitary representation of the braid group in terms of Fibonacci anyons can be derived using the R-matrix and the F-matrix of the topological field theory. From now on we shall denote the states of x_i using the language of qubits: $|0\rangle \equiv |x_i = \mathbf{1}\rangle$,

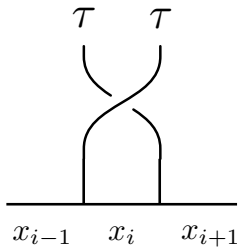

Figure 4·5: (Color online) The effect of braiding two Fibonacci anyons only depends on the configuration of the three qubits in contact with the two anyons: x_{i-1}, x_i, and x_{i+1}.

$|1\rangle \equiv |x_i = \tau\rangle$. We directly list below the action of braiding on the qubit basis as in Eq. (4.9) and provide the derivation in Appendix A. The effect of braiding two adjacent anyons depends only on the configuration of the three qubits in contact with the two anyons, see Fig. 4·5. The representation of the braiding in the qubit basis is

$$\begin{aligned}
\rho(T_i)\,|101\rangle &= -e^{-i\pi/5}/\phi\,|101\rangle - ie^{-i\pi/10}/\sqrt{\phi}\,|111\rangle, \\
\rho(T_i)\,|111\rangle &= -ie^{-i\pi/10}/\sqrt{\phi}\,|101\rangle - 1/\phi\,|111\rangle, \\
\rho(T_i)\,|110\rangle &= -e^{-2\pi i/5}\,|110\rangle, \\
\rho(T_i)\,|011\rangle &= -e^{-2\pi i/5}\,|011\rangle, \\
\rho(T_i)\,|010\rangle &= e^{-4\pi i/5}\,|010\rangle,
\end{aligned} \tag{4.12}$$

where we have suppressed the labels for the rest of the qubits.

The "no consecutive **1**s" constraint imposed on the states of adjacent qubits means that the Hilbert space dimension of the full chain is *not* equal to the product of the subsystem Hilbert space dimensions under a bipartition, i.e. $d \neq d_A d_B$.

4.3.3 Hadamard, $\pi/8$, and CNOT gate

In addition to the two non-Abelian random circuit models introduced above, we also study three more cases as a comparison. The first system is the random circuits built out of Hadamard, $\pi/8$, and CNOT gates. The action of these gates is most conveniently expressed in terms of the following unitary matrices:

$$H = \frac{1}{\sqrt{2}}\begin{pmatrix} 1 & 1 \\ 1 & -1 \end{pmatrix}, \qquad T = \begin{pmatrix} 1 & 0 \\ 0 & e^{i\pi/4} \end{pmatrix},$$
$$\text{CNOT} = \begin{pmatrix} 1 & 0 & 0 & 0 \\ 0 & 1 & 0 & 0 \\ 0 & 0 & 0 & 1 \\ 0 & 0 & 1 & 0 \end{pmatrix}. \tag{4.13}$$

It can be shown that H, T and CNOT combined together is capable of universal quantum computation [3], and hence is also capable of fully randomizing arbitrary initial states.

4.3.4 Two-qubit Haar-random unitaries

In this case, we study the same setup as in previous work by considering random unitary circuits built from two-qubit Haar-random unitary gates, which are drawn from the uniform probability distribution on the unitary group for two qubits $U(4)$ [15, 34]. Here we shall only use local gates which act on two nearest-neighboring qubits at a single step.

4.3.5 SYK model

Finally, we consider the SYK model consisting of N Majorana fermions with all-to-all random interactions [133, 134]. The main difference from all previous cases is that this system undergoes Hamiltonian dynamics with energy conservation, instead of random unitary dynamics. The Hamiltonian of the SYK model is:

$$\mathcal{H} = \sum_{ijkl} J_{ijkl}\gamma_i\gamma_j\gamma_k\gamma_l, \tag{4.14}$$

where the couplings J_{ijkl} are real Gaussian random variables with zero mean and variance $\overline{J_{ijkl}^2} = 3!J^2/N^3$. This model is exactly solvable in the large-N limit, with a Lyapunov exponent obtained from the OTOC saturating the bound $\lambda_L = 2\pi/\beta$, where β is the inverse temperature [113, 118]. Hence the SYK model is often referred to as being maximally chaotic. Moreover, the eigenstates of the SYK model have been shown to be thermalizing, with entanglement entropies obeying volume law scaling [157–160]. It is thus interesting to look at the degree of scrambling using our measure of D_{KL} and compare with the previous cases.

We consider pure states obtained from a *quantum quench* of an unentangled prod-

uct state with the Hamiltonian of Eq. (4.14) [161, 162]. One can explicitly construct a representation for the Majorana field operators in terms of Pauli matrices using the following Jordan-Wigner transformation:

$$\gamma_{2k-1} = \sigma_k^x \prod_{i=1}^{k-1} \sigma_i^z, \qquad \gamma_{2k} = \sigma_k^y \prod_{i=1}^{k-1} \sigma_i^z, \tag{4.15}$$

which maps the Hamiltonian (4.14) to a spin system.

4.4 Numerical results

We now present our numerical calculations of D_{KL} as a function of $S/S_{\max}$ for models A-E as explained in previous sections. Here the $S_{\max}$ denotes the maximal Page entropy of a Haar-random state given by [27]:

$$S_{\max} = \ln d_A - \frac{d_A}{2d_B}, \quad d_A \leq d_B \tag{4.16}$$

where $d_A = d_B = \mathrm{Fib}(n_A + 2)$ for the Fibonacci anyon model with n_A qubits (not anyon number!) in subsystem A, and $d_A = d_B = 2^{n_A}$ for all other cases [163].

For both the Majorana fermion circuit and the SYK model, the global fermion parity is conserved, and physically one can only create states within a fixed fermion parity sector: $i^n \gamma_1 \gamma_2 \cdots \gamma_{2n} |\psi\rangle = \pm |\psi\rangle$. As a consequence of that, the reduced density matrix ρ_A will be block-diagonal with two blocks corresponding to even/odd parities respectively, and hence the ES statistics of the full spectrum will be a mixture of two sectors and yields a Poisson distribution. One way of working around this is to study the ES statistics within each block. However, in order to obtain a denser spectrum without having to double the total number of sites, a more convenient way is to simply start with random product states that mix the two parity sectors. The physics of scrambling should not be affected by this choice, and one should view this as a theoretical probe, not the modeling of a physical system.

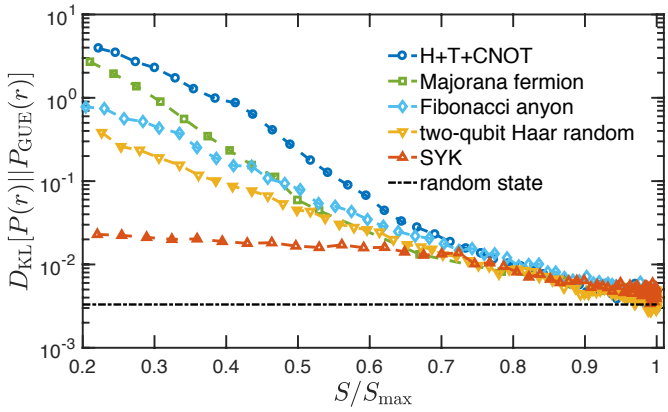

Figure 4·6: (Color online) D_{KL} as a function of S/S_{max} for different models. At intermediate times, one clearly observes a hierarchy of D_{KL} among various chaotic systems *even at the same amount of entropy*. The horizontal dotted dashed line corresponds to the D_{KL} calculated for Haar-random states, which serves as a lower bound numerically. We only look at times after $S/S_{\mathrm{max}} > 0.2$ when we have enough non-zero singular values in each ES to study statistics. For each ES, singular values smaller than 10^{-12} are discarded. The data are obtained for: $N = 28$ Majorana fermions (equivalently 14 qubits) for the SYK model, averaged over 2000 realizations; $n = 23$ anyons (equivalently 22 qubits) for the Fibonacci anyon model, averaged over 1000 realizations; and 16 qubits averaged over 1000 realizations for all other cases.

The numerical results are summarized in Fig. 4·6. Remarkably, we find that there is a clear hierarchy of D_{KL} among various models *even at the same amount of entropy*. Since D_{KL} quantifies how close a given state is to a Haar-random state, this result reveals the hierarchy in the degree of randomness produced by different unitary evolutions beyond the entanglement entropy. As shown in Fig. 4·6, at intermediate times (when the entanglement entropy is still far from maximum), the H+T+CNOT gate set turns out to be the least efficient scrambler among all cases. This result shows that, although the universal set of gates is capable of scrambling initial product states, at intermediate steps, the degree of randomness of such states are in fact quite low. In particular, in this regime, the states generated by H+T+CNOT gates are much less random than those generated by two-qubit Haar-random unitary circuits, at the

same amount of entanglement entropy.

Interestingly, the Fibonacci anyon model randomizes initial product states more efficiently than the H+T+CNOT gate set. Traditionally, there has been considerable effort in designing sophisticated compiling algorithms to build H, T, and CNOT gates from either the Ising or Fibonacci anyons [151–153]. While this is necessary for implementations of real-world quantum algorithms written in terms of universal gates, our results imply that a better strategy may be to bypass the compilation of standard gates completely and focus on computations carried out directly with braiding. Conversely, one can ask how to approximate an arbitrary anyonic braid by combining universal gates. Our results indicate that the appropriate combination may be quite complicated.

The SYK model, in spite of having additional energy conservation, generates a much higher degree of randomness than the local random unitary circuit models. This result may not be completely surprising since the SYK model has all-to-all interactions, hence the large number of independent random couplings in the Hamiltonian makes the corresponding unitary resemble a Haar-random unitary acting on n qubits. However, we now have a concrete way to quantify the degree of randomness that this system produces under time evolution, which can be compared with systems under drastically different dynamics.

It is important to emphasize that, by looking at D_{KL} as a function of the normalized entanglement entropy S/S_{max}, we are not comparing the 'speed' of information scrambling that people usually think of. After all, it is not sensible to talk about a unique time unit for drastically different systems, namely, random unitary circuits versus local or non-local Hamiltonian systems. Rather, we compare the degree of randomness produced by different systems when the same fraction of the systems becomes entangled, that is, at the same S/S_{max}. One may alternatively view the parametriza-

tion $S/S_{\max}$ as a 'proper time' which eliminates real time or circuit depths and allows different models to be compared on equal footing. In Appendix B, we show that this parametrization is insensitive to different system sizes, whereas the real time or circuit depth is not.

Finally, there is an interesting observation from Fig. 4·6 regarding the late time behavior of D_{KL} (when the entanglement entropy is close to reaching its maximum). Starting from $S/S_{\max} \approx 0.7$, the curves for different cases seem to collapse on top of each other. It is tempting to think of this as a universal late-time behavior of chaotic systems as a function of the entropy, in the sense that the discrepancies in the degree of randomness they produce disappear prior to reaching maximal entanglement entropy.

4.5 Summary and outlook

The notion of information scrambling bridges many different areas in physics, including quantum many-body physics, quantum computation and quantum information, quantum statistical mechanics and quantum gravity. Scrambling can exhibit different complexities depending on the degree of randomness it produces, which very often cannot be captured by the entanglement entropy alone [29, 30]. In this work, we propose a new metric to quantify the degree of scrambling in the form of the Kullback-Leibler divergence D_{KL}, which is a measure of the distance to universal ES level spacing distribution corresponding to complete randomization. The universal distribution of the ES is intimately tied to the complexity of entanglement in a given state, which is not reflected in the net amount of entanglement entropy. We demonstrate numerically that there is indeed a hierarchy of D_{KL} among various models, which defines the degree of scrambling in a model-independent manner.

This work opens interesting directions for future research. Our methodology can

be extended to a plethora of other quantum Hamiltonian systems, such as quantum spin chains. In particular, it was pointed out in Ref. [130] that many-body localized (MBL) systems — although they do not thermalize and hence do not reach Page entropy — also reach GUE distributed ES asymptotically as $1/\ln t$, where t is real time. Therefore, D_{KL} could potentially be a useful quantity to compare the degree of scrambling of different MBL systems, without the ambiguity of time units.

Furthermore, it has been conjectured that quantum chaos underlies the computational complexity of quantum circuits or, more generally, quantum channels [124, 145]. From the topological quantum computation perspective, our results imply that braiding non-Abelian anyons may well be a much faster quantum computer than the universal gate set. This suggests that there might be more efficient ways of utilizing the computational power of braidings, than trying to design the universal gates using braidings.

Acknowledgments

We would like to thank Meng Cheng, Yingfei Gu, and Eric Rowell for useful discussions, and Marko Žnidarič for useful comments on the manuscript. We thank Zi-Wen Liu for pointing out refs. [29, 30] to us and helpful discussions.

A Derivation of the braid group representation in terms of Fibonacci anyons

We present the derivation of the action of braiding operations on qubit basis of Fibonacci anyons, whose results are summarized in Eq. 4.12. We shall use the language of F and R matrices to derive these results. There also exists an alternative derivation by drawing a connection between the braid group representation and the Temperley-Lieb algebra. We refer the interested readers to refs. [164, 165].

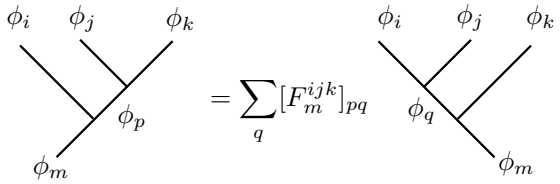

Figure ·7: (Color online) The F-matrix relates the two different basis states resulting from fusing four anyons in different orders.

The R-matrix and F-matix are important data characterizing a given conformal field theory or topological quantum field theory. The R-matrix R_c^{ab} specifies the phase resulting from braiding anyons of type a and b which fuse into type c. For the Fibonacci anyons, the R-matrix is given by [54]:

$$R = \begin{pmatrix} e^{4\pi i/5} & 0 \\ 0 & -e^{2\pi i/5} \end{pmatrix}, \tag{17}$$

or, $R_{\mathbf{1}}^{\tau\tau} = e^{4\pi i/5}$, $R_{\tau}^{\tau\tau} = -e^{2\pi i/5}$. The F-matrix $[F_m^{ijk}]_{pq}$, on the other hand, specifies the unitary transformation between two difference bases, when four anyons are fused in different orders (see Fig. ·7). For Fibonacci anyons, $F_{\mathbf{1}}^{\tau\tau\tau}$ can be easily seen to be trivially identity. However, $F_{\tau}^{\tau\tau\tau}$ is non-trivial and given by [54]:

$$F_{\tau}^{\tau\tau\tau} = \begin{pmatrix} 1/\phi & 1/\sqrt{\phi} \\ 1/\sqrt{\phi} & -1/\phi \end{pmatrix}, \tag{18}$$

where $\phi = (1+\sqrt{5})/2$ as defined earlier. Notice that the F-matrix satisfies $F^{-1} = F$.

As we explained in Fig. 4·5, the action of braiding on the qubit basis only depends on the configuration of three adjacent qubits. One can tilt Fig. 4·5 and draw it in exactly the same way as in Fig. ·7, so that the action of braiding can be determined using the F and R matrices. Let us give an example of the state $|x_{i-1}x_ix_{i+1}\rangle = |101\rangle$. This configuration corresponds to the fusion tree depicted in Fig. ·8. One will first need to convert to the basis where the two anyons being braid (top right) fuse into a definite anyon type using the (inverse of) F-matrix, then followed by applying the R-

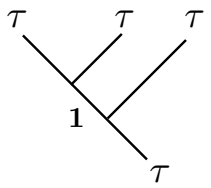

Figure ·8: (Color online) A qubit configuration $|x_{i-1}x_ix_{i+1}\rangle = |101\rangle$ corresponding to Fig. 4·5 drawn in the fusion tree orientation.

matrix. Finally, one converts back to the original basis by applying F again. Hence, the action of braiding on this configuration is given by the first row of the matrix FRF^{-1}, which is:

$$FRF^{-1} = \begin{pmatrix} -e^{-i\pi/5}/\phi & -ie^{-i\pi/10}/\sqrt{\phi} \\ -ie^{-i\pi/10}/\sqrt{\phi} & -1/\phi \end{pmatrix}. \tag{19}$$

Eq. 19 leads to the first line of Eq. 4.12 shown in the text. One can also check in a similar way the rest of the results claimed in Eq. 4.12.

B Finite-size effect on the parametrization $S/S_{\max}$

In this section, we show that the parametrization $S/S_{\max}$ is insensitive to finite-size effect, whereas the real time or circuit depth is not. Therefore, the main result that we present in Fig. 4·6 holds even with the slight non-uniformity in our choices of system sizes for different models.

We take the case of universal set of gates H+T+CNOT as an example. In Fig. ·9(a), we plot D_{KL} as a function of $S/S_{\max}$ for different system sizes. We find that the curves almost fall on top of one another, indicating that the ratio $S/S_{\max}$ measures the fraction of the degrees of freedom of the system that becomes entangled and is thus insensitive to different system sizes. On the other hand, if we plot D_{KL} as a function of the circuit depth (i.e. real time) as in Fig. ·9(b), we find that there is a systematic shift of the curves upon changing system sizes, namely, D_{KL} gets bigger

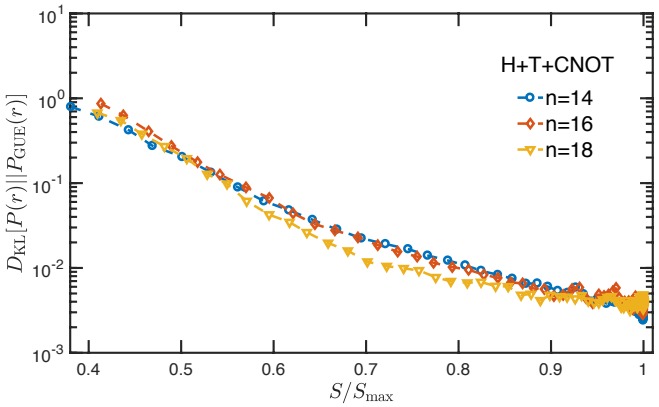

(a)

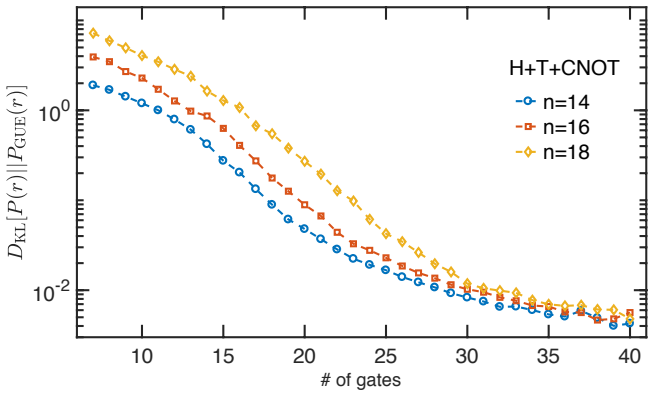

(b)

Figure ·9: (Color online) (a)D_{KL} as a function of S/S_{max} for the H+T+CNOT gate set for different system sizes; (b)D_{kL} as a function of circuit depth (i.e. real time) for different system sizes. One finds that the curves collapse with the parametrization S/S_{max} but not with the circuit depth.

at the same circuit depth as the system size increases. This is consistent with the expectation that it takes a longer real time for larger systems to scramble to the same degree. However, this effect is indeed eliminated with the parametrization S/S_{max}, which can be viewed as a 'proper time' that is robust against slight non-uniformity in the system sizes.

Part II: Novel architectures for quantum computation

Chapter 5

Optimizing variational quantum algorithms using Pontryagin's minimum principle

Abstract

We use Pontryagin's minimum principle to optimize variational quantum algorithms. We show that for a fixed computation time, the optimal evolution has a bang-bang (square pulse) form, both for closed and open quantum systems with Markovian decoherence. Our findings support the choice of evolution ansatz in the recently proposed Quantum Approximate Optimization Algorithm. Focusing on the Sherrington-Kirkpatrick spin-glass as an example, we find a system-size independent distribution of the duration of pulses, with characteristic time scale set by the inverse of the coupling constants in the Hamiltonian. The optimality of the bang-bang protocols and the characteristic time scale of the pulses provide an efficient parameterization of the protocol and inform the search for effective hybrid (classical and quantum) schemes for tackling combinatorial optimization problems. Furthermore, we find that the success rates of our optimal bang-bang protocols remain high even in the presence of weak external noise and coupling to a thermal bath.[1]

[1]The contents of this chapter were published in Physical Review X, **7**, 021027 (2017).

5.1 Introduction

Quantum Annealing (QA) aims to solve computational problems by using a guided quantum drive. The dynamics is generated by a time-dependent Hamiltonian along a trajectory that ends at a final target Hamiltonian whose ground state contains the solution of the problem [36, 166, 167]. QA is based on the adiabatic theorem, which guarantees that if the Hamiltonian is changed sufficiently slowly, transitions to excited states are suppressed during the adiabatic evolution, thus preparing states that are close to the target ground state. Unfortunately, the adiabatic condition that ensures that the system remains in the instantaneous ground state leads to long time scales for the solution of hard computational problem. Within the framework of adiabatic computation, there has been several theoretical proposals on the optimizations of the Quantum Adiabatic Algorithm (QAA), such as heuristic guesses for the initial state [168], increasing the minimum gap [169, 170], and the quantum adiabatic brachistochrone formulation [171].

The adiabatic trajectory is not the only path for reaching the ground state of a final Hamiltonian that encodes the solution of the computational problem. More generally, one could imagine many other paths, including those where the Hamiltonian is varied rapidly, that land at the desired state or, of practical interest, reach low energy states. In fact, it has been already found that for certain hard instances of problems, fast nonadiabatic paths can sometimes prevent the system from getting stuck at local minima, thus improve the search results [44, 45, 172]. The Variational Quantum Algorithm (VQA) is an example where one searches for such possible paths, using optimization of the outcome via the variation of a fixed number of parameters in the protocol. A hybrid machine, combining classical optimization and quantum evolution, optimizes the variational parameters. Such hybrid variational approaches have proved useful in the context of quantum state preparation [173–176]. Recently, Ref.

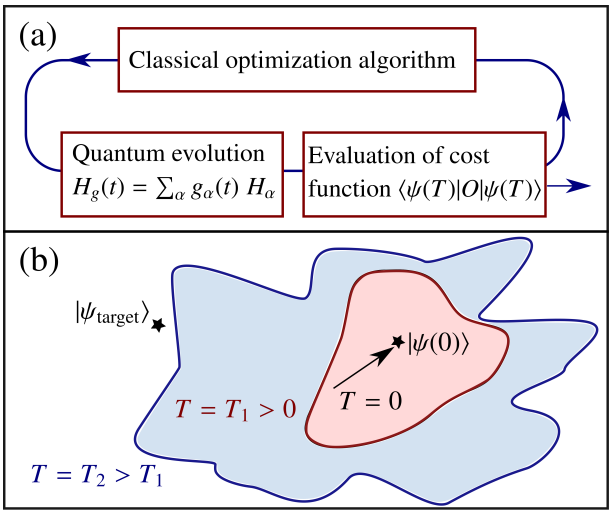

Figure 5·1: (a) Variational quantum algorithm as a closed-loop learning control problem. (b) Increasing the total time expands the set of final states that one can reach with the variational protocols. The optimal protocol for a given time generates the closest state to a low energy target state within this reachable set.

[47] introduced a variational quantum eigensolver (VQE) for applications in quantum chemistry. This idea was further explored in [48–51, 177] and experimentally tested in [178–180]. In a related approach [46, 181–183], Farhi *et al.* introduced a Quantum Approximate Optimization Algorithm (QAOA) for combinatorial optimization problems based on a parameterized square-pulse ansatz for dynamical evolution of the solver.

In this chapter, we make a connection between VQA and optimal control theory [184–187]. VQA is essentially an adaptive feedback control [188, 189] of a quantum system with the objective function encoding the solution of a computational problem, see Fig. 5·1(a). It utilizes a hybrid system comprised of a classical computer that searches for the optimal variational protocol using measurements done on a quantum machine that generates the final states corresponding to different variational protocols, via a closed-loop learning method [190].

Using Pontryagin's minimum principle of optimal control, we show that the opti-

mal protocol for VQA has a "bang-bang" form. Our results put the bang-bang ansatz of QAOA on a rigorous ground in contrast to VQA with a continuous-time evolution. A comparison of the performance of the optimal nonadiabatic bang-bang protocol with conventional (linear ramp) QAA demonstrates that the former significantly reduces error in the final state in the absence of noise or decoherence. The advantage over the linear ramp protocol in QAA survives weak dephasing white noise as well as weak coupling to a thermal bath. Furthermore, we perform a quantitative analysis of the characteristics of these optimal protocols. We numerically find a system-size independent distribution function for the duration of individual pulses, which may facilitate the development of effective algorithms for the classical optimizer through an efficient representation of the protocol with few variational parameters. Interestingly, each of the pulses in our bang-bang protocols contains commuting (either one-qubit or two-qubit) terms. Thus our protocol can be implemented by applying a sequence of one-qubit gates [generated by the initial Hamiltonian, $g = 0$ in Eq. (5.9)] and two-qubit gates generated by the problem Hamiltonian ($g = 1$).

5.2 Variational Quantum Algorithm

Consider a computational optimization problem such as finding a sequence of N bits that minimizes a certain function of all of the bits. To solve this problem with VQA, we consider a system of N qubits with a parameterized Hamiltonian

$$H_g(t) = \sum_\alpha g_\alpha(t)\ H_\alpha. \tag{5.1}$$

Generically, we can cast the problem into generating a state $|\psi\rangle$ that minimizes a certain cost function such as the expectation value of an operator O with respect to $|\psi\rangle$. A common example is finding the ground state of a disorderd classical Ising Hamiltonian [191], where the operator O is a Hamiltonian diagonal in the computa-

tional basis. In the context of quantum chemistry, VQE considers the operator O to be the Hamiltonian of a molecule [48].

The essence of VQA, as depicted in Fig. 5·1, is finding the time-dependent parameters $g_\alpha(t)$ over a time period T such that

$$|\psi(T)\rangle = \mathcal{T} \mathrm{e}^{-i\int_0^T H_g(t)dt} |\psi(0)\rangle \,, \tag{5.2}$$

minimizes a cost function $\langle\psi(T)|O|\psi(T)\rangle$. Generically, the controls $g_\alpha(t)$ belong to a permissible set determined by the experimental setup. A common such set is given by simple bounds as seen in Eq. (5.3) below. The ideal solution could be a unique state $|\psi_{\text{target}}\rangle$ [as depicted in Fig.5·1(b)] that is the ground state of the target Hamiltonian or more generally a set of states in the Hilbert space with an optimal figure of merit. One can either fix the initial state $|\psi(0)\rangle$ or add it to the list of the variational parameters (here we fix it motivated by experimental constraints). Generally, the longer the total time T, the closer we can get to an ideal solution.

One way to view this is to consider the reachable set, i.e., the set of all the final states one can reach by using one of the infinite number of permissible controls. The reachable set, naturally, grows with T (in fact, if $g_\alpha = 0$ is allowed, the reachable set for $T = T_1$ is strictly a subset of the reachable set for $T = T_2 > T_1$). As seen in Fig. 5·1(b), there could be a critical time beyond which the reachable set includes the target state and an exact solution is possible. There is no advantage in increasing T beyond this critical time. Generically, for smaller T, where the reachable set does not include the target state, the optimal protocols are highly constrained as they should prepare the closest point(s) of the reachable set to the target. For times longer than the critical time mentioned above, we expect an infinite number of protocols to produce the target as the evolution has extra time to meander in the Hilbert space. Our strategy is to fix T and find the best variational protocol $g_\alpha(t)$. If the solution

is not acceptable, we can increase T. Next we discuss how Pontryagin's minimum principle from optimal control theory determines the form of optimal $g_\alpha(t)$ functions.

5.3 Pontryagin's minimum principle applied to VQA

5.3.1 Bang-bang optimal protocols

The parameters in Hamiltonian (5.1) are generically constrained by their range:

$$g_\alpha^{\min} \leqslant g_\alpha(t) \leqslant g_\alpha^{\max} \tag{5.3}$$

during the evolution $0 < t < T$. Eq. (5.3) implies that, by assumption, each g_α can be tunned in the above range independently of the values of the other control parameters. For fixed initial state $|\psi(0)\rangle$, the coupling constants $g_\alpha(t)$ uniquely determine the final wave function. Consequently, the cost function, which we take as an arbitrary function of the final state, is a functional of $g_\alpha(t)$

$$F[\{g_\alpha(t)\}] = \mathcal{F}(|\psi(T)\rangle). \tag{5.4}$$

The Pontryagin's minimum principle [185] is directly applicable here. Briefly, this theorem states that for a set of dynamical variables $\boldsymbol{x}$ evolving from given initial values $\boldsymbol{x}(0)$ with the equations of motions $\dot{\boldsymbol{x}} = \boldsymbol{f}(\boldsymbol{x}, \boldsymbol{g})$, where $\boldsymbol{g}$ are a set of control functions, the control functions $\boldsymbol{g}^*$ that minimize an arbitrary function $\mathcal{F}[\boldsymbol{x}(T)]$ of the final values of the dynamical variable satisfy

$$\mathcal{H}(\boldsymbol{x}^*, \boldsymbol{p}^*, \boldsymbol{g}^*) = \min_{\boldsymbol{g}} \mathcal{H}(\boldsymbol{x}^*, \boldsymbol{p}^*, \boldsymbol{g}) \tag{5.5}$$

at any point in time and for each of the control functions. The optimal-control Hamiltonian is defined as $\mathcal{H}(\boldsymbol{x}, \boldsymbol{p}, \boldsymbol{g}) \equiv \boldsymbol{f}(\boldsymbol{x}, \boldsymbol{g}) \cdot \boldsymbol{p}$ for conjugate variables $\boldsymbol{p}$ that evolve as $\dot{\boldsymbol{p}} = -\partial_{\boldsymbol{x}} \mathcal{H}$ with boundary conditions $\boldsymbol{p}(T) = \partial_{\boldsymbol{x}} \mathcal{F}[\boldsymbol{x}(T)]$. Here the "$*$"

superscript indicates the optimal solution corresponding to $\boldsymbol{g}^*$.

An important consequence of Eq. (5.5) is that if the equations of motion for $\boldsymbol{x}$, and consequently the optimal-control Hamiltonian $\mathcal{H}$, are linear in $\boldsymbol{g}$, generically, the optimal protocol is bang-bang, i.e., at any time during the evolution we have $g_\alpha^*(t) = g_\alpha^{\min}$ or $g_\alpha^*(t) = g_\alpha^{\max}$. This follows from the fact that at any point in time we need to choose g_α to minimize $\mathcal{H}(\boldsymbol{x}^*, \boldsymbol{p}^*, \boldsymbol{g})$. If the sign of the coefficient of g_α in the optimal-control Hamiltonian is positive (negative), we should then choose the smallest (largest) g_α from the permissible range (5.3). In other words, the optimal protocol for each control function involves a sequence of sudden jumps between its minimum and maximum permissible values. The only caveat for the above argument is the possibility that the coefficient of a particular g_α in $\mathcal{H}(\boldsymbol{x}^*, \boldsymbol{p}^*, \boldsymbol{g})$ vanishes over a finite interval (since the sign of this coefficient determines whether we should choose the minimum or maximum value). We expect this special scenario to be nongeneric particularly for the disordered systems considered in the present work.

In the quantum mechanical context, if the physical Hamiltonian is linear in the controls, the equations of motion and consequently the optimal-control Hamiltonian will also be linear, giving rise to bang-bang protocols as verified in several recent studies on optimal topological quantum computing [192, 193]. To find the protocol $\boldsymbol{g}$ that minimizes the cost function in our case, we expand the wave function in a complete orthonormal basis, e.g., the computational basis $|z\rangle$ as $|\psi(t)\rangle = \sum_z A_z(t)|z\rangle$ and treat the real and imaginary parts of the amplitudes $A_z(t)$ as dynamical variables, which evolve according to the Schrödinger equation

$$\dot{A}_z^R = \frac{1}{2}\sum_{\alpha,z'} g_\alpha \left[\left(H_\alpha^{zz'} + H_\alpha^{z'z}\right) A_{z'}^I - i\left(H_\alpha^{zz'} - H_\alpha^{z'z}\right) A_{z'}^R\right], \tag{5.6}$$

$$\dot{A}_z^I = \frac{1}{2}\sum_{\alpha,z'} g_\alpha \left[-\left(H_\alpha^{zz'} + H_\alpha^{z'z}\right) A_{z'}^R - i\left(H_\alpha^{zz'} - H_\alpha^{z'z}\right) A_{z'}^I\right], \tag{5.7}$$

where $H_\alpha^{zz'} \equiv \langle z|H_\alpha|z'\rangle$ and $A_z^{R,I} \equiv \mathrm{Re}, \mathrm{Im}(A_z)$. Clearly, these equations of motion are linear in the control functions g_α and the cost function (5.4) is a function of only the final values of the dynamical variables. Thus, the argument above holds and the optimal protocol is generically bang-bang regardless of the number of variational parameters. We remark that our optimal bang-bang protocol is nonadiabatic by construction, and we put no constraint on maximizing the degree of adiabaticity. The value of this result hinges upon the time scale over which a coupling constant is held fixed. The longer this time scale, the fewer parameters (switching times) are needed to represent the protocol. In fact, in the limit where this time scale goes to zero, any protocol can be approximated by a sequence of square pulses through Trotterization. In this work, we find that the time scale above is indeed finite and is set by the energy scale of the Hamiltonian for the Sherrington-Kirkpatrick (SK) Ising spin-glass model [see Eq. (5.9)].

5.3.2 Presence of decoherence

From a practical point of view, it is important to assess the validity of the closed system findings in the presence of decoherence. Again, a straightforward application of the Pontryagin principle extends the above results for a closed system evolution to an open quantum system with Markovian dynamics described by a Lindblad equation

$$\frac{d\rho}{dt} = -i\left[\sum_\alpha g_\alpha(t)\ H_\alpha,\ \rho\right] + \sum_\beta f_\beta(t)\left(2F_\beta\ \rho\ F_\beta^\dagger - \left\{F_\beta^\dagger F_\beta,\ \rho\right\}\right) \tag{5.8}$$

where the optimal protocol $\{g_\alpha(t), f_\beta(t)\}$, if controllable, are of type bang-bang. This is due to the linearity of the dynamical equation (5.8). A decoherence operator F_β can represent either noise in the Hamiltonian parameters (in which case, F_β is Hermitian [194, 195]) or an engineered bath [196]. In the former case, f_β's are constant rates of noise processes and in the latter, $f_\beta(t)$'s are control knobs that the Pontrya-

gin's minimum principle says should vary in bang-bang form for an optimal protocol. In the rest of the chapter, we only focus on closed systems Schrödinger dynamics when finding the optimal protocol. We do, however, discuss the effects of noise and open-system dynamics on our optimal protocols.

5.4 VQA for the SK Spin-Glass Model

We now focus on a canonical problem in combinatorial optimization, namely the SK Ising spin glass [53] with the energy function

$$C = \frac{1}{\sqrt{n}} \sum_{i,j=1}^{n} J_{ij}\sigma_i^z\sigma_j^z + \sum_{i=1}^{n} h_i\sigma_i^z. \tag{5.9}$$

where J_{ij} and h_i are independent Gaussian random variables with zero mean and variance $J^2 = h^2 = 1$, and each σ^z spin can take the values ± 1. The goal is to minimize C over all the 2^n spin configurations. A multitude of practical combinatorial optimization problems map to this model. The computational cost of finding the minimum with classical algorithms is exponential in n.

In analogy with the simple instances of quantum annealing, we focus on the case with only one control function $g(t)$ and use the following parameterized Hamiltonian:

$$H_g(t) = g(t)C + [1 - g(t)]B, \tag{5.10}$$

with the operator $B \equiv -\sum_{i=1}^{n} \sigma_i^x$ representing a transverse field, which generates quantum fluctuations.

For the initial state, we choose the ground states of B. It is easy to prepare product state $|\psi(0)\rangle = \prod_i \left(\frac{|\uparrow\rangle_i + |\downarrow\rangle_i}{\sqrt{2}}\right)$ commonly used in other schemes such as the QAA. Here $\sigma_i^z|\uparrow\rangle_i = |\uparrow\rangle_i$ and $\sigma_i^z|\downarrow\rangle_i = -|\downarrow\rangle_i$. We would like to minimize the cost function $\langle\psi(T)|C|\psi(T)\rangle$. In the adiabatic scheme, a smooth ramp such as $g(t) = \frac{t}{T}$ is applied for $0 < t < T$ and we can generate large overlap with the ground state

of C in the limit of large T. Here, we allow for arbitrary time dependence of the control function in the fixed range $0 \leqslant g(t) \leqslant 1$. According to the general argument of Sec. 5.3.1, the optimal solution is bang-bang.

As discussed in the introduction, in VQA a classical optimization algorithm commands a quantum system to find the optimal protocol variationally from measurement of the cost function for many protocols. This requires many repetitions and it is to our advantage to use the shortest possible time T for which the final state has an acceptable overlap with the ground state of C (projective measurement is ultimately used in generating the ground state). In the adiabatic scheme, we only need one shot but there are important restrictions from the small energy gaps along the adiabatic trajectory, which can lead to exceedingly long time scales, over which quantum coherence cannot be even approximately sustained. Furthermore, the presence of noise or modulation in the control fields places important limitations on adiabatic schemes due to the emergence of the recently proposed noise-induced anti-adiabaticity in the long-time limit [197]. Unlike QAA, which relies on the adiabatic theorem, VQA has no known connection to instantaneous ground states and the minimum gap to excitations as transitions to excited states during the time evolution are allowed as long as the system eventually lands at the ground state of the final Hamiltonian.

Given the limitations of adiabatic scheme, a quantum approximate algorithm has been introduced for solving combinatorial optimization problems [46, 181–183] in the spirit of VQA. The algorithm of Ref. [46] uses an ansatz

$$|\boldsymbol{\gamma}, \boldsymbol{\beta}\rangle = U(B, \beta_p)\, U(C, \gamma_p) \cdots U(B, \beta_1)\, U(C, \gamma_1)\, |\psi(0)\rangle, \tag{5.11}$$

where the evolution operators are given by $U(C, \gamma) = e^{-i\gamma C}$ and $U(B, \beta) = e^{-i\beta B}$. The integer p is a parameter characterizing a variational ansatz.

For a given p, the goal of the algorithm is to find a set of variational parameters

that minimizes the expectation value of $F_p(\boldsymbol{\gamma}, \boldsymbol{\beta}) = \langle \boldsymbol{\gamma}, \boldsymbol{\beta}| \, C \, |\boldsymbol{\gamma}, \boldsymbol{\beta}\rangle$, which ensures that the state $|\boldsymbol{\gamma}, \boldsymbol{\beta}\rangle$ approaches the ground state of C. Physically, the ansatz describes time evolution for a total time $T = \sum_{i=1}^{p} (\gamma_i + \beta_i)$, and a sequence of sudden switching between the Hamiltonians B and C. While this ansatz with a finite p is an intelligent guess, the result that we derived using Pontryagin's minimum principle implies that given bounded independent control of Hamiltonian terms, the ansatz (5.11) is the optimal choice for a VQA approach to optimization. We reiterate that B and C are each a sum of commuting one- and/or two-qubit terms. Therefore, our protocol can be interpreted as a sequence of simple gates. Estimating the required p requires an analysis of the characteristic time scales of the pulses, which we carry out in this work.

5.5 Numerical studies

We start by verifying for small system sizes and short annealing times that the optimal annealing protocol is indeed bang-bang, by using a Metropolis Monte Carlo (MC) algorithm, which makes no assumptions about the nature of the protocol. We divide the total time T into S slices of duration $\delta t = T/S$ and use a piece-wise constant protocol. The method approaches an unbiased optimization, i.e., it explores all permissible controls and chooses the optimal one, if the protocols obtained converge upon increasing S. We then proceed by carrying out a MC simulation starting from random initial protocols, without any assumption regarding the bang-bang nature of the protocol. In each step, we slightly change the control parameter g in a randomly chosen discretized time interval. If the cost function gets smaller, we accept the attempt; if the cost function gets larger, we accept the attempt with probability $\mathrm{e}^{-\Delta E/T_{MC}}$, where T_{MC} is a fictitious temperature that is gradually reduced to zero.

In Fig. 5·2(a), we show the optimal protocol obtained from such MC simulation

for a fixed instance of Hamiltonian (5.9) with $n = 5$ spins and total time $T = 0.8$.

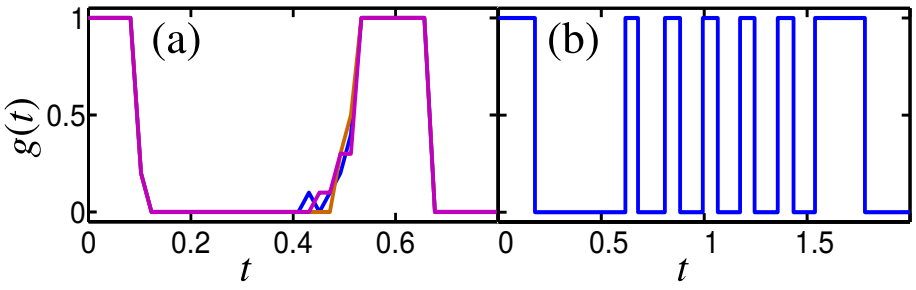

Figure 5·2: (a) The optimal protocol obtained from MC simulations for a fixed instance of Hamiltonian (5.9) with $n = 5$ spins and total annealing time $T = 0.8$. Different colors represent different initial protocols. The plots are for $S = 40$, but the optimal protocol does not change upon increasing S. (b) A typical protocol obtained for a given instance of Hamiltonian (5.9) with $n = 5$ spins and $T = 2$, using a classical optimization solver. We start from a uniform initial protocol with S slices such that $\delta t = T/S = 0.1$.

Indeed, the MC simulation converge to a bang-bang protocol for different initial protocols in agreement with the Pontryagin's minimum principle. Despite the convergence for short total time, the MC simulations often fail to converge for longer times and larger systems, signaling the difficulty of implementing VQA without any a priori knowledge about the form of the optimal protocol. However, based on the mathematical proof of the bang-bang nature of the optimal protocols, we can parameterize the protocol similar to QAOA [46] and use the durations of the pulses as variational parameters to be optimized with the interior-point minimization method (IPMM), increasing p to achieve convergence.

We have checked that IPMM results are indeed in agreement with MC results, e.g., Fig. 5·2(a) (it also runs much faster). In Fig.5·2(b), we show a typical optimized protocol obtained with IPMM for a certain instance of Hamiltonian (5.9) with $n = 5$ spins and $T = 2$. Guided by MC results, we choose around $\sim 20 \times T$ variational parameters, which proved to be adequate (we converged to a smaller number of bangs than we allowed in the ansatz).

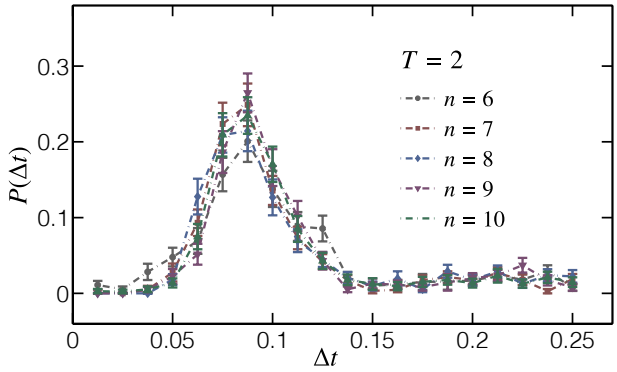

Figure 5·3: The average probability distribution of the time scales of bangs for different system sizes: $n = 6, 7, 8, 9$ and 10. The total annealing time is fixed to be $T = 2$, leading to an average success rate around $0.33 \sim 0.47$, depending on the system sizes. Each curve is averaged over 50 instances of Hamiltonian (5.9).

We now turn to the critical question of the time scales of the pulses. We observe numerically and then argue analytically that the typical time scale of each bang is independent of the system size, and is only determined by some characteristic energy scale of Hamiltonian (5.9). Therefore, from a complexity theory perspective, this result implies that the hardness of the optimization problem should translate into the number of pulses and/or the hardness of the protocol optimization. In Fig. 5·3 we plot the distribution of the time scales of each bang Δt for system sizes $n = 6, 7, 8, 9$ and 10. For each system size, we fix the total annealing time to be $T = 2$, and average over 50 instances of the Hamiltonian (5.9).

We find that the distributions for the bang time collapse for different system sizes, and peak at almost the same value. This observation suggests a universal average distribution of the bang times for the near optimal protocols, and a typical time scale (peak or average value) that is independent of the system size. Although we have only considered a few system sizes, the dependence on n is extremely weak and we expect our results to extrapolate to large n.

Finally we comment on the performance of our protocols. The cost function we

minimize is the expectation value $\langle\psi(T)|C|\psi(T)\rangle$. Minimizing the energy expectation value results in larger overlap with the ground state of C. As expected, the time scales for our protocols are significantly shorter than those of the adiabatic algorithm with similar success rate. A comparison between the optimal bang-bang protocols and linear ramps $g(t) = t/T$ is shown in Fig. 5·4. The errors in the final wavefunctions $1 - |\langle\psi_{GS}|\psi(T)\rangle|^2$ and final energies $E - E_{GS} \equiv \langle\psi(T)|C|\psi(T)\rangle - E_{GS}$ are averaged over the 20 instances (out of 50 generated realizations) with the highest success rates, for the optimal bang-bang protocol and linear QAA ramp respectively. We find that, in the system sizes considered in this work, the nonadiabatic bang-bang protocol with the same total time, performs better than the linear ramp (commonly used in QAA) in the ideal case, where the thermal environment and external noise are neglected. Of course, in practice one needs to include the overhead of searching for the optimal solution, and understand how it scales as function of system size. In particular, while implementing the bang-bang protocol consisting of square pulses on a quantum annealer is feasible [198], finding the optimal protocol with a classical optimizer could be difficult for certain hard instances of problems.

5.6 Effects of Dissipation and Dephasing

Real-world implementations of the bang-bang and QAA protocols are inevitably subject to noise either in the external controls or due to coupling to the thermal environment. Therefore, it is important to examine the effects of these perturbations on our optimal protocols for practical applications. Here we consider two noise models in order to evaluate the robustness of our bang-bang protocol, at the same time comparing it with the performance of QAA.

5.6.1 Random Dephasing Noise

Here we consider pure dephasing noise, where we introduce random fields in the x and z directions. This type of noise can capture noise induced by hardware electronics. Our error model can be viewed as the continuous time analog of the depolarizing channel commonly used for simulating noise in quantum circuits [3]. Since in a bang-bang protocol we either have $g(t) = 1$ or $g(t) = 0$ at any given time, we can write the stochastic Hamiltonian as

$$H(t) = C + \sum_{i=1}^{n} \delta h_i(t)\sigma_i^z + \sum_{i=1}^{n} \delta b_i(t)\sigma_i^x, \quad g = 1, \tag{5.12}$$

$$H(t) = B + \sum_{i=1}^{n} \delta h_i(t)\sigma_i^z + \sum_{i=1}^{n} \delta b_i(t)\sigma_i^x, \quad g = 0, \tag{5.13}$$

where $\delta h_i(t)$ and $\delta b_i(t)$ are noise in the z and x directions respectively, with strengths independent of the value of the coupling constants (additive noise). Assuming independent white noise for different terms with zero mean and second moments

$$\overline{\delta h_i(t)\delta h_{i'}(t')} = W_h^2 \delta_{ii'}\delta(t-t'), \tag{5.14}$$

$$\overline{\delta b_i(t)\delta b_{i'}(t')} = W_b^2 \delta_{ii'}\delta(t-t'), \tag{5.15}$$

the noise-averaged density matrix evolves with the following master equation [195]

$$\begin{aligned}\frac{d\rho(t)}{dt} = &- i[H,\rho(t)] - \frac{1}{2}W_h^2 \sum_{i=1}^{n}[[\rho(t),\sigma_i^z],\sigma_i^z] \\ &- \frac{1}{2}W_b^2 \sum_{i=1}^{n}[[\rho(t),\sigma_i^x],\sigma_i^x],\end{aligned} \tag{5.16}$$

where we take $W_b = W_h = W$ for simplicity. In the bang-bang case, the Hamiltonian H takes two different values $H = C$ ($H = B$) for $g = 1$ ($g = 0$), while in the QAA case, H has the explicit time dependence of Eq. (5.10) with $g(t) = t/T$.

In Fig. 5·4 we show the errors in the fidelity $1 - \langle\psi_{GS}|\rho(T)|\psi_{GS}\rangle$ and final energy

$\mathrm{Tr}\,[\rho(T)C] - E_{GS}$ for different strengths of noise. We find that in the small W regime, the noise only slightly decreases the fidelity, acting like a perturbation without inducing any instability. The effects of the noise on the linear QAA ramp are similar both qualitatively and quantitatively, changing the $W = 0$ error by amount of the same order of magnitude. For the strongest strength of noise that we studied ($W = 0.01$), the fidelity of the optimal bang-bang protocol remains higher than that of the linear ramp protocol.

A comment is in order regarding the dimension of W and the range used. As $\delta(t - t')$ has a dimension of time (inverse energy), W^2 has a dimension of energy. Strictly speaking, the δ function introduces infinitely large (albeit completely uncorrelated) random fields. This is unrealistic. In real experiments there is a characteristic high frequency, introducing a characteristic short time scale $\Delta\tau$, over which noise is correlated. This frequency scale is typically several orders of magnitude larger than the characteristic energy of the Hamiltonian (it diverges for the δ function). Therefore, Eq. (5.14) and (5.15) imply that $\delta h, \delta b \sim W/\sqrt{\Delta\tau}$, which means that for moderate noise in the random fields δh and δb, the corresponding values of W are suppressed by $\sqrt{\Delta\tau}$.

5.6.2 Weak Thermal Bath

Here we consider coupling the system to a weak thermal bath at temperature $1/\beta$. In this regime, the dynamics of the open system can be approximately described by the Redfield master equation which is commonly used to model noisy QAA for an actual annealing hardware [199–201]. Here we use the formulation in Ref. [199] and apply it to both QAA and bang-bang protocols.

The system of many qubits is coupled to the thermal bath via the Hamiltonian $\sum_i^n \sigma_i^z Q_i^z$, where Q_i^z are bath operators. We assume an Ohmic bosonic bath in thermal

equilibrium, with the spectral density function given by

$$S_i^z(\omega) = \int_{-\infty}^{\infty} dt\ e^{i\omega t}\ \langle Q_i^z(t) Q_i^z(0)\rangle = \eta\omega\ \frac{1}{1-e^{-\beta\omega}}\ , \tag{5.17}$$

where η is a dimensionless coefficient describing the strength of the coupling to the environment. We have taken the cut-off frequency of the bath to be infinite, so as to guarantee the Markovian assumption of dynamics. We employed Eqs.(4-9) in reference [199] to simulate the dynamics of open systems based on the Redfield master equation.

Fig. 5·5 shows the errors in the fidelity for different strengths of coupling to the bath, for both QAA and bang-bang protocols. Similar to the case of the closed system in the presence of white noise, we find that the errors corresponding to both protocols change in an analogous manner due to weak coupling to the environment in both the short- and long-time regimes. There is an intermediate time regime $8.5 \lesssim T \lesssim 11.5$, where QAA exhibits remarkable robustness and a much smaller change in $\eta = 0$ error. However, the errors of the VQA and QAA get closer as we increase T. Once again, the fidelity of the optimal bang-bang protocol remains higher than the QAA even for open system dynamics.

5.7 Pulse duration from the Pontryagin's minimum principle

Here we provide more details on how the Pontryagin's minimum principle can not only tell about the form of optimal solution for VQA but can also shed light on when the pulses should be switched on and off, in the context of the SK model.

Using the computational basis $z = z_1 \ldots z_n$, we represent the wave function as $|\psi(t)\rangle = \sum_z A_z(t)\,|z\rangle$. The initial state with all the spins in the x direction corre-

sponds to $A_z(0) = 1/\sqrt{2^n}$, and the Schrödinger equation reads

$$i\partial_t A_z(t) = g(t)C_z A_z(t) + [1 - g(t)] \sum_{k=1}^{n} A_{\bar{z}(k)}(t), \tag{5.18}$$

with $\bar{z}(k) = z_1 \ldots \bar{z}_k \ldots z_n$, where $\bar{z}_k$ represents a flipped spin with respect to z_k and C_z is the energy function we would like to minimize. In terms of the real and imaginary parts of $A_z(t) = R_z(t) + iI_z(t)$, we can then write

$$\partial_t R_z(t) = g(t)C_z I_z(t) + [1 - g(t)] \sum_{k=1}^{n} I_{\bar{z}(k)}(t), \tag{5.19}$$

$$\partial_t I_z(t) = -g(t)C_z R_z(t) - [1 - g(t)] \sum_{k=1}^{n} R_{\bar{z}(k)}(t). \tag{5.20}$$

Introducing conjugate momenta $P_z(t)$ and $Q_z(t)$ respectively for the real and imaginary parts of $A_z(t)$, the explicit form of the optimal-control Hamiltonian is given by

$$\begin{aligned} \mathcal{H} = \sum_z \Big\{ & g(t)C_z \left[P_z(t)I_z(t) - Q_z(t)R_z(t) \right] \\ & + [1 - g(t)] \sum_{k=1}^{n} \left[P_z(t)I_{\bar{z}(k)}(t) - Q_z(t)R_{\bar{z}(k)}(t) \right] \Big\}. \end{aligned} \tag{5.21}$$

The equations of motion for the conjugate momenta are $\partial_t P_z(t) = -\frac{\partial \mathcal{H}}{\partial R_z(t)}$ and $\partial_t Q_z(t) = -\frac{\partial \mathcal{H}}{\partial I_z(t)}$, which can be written explicitly as

$$\partial_t P_z(t) = g(t)C_z Q_z(t) + [1 - g(t)] \sum_{k=1}^{n} Q_{\bar{z}(k)}(t), \tag{5.22}$$

$$\partial_t Q_z(t) = -g(t)C_z P_z(t) - [1 - g(t)] \sum_{k=1}^{n} P_{\bar{z}(k)}(t), \tag{5.23}$$

where we have used the relationships $\sum_{z,k} Q_z(t)R_{\bar{z}(k)}(t) = \sum_{z,k} Q_{\bar{z}(k)}(t)R_z(t)$ and $\sum_{z,k} P_z(t)I_{\bar{z}(k)}(t) = \sum_{z,k} P_{\bar{z}(k)}(t)I_z(t)$.

The cost function

$$F[g(t)] = \sum_z |A_z(T)|^2 C_z \tag{5.24}$$

leads to the following boundary conditions at $t = T$ for the conjugate momenta:

$$P_z(T) = 2R_z(T)C_z, \quad Q_z(T) = 2I_z(T)C_z. \tag{5.25}$$

Notice that $g(t)$ uniquely determines $A_z(t)$. From $A_z(T)$ and the expression above, we can find $P_z(T)$ and $Q_z(T)$, solve the equations of motion backward in time and determine the conjugate momenta as a function of time. Therefore, $g(t)$ also uniquely determines $P_z(t)$ and $Q_z(t)$. The Potryagin's minimum principle states that the optimal protocol $g^*(t)$ satisfies

$$\mathcal{H}(g^*, \mathbf{R}^*, \mathbf{I}^*, \mathbf{P}^*, \mathbf{Q}^*) = \min_g \mathcal{H}(g, \mathbf{R}^*, \mathbf{I}^*, \mathbf{P}^*, \mathbf{Q}^*), \tag{5.26}$$

where $\mathbf{R}^*, \mathbf{I}^*, \mathbf{P}^*, \mathbf{Q}^*$ are the corresponding optimal solution. As argued in Sec. 5.3, $g^*(t)$ is bang-bang and can only take two values of 0 and 1. Which value will depend on the sign of $\frac{\partial \mathcal{H}}{\partial g}$ given by the expression

$$\begin{aligned} \frac{\partial \mathcal{H}}{\partial g} = \sum_z \Big\{ & C_z \left[P_z^*(t) I_z^*(t) - Q_z^*(t) R_z^*(t) \right] \\ & - \sum_{k=1}^{n} \left[P_z^*(t) I_{\tilde{z}(k)}^*(t) - Q_z^*(t) R_{\tilde{z}(k)}^*(t) \right] \Big\}. \end{aligned} \tag{5.27}$$

The sudden quenches at which $g(t)$ switches from 0 to 1 or vice versa correspond to the zeros of $\frac{\partial \mathcal{H}}{\partial g}$ above.

Let us first combine P_z and Q_z into one complex momentum

$$\Pi_z(t) = P_z(t) + iQ_z(t). \tag{5.28}$$

As we argued above, the optimal protocol is bang-bang with $g(t) = 0, 1$. In any

interval with $g(t) = 1$, we can write

$$A_z(t) = \mathrm{e}^{-iC_z(t-t_0)}A(t_0) \tag{5.29}$$

$$\Pi_z(t) = \mathrm{e}^{-iC_z(t-t_0)}\Pi(t_0), \tag{5.30}$$

where t_0 is the beginning of the current bang $g(t_0) = 1$. We first note that the term $P_z(t)I_z(t) - Q_z(t)R_z(t) = \mathrm{Im}\left[A_z(t)\Pi_z^*(t)\right]$ in Eq. (5.27) and does not change in intervals with $g(t) = 1$. Moreover the terms

$$\begin{aligned} &P_z(t)I_{\bar{z}(k)}(t) - Q_z(t)R_{\bar{z}(k)}(t) \\ &\quad = \mathrm{Im}\left[\mathrm{e}^{-i\left(C_z - C_{\bar{z}(k)}\right)(t-t_0)}A_z(t_0)\Pi_{\bar{z}(k)}^*(t_0)\right]. \end{aligned} \tag{5.31}$$

The above equation allows for an estimation of the typical time scale of the interval $g(t) = 1$. Suppose at some t_0, $g(t)$ switches from 0 to 1, i.e. a bang starts. From the discussion above, we know that at $t = t_0$ we must have $\frac{\partial \mathcal{H}}{\partial g}(t_0) = 0$. The time when the bang stops corresponds to the next $t > t_0$ when $\frac{\partial \mathcal{H}}{\partial g}(t) = 0$. More explicitly, in the interval $g(t) = 1$, Eq. (5.27) can be written as

$$w(t) = \sum_z \sum_{k=1}^{n} \mathrm{Im}\left[(\mathrm{e}^{-i(C_z - C_{\bar{z}(k)})(t-t_0)} - 1)A_z(t_0)\Pi_{\bar{z}(k)}^*(t_0)\right]. \tag{5.32}$$

We have $w(t_0) = 0$. The first root of the equation $w(t) = 0$ with $t > t_0$ then determines the duration of a pulse.

While we cannot derive analytically the average first root for $t > t_0$ from Eq. (5.32), one can see that the only time dependence in Eq. (5.32) within the current interval is in $\mathrm{e}^{-i(C_z - C_{\bar{z}(k)})t}$. Thus, the energy difference $\Delta C_{z,k} \equiv C_z - C_{\bar{z}(k)}$, which has zero mean (as both C_z and $C_{\bar{z}(k)}$ have zero mean) and variance $\overline{\Delta C_{z,k}^2} = 4(J^2 + h^2)$, sets the characteristic time scale proportional to $1/\sqrt{J^2 + h^2}$ observed in Fig. 5·3. Importantly, this time scale is finite and system-size independent, distinguishing our bang-bang type optimal protocol from the Trotterization of generic protocols, where

the duration of individual pulses must be taken to zero. We believe the numerically obtained system-size independent distribution of Fig. 5·3 follows from Eq. (5.32) whose root determines one set of the switching times for quenching $g(t)$ from 1 to 0, giving the duration of a pulse with $g(t) = 1$ [the distributions of pulse durations with $g(t) = 0$ and $g(t) = 1$ were found numerically to be almost identical]. However, an analytical derivation of the distribution in Fig. 5·3 has remained elusive.

5.8 Summary and Outlook

We have shown that the optimal VQA with bounded linear control parameters has a protocol of the bang-bang form. We verified this prediction by finding numerically the optimal protocol that minimizes the energy of a SK spin glass. The optimal nonadiabatic bang-bang protocols significantly reduce the error when compared to QAA within the same running time, and, at least for our system sizes, the advantage remains in the presence of weak additive white noise in the control parameters as well as weak coupling to a thermal environment.

Importantly, we show that the characteristic time scale between bangs is fixed by the energy scales in the problem and is independent of system size, which we confirm numerically. This finding significantly reduces the number of variational parameters in VQA, potentially decreasing the computational cost of the VQA outer-loop classical optimization algorithm to a great extent.

Our results, that the bang-bang protocols are optimal and the duration of each square pulse is size-independent, inform the search for effective hybrid classical-quantum schemes for solving combinatorial optimization problems. Further progress relies on the development of efficient outer-loop algorithms as well as hardware development for quantum enhanced optimization. Ultimately, the power of our results lies in their application to larger systems, for which solving the time-dependent

Schrodinger equation is impossible on a classical computer. Rapid developments in quantum technologies [202], together with the relative robustness of our protocols to specific models of external noise and thermal environment support the promise of such applications.

Acknowledgments

We are grateful to Ryan Babbush, Pedram Roushan, Eduardo Mucciolo, Dries Sels and Anatoli Polkovnikov for illuminating discussions. Z.-C. Y. would like to thank Quntao Zhuang for many early discussions on QAA.

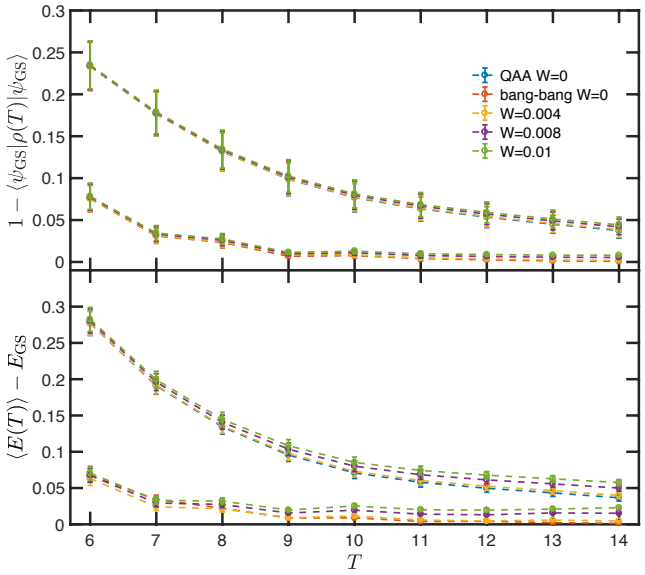

Figure 5·4: Errors in the fidelity (upper panel) and final energies (lower panel) evolved with the bang-bang and QAA protocols in the presence of noise with different strengths for $n = 5$.

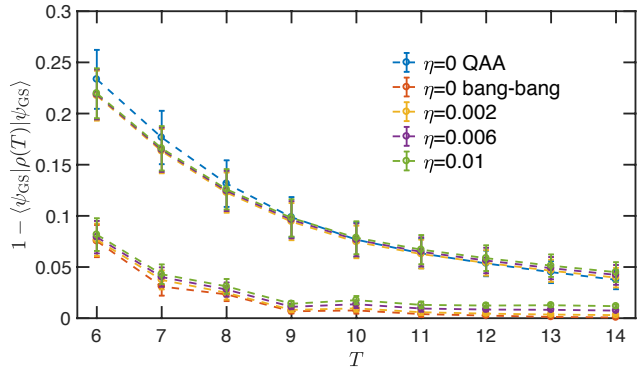

Figure 5·5: Errors in the fidelity of final states evolved with the bang-bang and QAA protocols in the presence of different strengths of coupling to the environment for $n = 5$. The inverse temperature is chosen to be $\beta = 2/J$.

Chapter 6

Hierarchical Majoranas in a programmable nanowire network

Abstract

We propose a hierarchical architecture for building "logical" Majorana zero modes using "physical" Majorana zero modes at the Y-junctions of a hexagonal network of semiconductor nanowires. Each Y-junction contains three "physical" Majoranas, which hybridize when placed in close proximity, yielding a single effective Majorana mode near zero energy. The hybridization of effective Majorana modes on neighboring Y-junctions is controlled by applied gate voltages on the links of the honeycomb network. This gives rise to a tunable tight-binding model of effective Majorana modes. We show that selecting the gate voltages that generate a Kekulé vortex pattern in the set of hybridization amplitudes yields an emergent "logical" Majorana zero mode bound to the vortex core. The position of a logical Majorana can be tuned adiabatically, *without* moving any of the "physical" Majoranas or closing any energy gaps, by programming the values of the gate voltages to change as functions of time. A nanowire network supporting multiple such "logical" Majorana zero modes provides a physical platform for performing adiabatic non-Abelian braiding operations in a fully controllable manner.

6.1 Introduction

Topological qubits offer stronger resistance to decoherence by storing quantum information non-locally. This property is a driving motivation behind theoretical studies of topological quantum computation. [54] Majorana zero modes (MZMs), for instance, make up half-a-qubit, thereby allowing the coding of qubits non-locally in two far-away Majoranas. There has been a number of experimental setups proposed to realize MZMs in condensed matter systems. [55, 203] One approach aims at engineering Hamiltonians with effective p-wave superconductivity by proximitizing an s-wave superconductor to a semiconductor nanowire with strong spin-orbit coupling, [204–210] or a topological insulator. [211–214] Such hybrid systems typically host MZMs at the endpoints or boundaries of the system. Recently, the theoretically predicted quantized zero-bias conductance peak at $2e^2/h$ in the presence of MZMs has been observed in indium antimonide semiconductor nanowires covered with an aluminium superconducting shell. [215]

Despite this progress, there remains the question of how to braid MZMs once they are realized experimentally. For example, many proposals for braiding MZMs involve processes by which energy gaps are selectively closed and reopened, thereby violating the adiabatic hypothesis. [216] In this work, we shall propose a scheme where braiding of MZMs can be implemented without violating the adiabatic hypothesis. The building blocks of our proposal are *Majorana nanowires*, i.e., semiconductor nanowires supporting Majorana modes bound to their endpoints at sufficiently low temperatures. However, the "logical" MZMs that are braided are *not* these elementary Majorana modes residing at the endpoints of the nanowires. Rather, they are emergent zero modes bound to point topological defects that can be programmed by gating the nanowires. These emergent zero modes live in two spatial dimensions, in contrast to 1D wires where the braiding statistics is intrinsically ill-defined. The

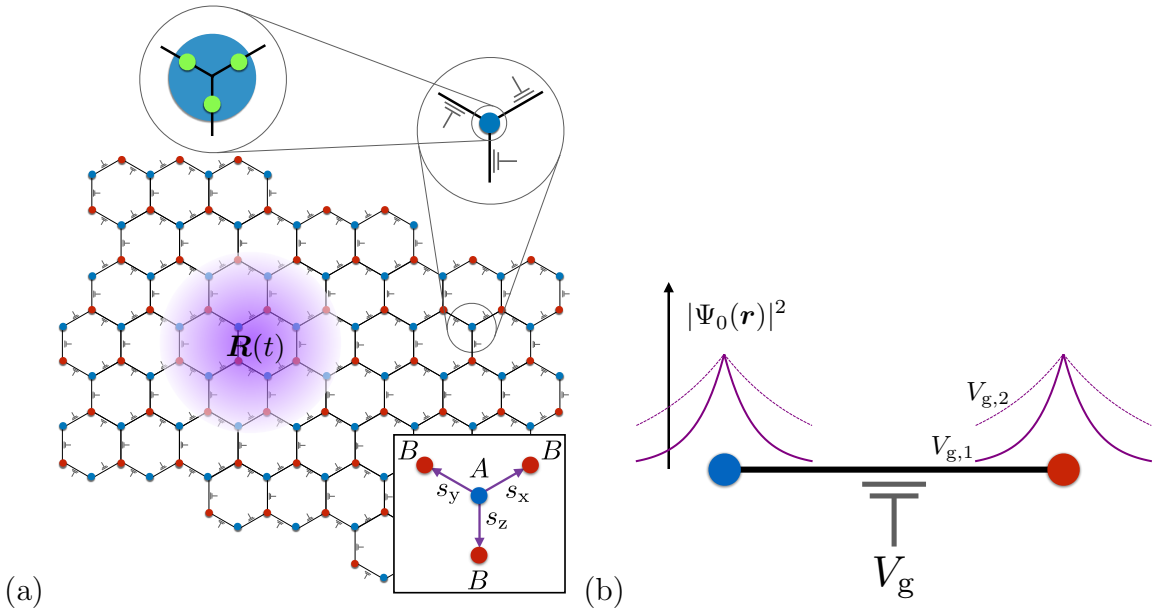

Figure 6·1: (a) Hierarchy of Majorana zero modes (MZMs). We start from an array of Majorana nanowires, depicted as the black links of a honeycomb lattice. Each nanowire furnishes three "physical" QMZMs (green circles in the inset) that hybridize locally, leaving one QMZM at each Y-junction (blue circle in the inset). The resulting effective QMZMs reside on the sites of a honeycomb lattice (blue and red circles). An array of gates (grey "plungers") provides tunable hybridization amplitudes for the effective QMZMs. Writing a particular pattern of gate voltages gives rise to a Kekulé vortex that binds an emergent "logical" MZM (purple density profile). The position $\boldsymbol{R}(t)$ of the emergent MZM is arbitrary and can be tuned continuously as a function of time, so that multiple "logical" MZMs can be braided adiabatically. Inset: Definition of the hexagonal lattice in terms of the two triangular sublattices Λ_A and Λ_B, with the nearest-neighbor vectors $\boldsymbol{s}_\alpha$, $\alpha = \mathtt{x}, \mathtt{y}, \mathtt{z}$. (b) Controlling the overlap between adjacent effective QMZMs with a gate voltage V_g. The Majorana wavefunctions (purple) decay exponentially across the length of the nanowire with a decay length that scales inversely with the topological nanowire gap Δ_{nw}. Increasing V_g from $V_{g,1}$ to $V_{g,2} > V_{g,1}$ decreases the nanowire gap, thereby increasing the wavefunction decay length, and with it the overlap between the two effective QMZMs (compare solid and dashed curves).

"logical" MZMs are *hierarchical*, in the sense that they emerge by coupling together a set of Majorana modes that are themselves the result of the topological state of

matter realized in each nanowire. The hierarchy of Majorana zero modes that are used in this work is depicted schematically in Fig. 6·1(a).

The hierarchical construction of the "logical" MZMs starts from a set of Majorana nanowires. Since each nanowire is of finite size, the Majorana modes at its endpoints hybridize weakly and split from zero energy. We call such a Majorana mode a quasi-Majorana zero mode (QMZM). Imagine placing one of the Majorana nanowires on each bond of a honeycomb lattice. At each vertex of the honeycomb lattice, where three nanowires form a Y-junction, three QMZMs hybridize strongly as their wavefunctions have large overlaps. This hybridization results in two QMZMs splitting away from zero energy by an amount much larger than the energy splitting of the QMZMs bound to the endpoints of a single nanowire, leaving a single effective QMZM at each site of the honeycomb lattice. This is the next level of the hierarchy. Now, imagine reducing the length of the Majorana nanowires making up the bonds of the honeycomb lattice. The increase of the overlap between these effective QMZMs will then be captured by a tight-binding model for Majorana modes hopping on the honeycomb lattice. If we assume translation invariant nearest-neighbor hopping amplitudes, there arises a gapped liquid with two massive Majorana cones very much as one finds in Kitaev's honeycomb model in the presence of a magnetic field, [217] or in other lattices in the presence of quartic Majorana interactions. [218]

Another gap, which allows for the formation and manipulation of "logical" MZMs, can then be opened by giving the hopping amplitudes a Kekulé pattern. In practice, this can be done by applying voltages on the individual Majorana nanowires, which modulates the hybridization of nearest-neighbor effective QMZMs. To see how, recall that the topological gap Δ_{nw} in a Majorana nanowire *decreases* when a gate voltage V_{g} is applied, thereby increasing the hybridization. [204–207] Decreasing the size of the topological gap *increases* the decay length of the QMZMs, thereby increasing the

overlap of their wavefunctions, see Fig. 6·1(b). Thus, by programming the set of gate voltages applied to every bond, one can exercise control over every hopping amplitude in the effective tight-binding model.

Furthermore, one can program these hopping amplitudes in a position-dependent manner so as to "write" an arbitrary number v of Kekulé vortices into the system. This is achieved by modulating the gate voltages as $V_{\mathrm{g}} \to V_{\mathrm{g}} + \delta V_{\mathrm{g}\boldsymbol{r},\alpha}$, where

$$\delta V_{\mathrm{g}\boldsymbol{r},\alpha} := V_0 \cos\left(\boldsymbol{K}_+ \cdot \boldsymbol{s}_\alpha + (\boldsymbol{K}_+ - \boldsymbol{K}_-) \cdot \boldsymbol{r} + \sum_{n=1}^{v} q_n \arg\left(\boldsymbol{r} - \boldsymbol{R}_n\right) \right). \tag{6.1}$$

Here, $\boldsymbol{r}$ is a point in one of the triangular sublattices of the honeycomb lattice, $\boldsymbol{s}_\alpha$ ($\alpha = \mathtt{x}, \mathtt{y}, \mathtt{z}$) are the nearest-neighbor vectors connecting to the other sublattice (see Fig. 6·1), $\boldsymbol{K}_+ = -\boldsymbol{K}_-$ are the corners of the Brillouin zone of the honeycomb lattice. The vorticities $q_n = \pm 1$ ($n = 1, \ldots, v$) and positions $\boldsymbol{R}_n$ are here merely parameters that can be tuned at will. Kekulé vortices have been shown to bind zero-energy modes in graphene, [219, 220] analogs of which also appear in photonic crystals. [221] Similar physics arises here, with the crucial distinction that the zero modes are now of Majorana nature, owing to the fact that the underlying tight-binding model is one of Majoranas. It is the MZMs localized near the core of each vortex that we shall call the "logical" MZMs, which constitute the final level of the hierarchy. Because the positions $\boldsymbol{R}_n$ of the vortices are merely parameters, they can be tuned simply by changing the voltages on each wire as a function of time, like addressing pixels on a screen. Therefore, in a system with multiple vortices, this scheme would allow one to move and braid the logical MZMs adiabatically.

The rest of the chapter is organized as follows. We present the realization with Majorana nanowires in Sec. 6.2 of an analogue of a $p+\mathrm{i}p$ superconductor belonging to the symmetry class D. We determine the conditions under which the Kekulé dimerization controls the gap. We define a scaling limit that allows one to derive a simple

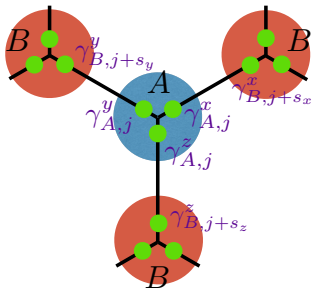

Figure 6·2: A Y-junction built from Majorana nanowires. The QMZMs are depicted as green dots. Effectively, there are three flavors of QMZMs on each lattice site. We label the operators creating QMZMs by $\hat{\gamma}^{\alpha}_{S,j}$, where $\alpha = \mathtt{x}, \mathtt{y}, \mathtt{z}$ denotes the bond to which the QMZM belongs, while $S = A, B$ denotes the sublattices, and j is the label for the lattice sites.

model of free Majoranas with nearest-neighbor hopping amplitudes on a honeycomb lattice in Sec. 6.3. In this scaling limit, the low-energy effective theory has higher symmetry, belonging to symmetry class BDI. We explicitly solve for the MZM bound to a Kekulé vortex. We further show that the Kekulé vortices indeed have the braiding statistics of MZMs. In Sec. 6.4, we demonstrate numerically the emergence of an MZM bound to the core of a Kekulé vortex away from the scaling limit. Section 6.5 discusses possible experimental measurement schemes for the emergent MZMs and demonstrates the feasibility of our setup using realistic experimental parameters. We conclude with a summary and outlook for future directions in Sec. 6.6.

6.2 Realization with Majorana nanowires

The building block that we shall use in this work is a nanowire which at low temperatures supports a topological superconducting gap Δ_{nw}. Because of the topological gap Δ_{nw}, the nanowire hosts a pair of QMZMs at its endpoints when superconducting. We shall call such a nanowire a "Majorana nanowire."

The main idea of this work is to imagine that each nearest-neighbor bond of the

honeycomb lattice is realized by a Majorana nanowire. There are two energy scales in the problem: a hybridization U and a hopping amplitude t, as we now explain.

On the one hand, three Majorana nanowires must meet at the sites of the honeycomb lattice, thereby realizing a Y-junction of Majorana nanowires, as shown in Fig. 6·2. Effectively (i.e., below the energy gap Δ_{nw} of an isolated Majorana nanowire), we have three flavors of QMZMs on each site of the honeycomb lattice. The pairwise hybridization among the three QMZMs will split their quasidegeneracy by an energy scale $|U|$. Then, only one QMZM remains below the energy scale $|U|$ on any given Y-junction (site of the honeycomb lattice). Thus, each Y-junction effectively contributes a single emergent Majorana mode.

On the other hand, the pair of QMZMs bound to the two ends of a Majorana nanowire are split away from zero energy by the energy scale t that results from the overlap of their wavefunctions. This hybridization increases as each Majorana nanowire is shortened, inducing a nearest-neighbor hopping amplitude t for the three pairs of QMZMs localized on nearest-neighbor Y-junctions of Majorana nanowires.

Hence, working at energies below the topological gap Δ_{nw} of a Majorana nanowire, we have outlined the construction of an effective six-band tight-binding model on the honeycomb lattice using Majorana nanowires. Below we shall discuss this construction in more detail.

6.2.1 Trimer limit ($U \neq 0$, $t = 0$)

Consider a honeycomb lattice Λ made of two interpenetrating triangular lattices Λ_A and Λ_B. We shall label the bonds of the honeycomb lattice by $\alpha = \mathtt{x}, \mathtt{y}, \mathtt{z}$ depending on their orientations, as shown in Fig. 6·2. Each bond of the honeycomb lattice realizes a Majorana nanowire. We shall thus associate to each bond of the honeycomb lattice a pair of Majorana operators as depicted in Fig. 6·2. If the label $S = A, B$ distinguishes between the triangular sublattices Λ_A and Λ_B, and if the label j stands for a site from

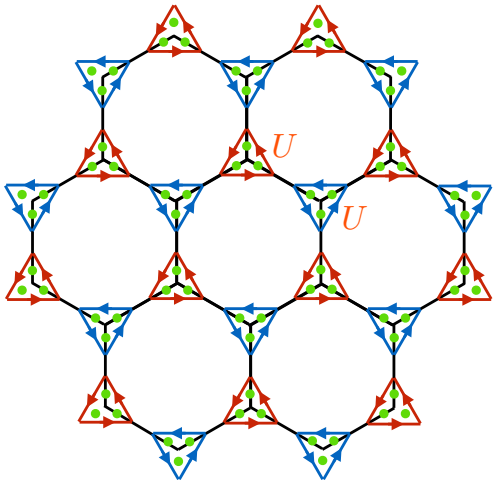

Figure 6·3: Representation of the trimer limit defined by the ground state of Hamiltonian (6.3). The MZMs at each Y-junction are represented by green dots. Their pairwise hybridization U is represented by directed bonds arranged along the edges of a triangle. The blue and red triangles encircles sites from sublattices Λ_A and Λ_B, respectively. The hybridization energy scale for blue and red triangles is U. The pattern of arrows along the edges of each triangle defines the order in which two Majorana operators are to be multiplied with the convention that U is positive for this order of multiplication.

Λ_S, then the Majorana algebra reads

$$\left\{\hat{\gamma}^{\alpha}_{S,j}, \hat{\gamma}^{\alpha'}_{S',j'}\right\} = 2\delta_{\alpha,\alpha'}\delta_{S,S'}\delta_{j,j'} \tag{6.2a}$$

with the Majorana reality condition

$$\hat{\gamma}^{\alpha\dagger}_{S,j} = \hat{\gamma}^{\alpha}_{S,j}. \tag{6.2b}$$

These Majorana operators stand at the first level of the hierarchy.

The trimer limit occurs for $t = 0$. The Hamiltonian describing this limit is

$$\widehat{H}_{\text{trimer}} := \sum_{S=A,B}\sum_{j\in\Lambda_S} \mathrm{i}U\left(\hat{\gamma}^{\mathtt{x}}_{S,j}\,\hat{\gamma}^{\mathtt{y}}_{S,j} + \hat{\gamma}^{\mathtt{y}}_{S,j}\,\hat{\gamma}^{\mathtt{z}}_{S,j} + \hat{\gamma}^{\mathtt{z}}_{S,j}\,\hat{\gamma}^{\mathtt{x}}_{S,j}\right). \tag{6.3}$$

We represent in Fig. 6·3 the trimer limit as a decorated honeycomb lattice. Hybridization within each Y-junction is represented by a directed arrow relating a pair of MZMs. The direction of the arrows along the edges of each triangle defines the order in which two Majorana operators are to be multiplied. It fixes the sign of the hybridization U to be positive along the arrow. Reversing the chirality of the red or blue triangles thus amounts to reversing the sign of U.

Hamiltonian (6.3) is the sum over $S = A, B$ and $j \in \Lambda_S$ of the pairwise commuting operators

$$\mathrm{i}U \left(\hat{\gamma}^{\mathtt{x}}_{S,j} \, \hat{\gamma}^{\mathtt{y}}_{S,j} + \hat{\gamma}^{\mathtt{y}}_{S,j} \, \hat{\gamma}^{\mathtt{z}}_{S,j} + \hat{\gamma}^{\mathtt{z}}_{S,j} \, \hat{\gamma}^{\mathtt{x}}_{S,j} \right) . \tag{6.4a}$$

As each one of these operators has the three single-particle eigenvalues

$$-\sqrt{3}\,U, \qquad 0, \qquad +\sqrt{3}\,U, \tag{6.4b}$$

with the Majorana zero mode

$$\hat{\eta} \coloneqq \frac{1}{\sqrt{3}} \left(\hat{\gamma}^{\mathtt{x}}_{S,j} + \hat{\gamma}^{\mathtt{y}}_{S,j} + \hat{\gamma}^{\mathtt{z}}_{S,j} \right) , \tag{6.4c}$$

Hamiltonian (6.3) supports three doubly-degenerate flat bands with the single-particle energies (6.4b), respectively.

6.2.2 Dimer limit ($t \neq 0$, $U = 0$)

The dimer limit occurs for $U = 0$. The Hamiltonian describing this limit is

$$\widehat{H}_{\text{dimer}} \coloneqq \sum_{j \in \Lambda_A} \sum_{\alpha = \mathtt{x},\mathtt{y},\mathtt{z}} \mathrm{i}t \, \hat{\gamma}^{\alpha}_{A,j} \, \hat{\gamma}^{\alpha}_{B,j+\boldsymbol{s}_\alpha} . \tag{6.5a}$$

Here, $\boldsymbol{s}_\alpha$ are the unit vectors connecting the three sites in Λ_B that are nearest-neighbor to a site in Λ_A, i.e.,

$$\boldsymbol{s}_{\mathtt{z}} \coloneqq \begin{pmatrix} 0 \\ -1 \end{pmatrix} , \quad \boldsymbol{s}_{\mathtt{x}} \coloneqq \begin{pmatrix} +\sqrt{3}/2 \\ 1/2 \end{pmatrix} , \quad \boldsymbol{s}_{\mathtt{y}} \coloneqq \begin{pmatrix} -\sqrt{3}/2 \\ 1/2 \end{pmatrix} . \tag{6.5b}$$

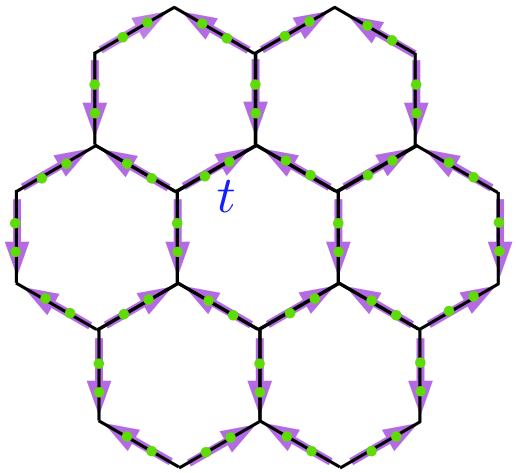

Figure 6·4: Representation of the dimer limit defined by the ground state of Hamiltonian (6.5a). The arrows specify the order in which Majorana operators (the green dots) enter Hamiltonian (6.5a), with the convention that operators on sublattice Λ_A are to the left of operators from sublattice Λ_B along an arrow. With this convention, the hopping amplitude t is positive along an arrow.

One may represent this Hamiltonian as is done in Fig. 6·4. The energy scale t results from the finite lengths of Majorana nanowires, which allows the pair of wavefunctions of the QMZMs bound to the two ends of the semiconductor nanowire to have a nonvanishing overlap. This overlap leads to a splitting of their energies away from 0 by the amount $\pm|t|$.

Hamiltonian (6.5a) is the sum over $j \in \Lambda_A$ and $\alpha = \mathtt{x}, \mathtt{y}, \mathtt{z}$ of the pairwise commuting operators

$$\mathrm{i}t\, \hat{\gamma}^{\alpha}_{A,j}\, \hat{\gamma}^{\alpha}_{B,j+\boldsymbol{s}_\alpha}. \tag{6.6a}$$

As each one of these operators has the two single-particle eigenvalues

$$-|t|, \qquad +|t| \tag{6.6b}$$

Hamiltonian (6.5a) supports two triply-degenerate flat bands with the single-particle

energies (6.6b), respectively. The single-particle energies (6.6b) correspond to the fermionic state

$$\hat{c}_j^{\alpha\dagger}|0\rangle := \frac{1}{2}\left(\hat{\gamma}_{A,j}^{\alpha} - \mathrm{i}\,\hat{\gamma}_{B,j+\boldsymbol{s}_\alpha}^{\alpha}\right)|0\rangle, \qquad \hat{c}_j^{\alpha}|0\rangle := 0, \tag{6.7}$$

being empty or occupied, respectively. There is no zero mode in the dimer limit.

6.2.3 Reversal of time

We shall define the action of time reversal by the rules

$$\mathrm{i} \mapsto -\mathrm{i}, \qquad \hat{\gamma}_{A,j}^{\alpha} \mapsto +\hat{\gamma}_{A,j}^{\alpha}, \qquad \hat{\gamma}_{B,j+\boldsymbol{s}_\alpha}^{\alpha} \mapsto -\hat{\gamma}_{B,j+\boldsymbol{s}_\alpha}^{\alpha}. \tag{6.8}$$

The motivation for this definition is that we would like to interpret

$$\hat{c}_{A,j}^{\alpha} := \frac{1}{2}\left(\hat{\gamma}_{A,j}^{\alpha} + \mathrm{i}\,\hat{\gamma}_{B,j+\boldsymbol{s}_\alpha}^{\alpha}\right) \tag{6.9}$$

as a fermion operator localized on the directed bond $\langle j \in \Lambda_A, j + \boldsymbol{s}_\alpha \in \Lambda_B\rangle$ of the honeycomb lattices that is left invariant by the operation of time reversal.

One verifies that Hamiltonian (6.5a) is even under reversal of time while Hamiltonian (6.3) is odd under reversal of time, i.e.,

$$\widehat{H}_{\text{dimer}} \mapsto +\widehat{H}_{\text{dimer}}, \qquad \widehat{H}_{\text{trimer}} \mapsto -\widehat{H}_{\text{trimer}}. \tag{6.10}$$

Although $\widehat{H}_{\text{trimer}}$ is odd under time reversal, the zero-energy flat band transforms trivially whereas the finite-energy bands are interchanged.

6.2.4 Hamiltonian for the nanowire network

When both $U \neq 0$ and $t \neq 0$, we can write the noninteracting Hamiltonian in momentum space as

$$\widehat{H}_{\text{wire}} := \widehat{H}_{\text{trimer}} + \widehat{H}_{\text{dimer}} = \int\limits_{\Omega_{\text{BZ}}^{\text{K}}} \mathrm{d}^3\boldsymbol{k}\, \widehat{\Psi}_{\boldsymbol{k}}^{\dagger}\, \mathcal{H}_{\text{wire}}\, \widehat{\Psi}_{\boldsymbol{k}}, \tag{6.11a}$$

with the spinor

$$\widehat{\Psi}_{\boldsymbol{k}}^{\dagger} = \begin{pmatrix} \hat{\gamma}_{A,\boldsymbol{k}}^{\mathrm{x}} & \hat{\gamma}_{A,\boldsymbol{k}}^{\mathrm{y}} & \hat{\gamma}_{A,\boldsymbol{k}}^{\mathrm{z}} & \hat{\gamma}_{B,\boldsymbol{k}}^{\mathrm{x}} & \hat{\gamma}_{B,\boldsymbol{k}}^{\mathrm{y}} & \hat{\gamma}_{B,\boldsymbol{k}}^{\mathrm{z}} \end{pmatrix} \tag{6.11b}$$

and the single-particle Hamiltonian

$$\mathcal{H}_{\text{wire}} = \begin{pmatrix} 0 & +\mathrm{i}U/2 & -\mathrm{i}U/2 & +\frac{\mathrm{i}t}{2}\, e^{\mathrm{i}\boldsymbol{k}\cdot\boldsymbol{s}_{\mathrm{x}}} & 0 & 0 \\ -\mathrm{i}U/2 & 0 & +\mathrm{i}U/2 & 0 & +\frac{\mathrm{i}t}{2}\, e^{\mathrm{i}\boldsymbol{k}\cdot\boldsymbol{s}_{\mathrm{y}}} & 0 \\ +\mathrm{i}U/2 & -\mathrm{i}U/2 & 0 & 0 & 0 & +\frac{\mathrm{i}t}{2}\, e^{\mathrm{i}\boldsymbol{k}\cdot\boldsymbol{s}_{\mathrm{z}}} \\ -\frac{\mathrm{i}t}{2}\, e^{-\mathrm{i}\boldsymbol{k}\cdot\boldsymbol{s}_{\mathrm{x}}} & 0 & 0 & 0 & +\mathrm{i}U/2 & -\mathrm{i}U/2 \\ 0 & -\frac{\mathrm{i}t}{2}\, e^{-\mathrm{i}\boldsymbol{k}\cdot\boldsymbol{s}_{\mathrm{y}}} & 0 & -\mathrm{i}U/2 & 0 & +\mathrm{i}U/2 \\ 0 & 0 & -\frac{\mathrm{i}t}{2}\, e^{-\mathrm{i}\boldsymbol{k}\cdot\boldsymbol{s}_{\mathrm{z}}} & +\mathrm{i}U/2 & -\mathrm{i}U/2 & 0 \end{pmatrix}. \tag{6.11c}$$

The single-particle Hamiltonian (6.11c) is of Bogoliubov-de Gennes (BdG) form. This is to say that out of its six Majorana bands, three have positive single-particle energies, three have negative single single-particle energies, and there exists an antiunitary transformation such that the six bands can be organized into three pairs such that for any one of these three pairs the Majorana band with positive single-particle energy maps to the Majorana band with negative single-particle energy and vice versa under the antiunitary transformation.

When $|U/t| \ll 1$, the two flat bands of $\widehat{H}_{\text{dimer}}$ acquire a dispersion with a bandwidth that is controlled by $|U|$. Both bands are topologially trivial. We will not consider this limit anymore in this chapter.

When $|t/U| \ll 1$, the zero-energy modes (6.4c) of $\widehat{H}_{\text{trimer}}$ that are localized on the sites of the honeycomb lattice get hybridized by $\widehat{H}_{\text{dimer}}$. More precisely, the twofold

degenerate flat band in the Brillouin zone Ω_{BZ} arising from the zero mode $\hat{\eta}$ defined in Eq. (6.4c) when $t/U = 0$ turns into two bands related by particle-hole symmetry. The bandwidth for this pair of Majorana bands is of order $|t|$. These emergent low-energy Majorana modes realize the second level of the hierarchy of Majoranas. The limit $|U| \gg |t|$ enforces the first hierarchical reduction in the number of effective Majorana modes. We now turn to a quantitative analysis of the band structure of the Hamiltonian (6.11c) in this limit.

In Fig. 6·5, we plot the band structure for $t/U = 0.1$ with $U > t > 0$. We find that a gap opens at the corners of the Brillouin zone. We shall call this gap the Haldane gap. This terminology will be explained when we introduce the single-particle Hamiltonian (6.19) and show that it opens a spectral gap and endows Majorana bands with non-vanishing Chern numbers. A direct calculation of the eigenvalues at $\boldsymbol{K}_{\pm}$ shows that the energies of the two bands at $\boldsymbol{K}_{\pm}$ are given by

$$\begin{aligned}\varepsilon_{\pm}(\boldsymbol{K}_{+}) &= \varepsilon_{\pm}(\boldsymbol{K}_{-}) \\ &= \pm\,\frac{1}{4}\left(\sqrt{3}\,U - \sqrt{3U^2 + 4t^2}\right) \\ &\approx \pm\,\frac{t^2}{2\sqrt{3}\,U} + \mathcal{O}\left(\frac{t^4}{U^3}\right). \end{aligned} \tag{6.12}$$

We thus find that the Haldane gap is of order t^2/U and, as such, can be explained within second-order perturbation theory. Upon linearization of the single-particle Hamiltonian in the vicinity of $\boldsymbol{K}_{\pm}$, this gap can be interpreted as a Haldane mass that implements the microscopic breaking of time-reversal symmetry. [222]. The counterpart of this phase in the Kitaev's honeycomb model is the non-Abelian topologically ordered phase stabilized by a magnetic field. [217]

When the system is perturbed by a Kekulé dimerization defined by

$$\delta\widehat{H}_{\mathrm{dimer}} \coloneqq \mathrm{i}\sum_{j\in\Lambda_A}\sum_{\alpha=\mathtt{x},\mathtt{y},\mathtt{z}} \delta t_{j,\alpha}\,\hat{\gamma}^{\alpha}_{A,j}\,\hat{\gamma}^{\alpha}_{B,j+\boldsymbol{s}_\alpha} \tag{6.13a}$$

with the dimerization pattern [223]

$$\delta t_{j,\alpha} := \Delta\, e^{\mathrm{i}\boldsymbol{K}_+\cdot\boldsymbol{s}_\alpha}\, e^{\mathrm{i}\boldsymbol{G}\cdot\boldsymbol{r}_j} + \text{c.c.}, \tag{6.13b}$$

where the Kekulé amplitude

$$\Delta := \Delta_0\, e^{\mathrm{i}\varphi}, \qquad \Delta_0 := |\Delta|, \qquad \varphi \in [0, 2\pi), \tag{6.13c}$$

and

$$\boldsymbol{G} := \boldsymbol{K}_+ - \boldsymbol{K}_- \equiv 2\boldsymbol{K}_+ \equiv -2\boldsymbol{K}_- \tag{6.13d}$$

is the momentum connecting the two valleys, such that $0 < \Delta_0 \ll t^2/U$, the band gap decreases until it vanishes when $\Delta_0 \sim t^2/U$. When the Kekulé amplitude $\Delta_0 \gtrsim t^2/U$, the gap is of Kekulé character [219]. This case is illustrated in Fig. 6·6. We stress that the Haldane and Kekulé gaps compete against each other, so they realize two distinct gapped phases separated by a gap-closing transition. [224]

6.2.5 Scaling limits

There is an interesting scaling limit of (6.11) consisting in taking the limit $U \to \infty$ holding t fixed. In this limit, the hierarchy

$$U > t > \frac{t}{U}\, t \tag{6.14a}$$

becomes

$$\infty > t > 0. \tag{6.14b}$$

This limit sends to infinite energy the two pairs of particle-hole symmetric Majorana bands that are separated by an energy of order $2U$ [see Eqs. (6.4)]. It leaves a *gapless* pair of particle-hole symmetric Majorana bands with conical band crossing at the corners $\boldsymbol{K}_+$ and $\boldsymbol{K}_-$ of the Brillouin zone Ω_{BZ}. In this limit, time-reversal symmetry,

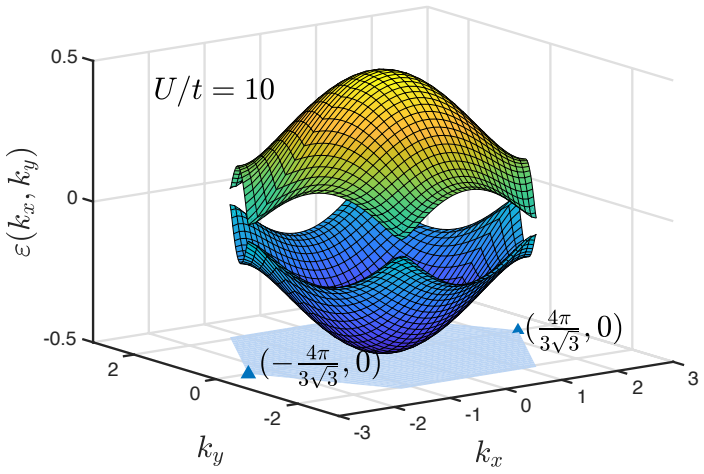

Figure 6·5: The pair of particle-hole symmetric bands with the lowest energies for Hamiltonian (6.11a) when $U/t = 10$ with $U > t > 0$. A Haldane gap appears at the corners of the Brillouin zone Ω_{BZ} (depicted in light blue). The magnitude of the Haldane gap follows from $\varepsilon_{\pm}(\boldsymbol{K}_{+}) = \varepsilon_{\pm}(\boldsymbol{K}_{-}) \approx \pm\frac{t^2}{2\sqrt{3}\,U} + \mathcal{O}(t^4/U^3)$. The energies are plotted in units of t.

as measured by the vanishing of the Haldane gap, is restored. This limit is useful as it allows one to treat in closed analytical form the effect of a Kekulé modulation of t – in particular the effect of a vortex in the Kekulé modulation of t – on the single-particle spectrum.

6.3 Free Majoranas on a honeycomb lattice with Kekulé dimerization

We start by reviewing the properties of a tight-binding model for Majoranas hopping on the honeycomb lattice with nearest-neighbor hopping amplitudes. This model is motivated by the scaling limit $U \to \infty$ holding t fixed that turns the hierarchy (6.14a) into the hierarchy (6.14b).

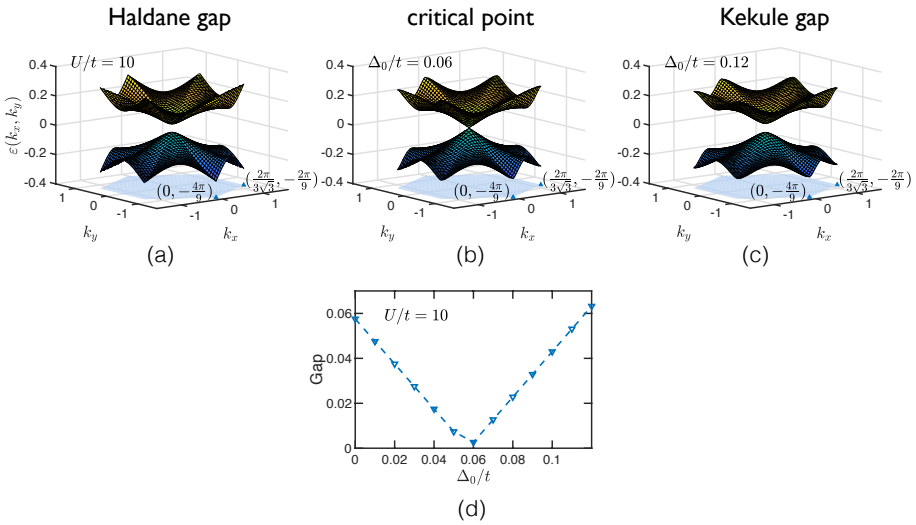

Figure 6·6: Upper panels: the pair of particle-hole symmetric bands with the lowest energies for Hamiltonian (6.11a) when $U/t = 10$ with $U > t > 0$ in the reduced Brillouin zone $\Omega_{\rm BZ}^{\rm K}$ (depicted in light blue). The energies are plotted in units of t. (a) Haldane gap at the corners of the original Brillouin zone $\Omega_{\rm BZ}$ in the absence of Kekulé dimerization is folded to the Γ point of $\Omega_{\rm BZ}^{\rm K}$. (b) The critical point where the gap closes when $\Delta_0/t \approx 0.06$. (c) A Kekulé gap is present at the Γ point in the reduced Brillouin zone for $\Delta_0/t = 0.12$. Lower panel: (d) the single-particle spectral gap as a function of Δ_0/t. Upon increasing Δ_0/t, the gap first closes and then reopens, indicating a phase transition separating two distinct gapped phases in which either the Haldane gap or the Kekulé gap dominates.

6.3.1 Gapless liquid phase with uniform hopping amplitudes

Consider a honeycomb lattice Λ made of two interpenetrating triangular lattices Λ_A and Λ_B. We start with the operator $\hat{a}_{\boldsymbol{r}}$ that either creates or annihilates a Majorana mode on the lattice site $\boldsymbol{r}$, i.e.,

$$\{\hat{a}_{\boldsymbol{r}}, \hat{a}_{\boldsymbol{r}'}\} = 2\delta_{\boldsymbol{r},\boldsymbol{r}'}, \qquad \hat{a}_{\boldsymbol{r}}^\dagger = \hat{a}_{\boldsymbol{r}}, \tag{6.15a}$$

for any pair of sites $\boldsymbol{r}$ and $\boldsymbol{r}'$. We endow these Majorana modes with the quantum dynamics specified by the single-particle Hamiltonian

$$\widehat{H} \coloneqq \sum_{\boldsymbol{r}\in\Lambda_A} \sum_{\alpha=\mathtt{x},\mathtt{y},\mathtt{z}} t\,\mathrm{i}\hat{a}_{\boldsymbol{r}}\,\hat{a}_{\boldsymbol{r}+\boldsymbol{s}_\alpha}. \tag{6.15b}$$

Without loss of generality, we choose the hopping amplitudes to be positive, $t > 0$. We have set the lattice spacing $\mathfrak{a}$ of the honeycomb lattice to unity, $\mathfrak{a} = 1$.

We observe that Majorana operators localized on sublattice Λ_A always appear to the left of Majorana operators localized on sublattice Λ_B in the Hamiltonian (6.15b). If we define the operation of time reversal by the rule

$$\mathrm{i} \mapsto -\mathrm{i}, \qquad \hat{a}_{\boldsymbol{r}} \mapsto +\hat{a}_{\boldsymbol{r}}, \qquad \hat{a}_{\boldsymbol{r}+\boldsymbol{s}_\alpha} \mapsto -\hat{a}_{\boldsymbol{r}+\boldsymbol{s}_\alpha}, \tag{6.16}$$

we conclude that the Hamiltonian (6.15b) is invariant under reversal of time.

Hamiltonian (6.15b) is invariant under the translations that map the honeycomb lattice onto itself. Hence, we perform the Fourier transformation

$$\hat{a}_{\boldsymbol{r}} =: \frac{1}{\sqrt{N}} \sum_{\boldsymbol{k}\in\Omega_{\mathrm{BZ}}} e^{\mathrm{i}\boldsymbol{k}\cdot\boldsymbol{r}} \hat{a}_{A,\boldsymbol{k}}, \tag{6.17a}$$

$$\hat{a}_{\boldsymbol{r}+\boldsymbol{s}_\alpha} =: \frac{1}{\sqrt{N}} \sum_{\boldsymbol{k}\in\Omega_{\mathrm{BZ}}} e^{\mathrm{i}\boldsymbol{k}\cdot(\boldsymbol{r}+\boldsymbol{s}_\alpha)} \hat{a}_{B,\boldsymbol{k}}, \tag{6.17b}$$

where Ω_{BZ} denotes the Brillouin zone of the triangular sublattice. Notice that since $\hat{a}_{\boldsymbol{r}}$ is a Majorana operator, $\hat{a}^\dagger_{\boldsymbol{k}}$ and $\hat{a}_{\boldsymbol{k}}$ are not independent,

$$\hat{a}^\dagger_{A,\boldsymbol{k}} = \hat{a}_{A,-\boldsymbol{k}}, \qquad \hat{a}^\dagger_{B,\boldsymbol{k}} = \hat{a}_{B,-\boldsymbol{k}}. \tag{6.17c}$$

If we introduce the two-component spinor

$$\hat{\gamma}^\dagger_{\boldsymbol{k}} \coloneqq \begin{pmatrix} \hat{a}^\dagger_{A,\boldsymbol{k}} & \hat{a}^\dagger_{B,\boldsymbol{k}} \end{pmatrix}, \tag{6.18a}$$

Hamiltonian (6.15b) turns into

$$\widehat{H} = \sum_{\boldsymbol{k}\in\Omega_{\mathrm{BZ}}} \hat{\gamma}^{\dagger}_{\boldsymbol{k}}\, \mathrm{i}\mathcal{A}_{\boldsymbol{k}}\, \hat{\gamma}_{\boldsymbol{k}}, \tag{6.18b}$$

where

$$\begin{aligned} \mathcal{H}_{\boldsymbol{k}} &\equiv \mathrm{i}\mathcal{A}_{\boldsymbol{k}} \\ &\coloneqq \frac{\mathrm{i}}{2} \begin{pmatrix} 0 & +t \sum\limits_{\alpha=\mathrm{x,y,z}} e^{-\mathrm{i}\boldsymbol{k}\cdot\boldsymbol{s}_\alpha} \\ -t \sum\limits_{\alpha=\mathrm{x,y,z}} e^{+\mathrm{i}\boldsymbol{k}\cdot\boldsymbol{s}_\alpha} & 0 \end{pmatrix}. \end{aligned} \tag{6.18c}$$

We observe that the symmetry under reversal of time defined by Eq. (6.16) is broken by adding to the single-particle Hamiltonian (6.18c) the traceless diagonal matrix

$$\mathcal{H}^{\mathrm{Hal}}_{\boldsymbol{k}} \coloneqq \begin{pmatrix} +\Delta^{\mathrm{Hal}}_{\boldsymbol{k}} & 0 \\ 0 & -\Delta^{\mathrm{Hal}}_{\boldsymbol{k}} \end{pmatrix}, \tag{6.19a}$$

where we demand that the so-called Haldane amplitude satisfies

$$\Delta^{\mathrm{Hal}}_{-\boldsymbol{k}} = -\Delta^{\mathrm{Hal}}_{+\boldsymbol{k}} \tag{6.19b}$$

for any $\boldsymbol{k}$ in the Brillouin zone Ω_{BZ}.

Solving for

$$\sum_{\alpha=\mathrm{x,y,z}} e^{+\mathrm{i}\boldsymbol{k}\cdot\boldsymbol{s}_\alpha} = 0 \tag{6.20a}$$

yields the two nodal points

$$\boldsymbol{K}_{\pm} \coloneqq \frac{4\pi}{3\sqrt{3}} \begin{pmatrix} \pm 1 \\ 0 \end{pmatrix} \tag{6.20b}$$

at the corners $\boldsymbol{K}_{\pm}$ of the Brillouin zone. Hence, the single-particle spectrum of the single-particle Hamiltonian (6.18c) is identical to that of graphene for spinless fermions at vanishing chemical potential by virtue of the Majorana representation in the second-quantized Hamiltonian (6.18b).

Adding the Haldane term (6.19) to the single-particle Hamiltonian (6.18c) opens

a gap $2|\Delta_{\boldsymbol{K}_+}| > 0$, the so-called Haldane gap, at the corners $\boldsymbol{K}_\pm$ of the Brillouin zone. The upper and lower bands carry opposite Chern numbers of magnitude 1 when $2|\Delta_{\boldsymbol{K}_+}| > 0$. This Haldane gap is the counterpart to the gap (6.12).

If we focus on the low-energy physics near the two Majorana cones, we can write $\boldsymbol{k} = \boldsymbol{K}_\pm + \boldsymbol{p}$ in the vicinity of $\boldsymbol{K}_\pm$ and expand to leading order in $\boldsymbol{p}$. The linearized Hamiltonian (6.15b) now takes the form

$$\widehat{H} \approx \frac{1}{2} \int\limits_{\Omega_{\mathrm{BZ}}} \frac{\mathrm{d}^2\boldsymbol{p}}{(2\pi)^2}\, \widehat{\Upsilon}^\dagger(\boldsymbol{p})\, \mathrm{i}\widetilde{\mathcal{A}}(\boldsymbol{p})\, \widehat{\Upsilon}(\boldsymbol{p}), \tag{6.21a}$$

$$\widetilde{\mathcal{H}}(\boldsymbol{p}) \equiv \mathrm{i}\widetilde{\mathcal{A}}(\boldsymbol{p}) = v_{\mathrm{F}} \begin{pmatrix} -\boldsymbol{p}\cdot\boldsymbol{\sigma} & 0 \\ 0 & +\boldsymbol{p}\cdot\boldsymbol{\sigma} \end{pmatrix}, \tag{6.21b}$$

where $v_{\mathrm{F}} := 3t/2$ and $\boldsymbol{\sigma}$ are Pauli matrices acting on the two sublattice degrees of freedom. We have introduced the four-component spinor

$$\widehat{\Upsilon}^\dagger(\boldsymbol{p}) = \begin{pmatrix} \hat{a}^\dagger_{A,+}(\boldsymbol{p}) & -\mathrm{i}\hat{a}^\dagger_{B,+}(\boldsymbol{p}) & -\mathrm{i}\hat{a}^\dagger_{B,-}(\boldsymbol{p}) & \hat{a}^\dagger_{A,-}(\boldsymbol{p}) \end{pmatrix}, \tag{6.21c}$$

where the subscript $\pm$ labels the two valleys centered about the nodal points (6.20b). If we introduce another set of Pauli matrices $\boldsymbol{\tau}$ acting on these valley degrees of freedom, the constraint from the reality condition becomes

$$\widehat{\Upsilon}^\dagger(\boldsymbol{p}) = [-\sigma^2 \otimes \tau^2 \widehat{\Upsilon}(-\boldsymbol{p})]^{\mathsf{T}}. \tag{6.21d}$$

If we do the rescaling

$$\widehat{\Upsilon}^\dagger(\boldsymbol{p}) =: \sqrt{2}\, \widehat{\Psi}^\dagger(\boldsymbol{p}), \qquad \widehat{\Upsilon}\,(\boldsymbol{p}) =: \sqrt{2}\, \widehat{\Psi}\,(\boldsymbol{p}), \tag{6.22a}$$

one may verify that the components of $\widehat{\Psi}^\dagger(\boldsymbol{p})$ obey the standard algebra of *complex* fermions in momentum space within each valley subspace. Finally, we arrive at the

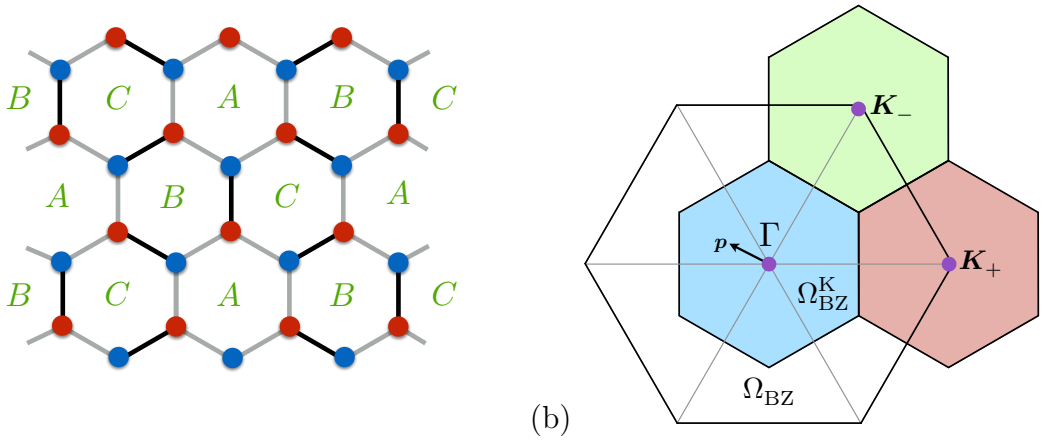

Figure 6·7: (a) The Kekulé modulation of the coupling strengths along the bonds. The black (grey) color denotes hopping amplitudes that are strong (weak). Such a dimerization pattern breaks the space group symmetry of the original Bravais lattice by enlarging the original unit cell. We label the inequivalent plaquettes by A, B, and C, and the enlarged unit cell is made of three original unit cells. (b) Folding the Brillouin zone $\Omega_{\rm BZ}$ of the honeycomb lattice into the Kekulé Brillouin zone $\Omega_{\rm BZ}^{\rm K}$. The three colored Brillouin zones are equivalent up to translation by reciprocal lattice vectors of the folded Brillouin zone.

representation

$$\widehat{H} \approx \int \frac{\mathrm{d}^2\boldsymbol{p}}{(2\pi)^2}\, \widehat{\Psi}^\dagger(\boldsymbol{p})\, \widetilde{\mathcal{H}}(\boldsymbol{p}) \widehat{\Psi}(\boldsymbol{p}), \tag{6.22b}$$

$$\widetilde{\mathcal{H}}(\boldsymbol{p}) \equiv -v_{\rm F}\, \boldsymbol{p}\cdot\boldsymbol{\sigma} \otimes \tau^3, \tag{6.22c}$$

$$\widehat{\Psi}^\dagger(\boldsymbol{p}) = [-\sigma^2 \otimes \tau^2 \widehat{\Psi}(-\boldsymbol{p})]^{\mathsf{T}}. \tag{6.22d}$$

This is the same Hamiltonian as the one governing the vortex-free sector of Kitaev's honeycomb model. [217] The spinors $\widehat{\Psi}(\boldsymbol{p})$ and $\widehat{\Psi}^\dagger(\boldsymbol{p})$ are not independent due to the constraint (6.22d), which is essentially a particle-hole constraint that relates the operators at one valley to the other valley. Therefore, the single-particle Hamiltonian (6.22c) has a BdG form.

6.3.2 Gapped phase with Kekulé dimerization

We consider the effect of a Kekulé modulation of the hopping amplitudes along the bonds of the honeycomb lattice. As we will see, the Kekulé dimerization will open a gap near $\boldsymbol{K}_{\pm}$. The Hamiltonian describing the Kekulé modulation can be represented by [compare with Eq. (6.13)]

$$\delta\widehat{H} \coloneqq \mathrm{i} \sum_{\boldsymbol{r}\in\Lambda_A} \sum_{\alpha=\mathrm{x},\mathrm{y},\mathrm{z}} \delta t_{\boldsymbol{r},\alpha}\, \hat{a}_{\boldsymbol{r}}\, \hat{a}_{\boldsymbol{r}+\boldsymbol{s}_\alpha} \tag{6.23a}$$

with the dimerization pattern [223]

$$\delta t_{\boldsymbol{r},\alpha} \coloneqq \frac{\Delta}{3}\, e^{\mathrm{i}\boldsymbol{K}_+\cdot\boldsymbol{s}_\alpha}\, e^{\mathrm{i}\boldsymbol{G}\cdot\boldsymbol{r}} + \text{c.c.}, \tag{6.23b}$$

where the Kekulé amplitude

$$\Delta \coloneqq \Delta_0\, e^{\mathrm{i}\varphi}, \qquad \Delta_0 \coloneqq |\Delta|, \qquad \varphi \in [0, 2\pi), \tag{6.23c}$$

will be shown to be associated to a single-particle gap that opens up at the nodal points (6.20b). The Kekulé term (6.23b) modulates the magnitudes of the hopping amplitudes along the bonds in an alternating fashion as shown in Fig. 6·7(a). Such a dimerization pattern breaks the space group symmetry of the original Bravais lattice by enlarging the original unit cell. In Fig. 6·7(a), we label the inequivalent plaquettes by A, B, and C. By inspection of Fig. 6·7(a), one observes that the enlarged unit cell is made of three original ones. As a result, we now have a smaller Brillouin zone $\Omega_{\mathrm{BZ}}^{\mathrm{K}}$ corresponding to the enlarged unit cell, see Fig. 6·7(b). There are $3 \times 2 = 6$ Majorana bands with all momenta from the original Brillouin zone Ω_{BZ} folded into $\Omega_{\mathrm{BZ}}^{\mathrm{K}}$. Applying the Fourier transformation (6.17), the Kekulé modulation (6.23) takes

the form

$$\delta\widehat{H} = \mathrm{i}\sum_{\boldsymbol{k}\in\Omega_{\mathrm{BZ}}}\left[\left(\sum_{\alpha=\mathrm{x,y,z}}\frac{2\Delta}{3}\,e^{\mathrm{i}(\boldsymbol{K}_+ +\boldsymbol{k})\cdot\boldsymbol{s}_\alpha}\right)\hat{a}^\dagger_{A,[\boldsymbol{k}+\boldsymbol{G}]}\,\hat{a}_{B,[\boldsymbol{k}]} + \left(\sum_{\alpha=\mathrm{x,y,z}}\frac{2\overline{\Delta}}{3}\,e^{\mathrm{i}(\boldsymbol{K}_- +\boldsymbol{k})\cdot\boldsymbol{s}_\alpha}\right)\hat{a}^\dagger_{A,[\boldsymbol{k}-\boldsymbol{G}]}\,\hat{a}_{B,[\boldsymbol{k}]}\right], \tag{6.24}$$

where we have used the reality condition (6.17c) and defined $[\boldsymbol{q}]$ as the wave vector in the union of the three colored hexagonal cells in Fig. 6·7(b) that differs from $\boldsymbol{q}$ by a reciprocal wave vector. Expanding Eq. (6.24) near $\boldsymbol{K}_\pm$ and the Γ point, we obtain

$$\begin{aligned}\delta\widehat{H} = \mathrm{i}\Bigg[&\sum_{\boldsymbol{p}\in\Omega^{\mathrm{K}}_{\mathrm{BZ}}}\left(\sum_{\alpha=\mathrm{x,y,z}}\frac{2\Delta}{3}\,e^{\mathrm{i}(2\boldsymbol{K}_+ +\boldsymbol{p})\cdot\boldsymbol{s}_\alpha}\right)\hat{a}^\dagger_{A,[3\boldsymbol{K}_+ +\boldsymbol{p}]}\,\hat{a}_{B,[\boldsymbol{K}_+ +\boldsymbol{p}]}\\ &+\sum_{\boldsymbol{p}\in\Omega^{\mathrm{K}}_{\mathrm{BZ}}}\left(\sum_{\alpha=\mathrm{x,y,z}}\frac{2\overline{\Delta}}{3}\,e^{\mathrm{i}\boldsymbol{p}\cdot\boldsymbol{s}_\alpha}\right)\hat{a}^\dagger_{A,[\boldsymbol{K}_- +\boldsymbol{p}]}\,\hat{a}_{B,[\boldsymbol{K}_+ +\boldsymbol{p}]}\\ &+\sum_{\boldsymbol{p}\in\Omega^{\mathrm{K}}_{\mathrm{BZ}}}\left(\sum_{\alpha=\mathrm{x,y,z}}\frac{2\Delta}{3}\,e^{\mathrm{i}\boldsymbol{p}\cdot\boldsymbol{s}_\alpha}\right)\hat{a}^\dagger_{A,[\boldsymbol{K}_+ +\boldsymbol{p}]}\,\hat{a}_{B,[\boldsymbol{K}_- +\boldsymbol{p}]}\\ &+\sum_{\boldsymbol{p}\in\Omega^{\mathrm{K}}_{\mathrm{BZ}}}\left(\sum_{\alpha=\mathrm{x,y,z}}\frac{2\overline{\Delta}}{3}\,e^{\mathrm{i}(2\boldsymbol{K}_- +\boldsymbol{p})\cdot\boldsymbol{s}_\alpha}\right)\hat{a}^\dagger_{A,[3\boldsymbol{K}_- +\boldsymbol{p}]}\,\hat{a}_{B,[\boldsymbol{K}_- +\boldsymbol{p}]}\\ &+\sum_{\boldsymbol{p}\in\Omega^{\mathrm{K}}_{\mathrm{BZ}}}\left(\sum_{\alpha=\mathrm{x,y,z}}\frac{2\Delta}{3}\,e^{\mathrm{i}(\boldsymbol{K}_+ +\boldsymbol{p})\cdot\boldsymbol{s}_\alpha}\right)\hat{a}^\dagger_{A,[\boldsymbol{K}_- +\boldsymbol{p}]}\,\hat{a}_{B,[\boldsymbol{p}]}\\ &+\sum_{\boldsymbol{p}\in\Omega^{\mathrm{K}}_{\mathrm{BZ}}}\left(\sum_{\alpha=\mathrm{x,y,z}}\frac{2\overline{\Delta}}{3}\,e^{\mathrm{i}(\boldsymbol{K}_- +\boldsymbol{p})\cdot\boldsymbol{s}_\alpha}\right)\hat{a}^\dagger_{A,[\boldsymbol{K}_+ +\boldsymbol{p}]}\,\hat{a}_{B,[\boldsymbol{p}]}\Bigg].\end{aligned} \tag{6.25}$$

The modes at the Γ point must also be taken into account, since the expansion near $\boldsymbol{K}_\pm$ already involves $3\boldsymbol{K}_\pm$, which can be identified as the Γ point. However, the hybridization between the nodal modes and the modes at the Γ point occurs at much higher energies. In the low energy physics, we may neglect terms involving the modes at the Γ point in Eq. (6.25) and keep only hybridized modes between the nodal points

$[\boldsymbol{K}_{\pm}]$. To leading order in $\boldsymbol{p}$, we thus obtain

$$\delta\widehat{H} \approx \mathrm{i}\int \frac{\mathrm{d}^2\boldsymbol{p}}{(2\pi)^2}\Big\{ \Big[\Delta\,\hat{a}^{\dagger}_{A,+}(\boldsymbol{p})\,\hat{a}_{B,-}(\boldsymbol{p}) + \overline{\Delta}\,\hat{a}^{\dagger}_{A,-}(\boldsymbol{p})\,\hat{a}_{B,+}(\boldsymbol{p})\Big] - \Big[\Delta\,\hat{a}^{\dagger}_{B,+}(\boldsymbol{p})\,\hat{a}_{A,-}(\boldsymbol{p}) + \overline{\Delta}\,\hat{a}^{\dagger}_{B,-}(\boldsymbol{p})\,\hat{a}_{A,+}(\boldsymbol{p})\Big] \Big\} \tag{6.26a}$$

where we have made the identifications

$$\hat{a}^{\dagger}_{S,[\boldsymbol{K}_{+}+\boldsymbol{p}]} \to \hat{a}^{\dagger}_{S,+}(\boldsymbol{p}), \qquad \hat{a}^{\dagger}_{S,[\boldsymbol{K}_{-}+\boldsymbol{p}]} \to \hat{a}^{\dagger}_{S,-}(\boldsymbol{p}), \qquad S = A, B. \tag{6.26b}$$

Combining with Eq. (6.22b), the low-energy effective Hamiltonian in the presence of a Kekulé modulation can be written in the continuum as

$$\widehat{H}_{\mathrm{Kek}} \coloneqq \widehat{H} + \delta\widehat{H} \equiv \int \frac{\mathrm{d}^2\boldsymbol{p}}{(2\pi)^2}\,\widehat{\Psi}^{\dagger}(\boldsymbol{p})\,\widetilde{\mathcal{H}}_{\mathrm{Kek}}(\boldsymbol{p})\widehat{\Psi}(\boldsymbol{p}), \tag{6.27a}$$

where

$$\widetilde{\mathcal{H}}_{\mathrm{Kek}}(\boldsymbol{p}) \coloneqq \begin{pmatrix} -\boldsymbol{p}\cdot\boldsymbol{\sigma} & \Delta\,\sigma^0 \\ \overline{\Delta}\,\sigma^0 & +\boldsymbol{p}\cdot\boldsymbol{\sigma} \end{pmatrix}, \tag{6.27b}$$

and we have set $v_{\mathrm{F}} = 1$. We remark that the particle-hole symmetry was never broken on the way to Eq. (6.27), so that the single-particle Hamiltonian (6.27b) is still of the BdG type. As advertised, the Kekulé dimerization opens a gap $2|\Delta|$ in the single-particle spectrum due to scattering with the amplitude Δ between the two nodal points.

6.3.3 Symmetry class

We now consider the symmetries of the BdG Hamiltonian (6.27). We shall drop the tilde and denote $\widetilde{\mathcal{H}}(\boldsymbol{p})$ simply as $\mathcal{H}(\boldsymbol{p})$ from now on.

First, the reality condition (6.21d) imposes the spectral particle-hole symmetry

$$\mathcal{C}\,\widetilde{\mathcal{H}}_{\mathrm{Kek}}(\boldsymbol{p})\,\mathcal{C}^{-1} = -\widetilde{\mathcal{H}}^{*}_{\mathrm{Kek}}(-\boldsymbol{p}), \qquad \mathcal{C} \coloneqq -\sigma^{2}\otimes\tau^{2}\,\mathsf{K}, \tag{6.28}$$

where K denotes complex conjugation. Hamiltonian (6.27) also possesses the time-reversal symmetry

$$\mathcal{T}\,\widetilde{\mathcal{H}}_{\mathrm{Kek}}(\boldsymbol{p})\,\mathcal{T}^{-1} = \widetilde{\mathcal{H}}^{*}_{\mathrm{Kek}}(-\boldsymbol{p}), \qquad \mathcal{T} \coloneqq \sigma^{1}\otimes\tau^{1}\,\mathsf{K}. \tag{6.29}$$

Finally, composition of $\mathcal{C}$ and $\mathcal{T}$ yields the chiral symmetry

$$\mathcal{S} \coloneqq \mathcal{T}\,\mathcal{C} = \sigma^{3}\otimes\tau^{3}, \tag{6.30}$$

under which

$$\hat{a}_{A} \mapsto \hat{a}_{A}, \qquad \hat{a}_{B} \mapsto -\hat{a}_{B}, \tag{6.31}$$

and

$$\mathcal{S}\,\widetilde{\mathcal{H}}_{\mathrm{Kek}}(\boldsymbol{p})\,\mathcal{S}^{-1} = -\widetilde{\mathcal{H}}_{\mathrm{Kek}}(\boldsymbol{p}). \tag{6.32}$$

Notice that the symmetry transformation satisfies

$$\mathcal{C}^{2} = 1, \qquad \mathcal{T}^{2} = 1, \tag{6.33}$$

so that Hamiltonian (6.27) belongs to the symmetry class BDI. In the presence of point topological defects (vortices), the Hamiltonian supports zero-energy chiral Majorana modes classified by $\mathbb{Z}$. [225–228] As we will see explicitly in the next section, zero modes with positive and negative chiral eigenvalues have nonvanishing amplitudes on sublattice Λ_{A} and Λ_{B}, respectively.

6.3.4 Chiral Majorana zero modes bound to Kekulé vortices

The Kekulé distortion enters (6.27) as a complex-valued amplitude. As such the Kekulé distortion supports point-like static defects in the form of vortices

$$\Delta_{\mathrm{vtx}}(\boldsymbol{r}) \coloneqq \Delta_0(\boldsymbol{r}) e^{\mathrm{i}(\varphi + n\theta)}, \qquad \boldsymbol{r} = |\boldsymbol{r}| \begin{pmatrix} \cos\theta \\ \sin\theta \end{pmatrix}, \tag{6.34a}$$

where $n \in \mathbb{Z}$ is the vorticity that measures the winding of the phase of the Kekulé order parameter, while $\Delta_0(\boldsymbol{r}) \coloneqq |\Delta_{\mathrm{vtx}}(\boldsymbol{r})|$ defines the profile of its magnitude. This static function must vanish at the origin and saturate to some prescribed nonvanishing but finite value as $\boldsymbol{r} \to \infty$, say

$$\Delta_0(\boldsymbol{r}) \coloneqq \Delta_0 \tanh\left(\frac{|\boldsymbol{r}|}{\ell_0}\right) \tag{6.34b}$$

with $\Delta_0 > 0$ and $\ell_0 > 0$.

We seek any qualitative change induced in the single-particle spectrum of Hamiltonian (6.27b) when the Kekulé order parameter is given by Eq. (6.34) instead of being a constant complex number. To this end, we represent Hamiltonian (6.27) in two-dimensional position space. We thus have

$$\widetilde{\mathcal{H}}_{\mathrm{Kek}}(\boldsymbol{r}) \coloneqq \begin{pmatrix} 0 & 2\mathrm{i}\partial_z & \Delta_{\mathrm{vtx}}(\boldsymbol{r}) & 0 \\ 2\mathrm{i}\partial_{\bar{z}} & 0 & 0 & \Delta_{\mathrm{vtx}}(\boldsymbol{r}) \\ \overline{\Delta}_{\mathrm{vtx}}(\boldsymbol{r}) & 0 & 0 & -2\mathrm{i}\partial_z \\ 0 & \overline{\Delta}_{\mathrm{vtx}}(\boldsymbol{r}) & -2\mathrm{i}\partial_{\bar{z}} & 0 \end{pmatrix}, \tag{6.35a}$$

where we have chosen the basis

$$\widehat{\Psi}^\dagger(\boldsymbol{r}) \coloneqq \frac{1}{\sqrt{2}} \begin{pmatrix} \hat{a}^\dagger_{A,+}(\boldsymbol{r}) & -\mathrm{i}\hat{a}^\dagger_{B,+}(\boldsymbol{r}) & -\mathrm{i}\hat{a}^\dagger_{B,-}(\boldsymbol{r}) & \hat{a}^\dagger_{A,-}(\boldsymbol{r}) \end{pmatrix} \tag{6.35b}$$

obeying the reality condition

$$\widehat{\Psi}^\dagger(\boldsymbol{r}) \coloneqq \left[-\sigma^2 \otimes \tau^2 \widehat{\Psi}(\boldsymbol{r})\right]^{\mathsf{T}} \tag{6.35c}$$

and used the complex coordinates

$$\begin{aligned} z &\coloneqq x + \mathrm{i}y, \qquad \partial_z = \tfrac{1}{2}\left(\partial_x - \mathrm{i}\partial_y\right), \\ \bar{z} &\coloneqq x - \mathrm{i}y, \qquad \partial_{\bar{z}} \coloneqq \tfrac{1}{2}\left(\partial_x + \mathrm{i}\partial_y\right). \end{aligned} \tag{6.35d}$$

We seek normalizable solutions to the eigenvalue problem

$$\mathcal{H}_{\mathrm{Kek}}(\boldsymbol{r})\,\Psi_0(\boldsymbol{r}) = 0. \tag{6.36}$$

If a normalizable solution $\Psi_0(\boldsymbol{r})$ exists, we shall call it a zero mode. This problem was first studied by Jackiw and Rossi in a different context where $\Delta(\boldsymbol{r})$ is the vortex in the superconducting order parameter. [226] Here, the origin of the gap is instead the bond density wave due to the Kekulé modulation. [219] Nevertheless, the mathematical structure of the Hamiltonian (6.35) is identical to that studied by Jackiw and Rossi. As a consequence of the spectral chiral symmetry (6.30), the single-particle Hamiltonian (6.35) is block off diagonal. Hence, any zero-mode solution must take one of two forms, namely

$$\Psi_{A,0}(\boldsymbol{r}) = \begin{pmatrix} u_A(\boldsymbol{r}) \\ 0 \\ 0 \\ v_A(\boldsymbol{r}) \end{pmatrix}, \qquad \Psi_{B,0}(\boldsymbol{r}) = \begin{pmatrix} 0 \\ u_B(\boldsymbol{r}) \\ v_B(\boldsymbol{r}) \\ 0 \end{pmatrix}. \tag{6.37}$$

As is implied by the notation, $\Psi_{S,0}(\boldsymbol{r})$ has support on sublattice $S = A, B$ only. For simplicity, we shall focus below only on cases where $|n| = 1$.

When $n = -1$, only $\Psi_{A,0}(\boldsymbol{r})$ is normalizable. It is given by

$$u_A(\boldsymbol{r}) = \mathcal{N}\, e^{\mathrm{i}\left(\frac{\pi}{4}+\frac{\varphi}{2}\right)}\, e^{-\int_0^r \mathrm{d}r'\,\Delta_0(r')}, \tag{6.38a}$$

$$u_B(\boldsymbol{r}) = 0, \tag{6.38b}$$

$$v_B(\boldsymbol{r}) = 0, \tag{6.38c}$$

$$v_A(\boldsymbol{r}) = \overline{u_B(\boldsymbol{r})}, \tag{6.38d}$$

where $\mathcal{N}$ is the normalization constant. The wavefunction (6.38) is exponentially localized about the vortex core, for it decays exponentially fast with the distance $\boldsymbol{r}$ away from the vortex core with the characteristic decay length $\sim 1/\Delta_0$ set by the asymptotic magnitude Δ_0 of the Kekulé order parameter. There follows the "logical" MZM operator

$$\hat{\gamma}_A \coloneqq \int \mathrm{d}^2\boldsymbol{r} \, \left[u_A(\boldsymbol{r}) \, \hat{a}_{A,+}(\boldsymbol{r}) + \overline{u_A(\boldsymbol{r})} \, \hat{a}_{A,-}(\boldsymbol{r}) \right]. \tag{6.38e}$$

The reality condition

$$\gamma_A^\dagger = \gamma_A \tag{6.38f}$$

follows from Eq. (6.35c).

Similarly, when $n = +1$, it is only $\Psi_{B,0}(\boldsymbol{r})$ that is normalizable. The wavefunction is then given by

$$u_A(\boldsymbol{r}) = 0, \tag{6.39a}$$

$$u_B(\boldsymbol{r}) = \mathcal{N} \, e^{\mathrm{i}(\frac{\pi}{4} + \frac{\varphi}{2})} \, e^{-\int_0^r \mathrm{d}r' \, \Delta_0(r')}, \tag{6.39b}$$

$$v_B(\boldsymbol{r}) = \overline{u_A(\boldsymbol{r})}, \tag{6.39c}$$

$$v_A(\boldsymbol{r}) = 0, \tag{6.39d}$$

where $\mathcal{N}$ is the normalization constant. There follows the "logical" MZM operator

$$\hat{\gamma}_B \coloneqq \int \mathrm{d}^2\boldsymbol{r} \, \left[u_B(\boldsymbol{r}) \, \hat{a}_{B,+}(\boldsymbol{r}) + \overline{u_B(\boldsymbol{r})} \, \hat{a}_{B,-}(\boldsymbol{r}) \right]. \tag{6.39e}$$

The reality condition

$$\hat{\gamma}_B^\dagger = \hat{\gamma}_B \tag{6.39f}$$

follows from Eq. (6.35c).

In summary, far-separated Kekulé vortices with $|n| = 1$ bind MZMs localized

around their vortex cores, with nonvanishing amplitude on either sublattice Λ_A or Λ_B, respectively. For $|n| > 1$, the index theorem guarantees that there are $|n|$ mutually orthogonal normalizable zero modes, with support on sublattice Λ_A or Λ_B depending on $\mathrm{sgn}(n)$. [226] All n zero modes are robust to any perturbation that respects the BDI symmetry. [225–228] Thus, in general, Kekulé vortices in class BDI can harbor multiple protected MZMs, unlike vortices in the traditional (2+1)-dimensional $p+\mathrm{i}\,p$ superconductor. [148, 150] The reason for this is that vortices in the latter case carry a $\mathbb{Z}_2$ index, owing to the fact that the parent Hamiltonian is in class D rather than BDI, so that only the parity of the number of MZMs is conserved. The model studied in Sec. 6.2 turns out to be in class D, and consequently is more similar to the usual $p+\mathrm{i}\,p$ superconductor, despite the fact that its vortices also stem from the presence of a Kekulé distortion.

If we drop the reality condition (6.35c), the fermion number becomes a good quantum number. This situtation applies to the case of complex fermions hopping on the honeycomb lattice as was considered in Refs. [219, 220]. The filled Fermi sea with the zero mode occupied or empty, respectively, can then be assigned the fermion number $\pm 1/2$. In the presence of the reality condition (6.35c), the zero mode becomes a logical MZM of indefinite fermion number. The logical MZMs obey an exotic braiding statistics, as we now explain.

6.3.5 Braiding statistics of Kekulé vortices

In this section, we review the fact that the form of the zero-mode solutions (6.38e) and (6.39e) implies that their corresponding MZM operators obey non-Abelian braiding statistics, just like the half-vortices of $p+\mathrm{i}p$ topological superconductors. [148, 150]

Instead of one vortex, we shall consider v vortices all sharing the same vorticity centered at the positions $\boldsymbol{R}_1, \cdots, \boldsymbol{R}_v$ on the two-dimensional Euclidean plane through

the Ansatz

$$\Delta(\boldsymbol{r};\boldsymbol{R}_1,\cdots,\boldsymbol{R}_v) \coloneqq \Delta_0 \prod_{j=1}^{v} \tanh\left(\frac{|\boldsymbol{r}-\boldsymbol{R}_j|}{l_0}\right) \times e^{\mathrm{i}[\varphi_j - \arg(\boldsymbol{r}-\boldsymbol{R}_j)]}. \tag{6.40}$$

We assume that the vortices are kept far enough away from each other that their pairwise hybridization can be ignored, i.e.,

$$|\boldsymbol{R}_i - \boldsymbol{R}_j| \gg 1/\Delta_0 \tag{6.41}$$

must always hold for any $1 \leq i < j \leq v$. Suppose that $\boldsymbol{R}_j$ moves adiabatically anti-clockwise once along a closed path in two-dimensional Euclidean space. Furthermore, suppose that this path encircles one and only one vortex, say the vortex located at $\boldsymbol{R}_i$ without loss of generality. If $\boldsymbol{r}$ is sufficiently close to $\boldsymbol{R}_i$, $\arg(\boldsymbol{r}-\boldsymbol{R}_j)$ changes by 2π, a change that can be absorbed by taking $\varphi_i \to \varphi_i + 2\pi$. However, due to the presence of the phase $\varphi_i/2$ in the zero mode solutions (6.38) and (6.39), we find that $\hat{\gamma}_i \to -\hat{\gamma}_i$ after moving $\boldsymbol{r}_j$ a full circle around $\boldsymbol{r}_i$. Repeating the same analysis by interchanging the role of $\boldsymbol{r}_j$ and $\boldsymbol{r}_i$, one finds that $\hat{\gamma}_j \to -\hat{\gamma}_j$ as well.

The appearance of the additional minus sign due to the multi-valuedness of the zero mode solutions parallels that of the $p + \mathrm{i}\, p$ topological superconductor. Namely, the MZM operator changes sign as the vortex phase winds by 2π. To keep track of the signs, it is convenient to take $\varphi_i \in [0, 2\pi)$ and introduce branch cuts so that φ_i jumps by 2π each time the vortex $\boldsymbol{r}_i$ crosses a branch cut. In this way, one can derive the following property of the Majorana zero modes under a counterclockwise exchange of vortices j and $j+1$,

$$\hat{\gamma}_j \mapsto +\hat{\gamma}_{j+1}, \qquad \hat{\gamma}_{j+1} \mapsto -\hat{\gamma}_j, \tag{6.42}$$

which is precisely the braiding statistics of MZMs. [148, 150]

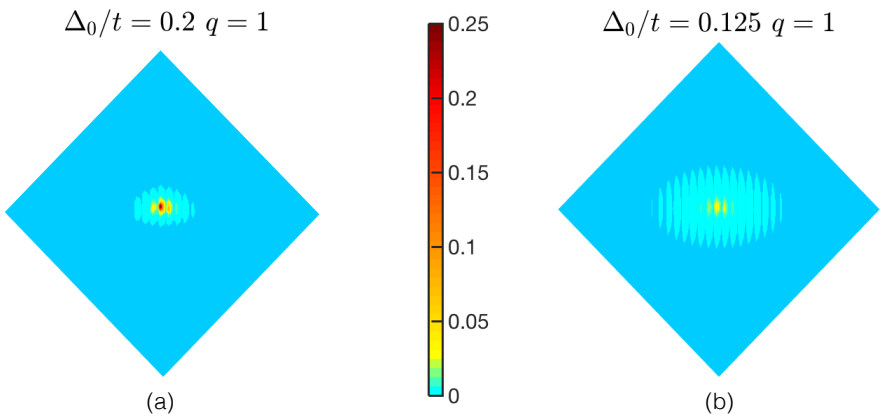

Figure 6·8: Wavefunctions of the zero mode bound to a single Kekulé vortex at the origin for $\Delta_0/U = 0.02$ with $U > t > 0$ and vorticity $q = 1$. The numerics are carried out on a diamond shaped geometry with 61 sites on each edge. (a) $\Delta_0/t = 0.2$; (b) $\Delta_0/t = 0.125$. The zero mode amplitude decreases upon decreasing Δ_0/t and the profile broadens. For a system with open boundary, there is an additional zero mode localized near the boundary which is not shown in the plot.

6.4 Zero modes bound to Kekulé vortices in the network of Majorana nanowires

We now return to the Hamiltonian (6.11) describing the network of quantum nanowires in the presence of a Kekulé gap larger than the Haldane gap. We shall impose a Kekule vortex of vorticity one in magnitude and verify numerically that it binds a "logical" Majorana zero mode.

To this end, we imprint a Kekulé vortex with vorticity $q = \pm 1$ that is centered at the origin, $\boldsymbol{R} = \boldsymbol{0}$, by replacing the uniform t in the dimer Hamiltonian (6.5a) with $t + \delta t_{\boldsymbol{r},\alpha}$ where [compare with Eq. (6.1)]

$$\delta t_{\boldsymbol{r},\alpha} := \Delta_0 \cos\left(\boldsymbol{K}_+ \cdot \boldsymbol{s}_\alpha + \boldsymbol{G} \cdot \boldsymbol{r} + q \arg\left(\boldsymbol{r}\right)\right) \tag{6.43}$$

and $\alpha = \mathtt{x}, \mathtt{y}, \mathtt{z}$. In the continuum limit, this expression yields a Kekulé order parameter with a vortex profile similar to that in Eq. (6.34).

When$|\Delta_0| \gtrsim t^2/U$, we find a zero mode bound to the Kekulé vortex, as shown in Fig. 6·8. The amplitude of this zero mode decays exponentially away from the vortex core. The amplitudes are nonvanishing on sublattices Λ_A and Λ_B, respectively, depending on the sign of the vorticity, $\mathrm{sgn}(q) = \pm 1$. Upon increasing t/U, the band gap decreases as the Kekulé gap competes with the Haldane gap. Consequently, the exponential decay of the zero mode is less pronounced, and the zero mode spreads out further, until the zero mode is eaten by the continuum of single-particle states when the band gap vanishes. When $t^2/U \gtrsim |\Delta_0|$, the Haldane gap dominates over the Kekulé gap and no zero mode can bind to a Kekulé vortex. [224]

6.5 Experimental considerations

6.5.1 Measurement scheme

We now discuss the possibility of measuring the emergent MZMs and verifying their braiding properties within the nanowire network proposed in this chapter. The existence of the "logical" MZMs can be probed via scanning tunneling microscopy (STM), where they manifest themselves as zero-bias peaks in the tunneling differential conductance. In addition, by employing high-resolution STM conductance mapping techniques, it is possible to probe the spatial profile of the MZMs, thereby verifying their localized nature. [229–232]

However, the verification of the existence of the "logical" MZMs is not complete unless one can also verify that braiding the "logical" MZMs acts on the low-energy Hilbert space of the system in the manner characteristic of true MZMs. We now make this idea more precise. For a system with $2N$ "logical" MZMs, each pair of MZMs constitutes a fermionic state that can be either empty or filled. The fermion parity (even or odd, respectively) of each pair then specifies the state of a qubit. Thus, the dimension of the Hilbert space spanned by the quantum states of these

qubits grows as 2^{N-1} once the total fermion parity of the $2N$ MZMs has been fixed. Braiding "logical" MZMs performs unitary transformations on this Hilbert space. Thus, in order to verify that braiding the "logical" MZMs acts in the desired way, one needs a means of measuring the fermion parity of any pair of MZMs. Here, we can again exploit the fact that the "logical" MZMs can be moved adiabatically by adjusting the array of gate voltages. Bringing a pair of "logical" MZMs together by merging two Kekulé vortices effectively "fuses" the two MZMs. Then, in order to determine whether the pair of MZMs were in an even- or odd-fermion-parity state, one can measure the local charge distribution in the vicinity of the fused pair: if there is a finite charge density where the two zero modes were fused together, then they were in an odd-fermion-parity state; if not, then they were in an even-fermion-parity state. Such a measurement can potentially be achieved with scanning single-electron transistor microscopy (SSETM), which can resolve local charge density on the length scale of nanometers. [233, 234] Therefore, in principle, the existence of MZMs and their braiding and fusion properties can be measured by interfacing STM and SSETM probes with the nanowire network.

6.5.2 Experimental parameters

Let $\mathfrak{a}$ be the length of a Majorana nanowire that we are using as a nearest-neighbor bond of the honeycomb lattice (i.e., the lattice spacing of the honeycomb network). We assume that the trimer energy scale U that enters in Eq. (6.11) is $U \sim \Delta_{\rm nw}$, so that the physical Majoranas are almost on top of one another. We seek to express the hopping amplitude t and the Kekulé gap Δ_0 that enter in $\widehat{H}_{\rm dimer} + \delta\widehat{H}_{\rm dimer}$ [see Eqs. (6.11) and (6.13)] in terms of the energy scales entering a single Majorana nanowire.

A single Majorana nanowire wire is modeled as a one-dimensional gas of non-interacting electrons at the chemical potential $V_{\rm g}$ in proximity to an s-wave superconductor, whereby the electronic kinetic energy competes with Zeeman, Rashba spin-

orbit, and s-wave superconducting pairing contributions to the Hamiltonian. [206, 207, 216]

The expression for the topological gap Δ_{nw} of a single Majorana nanowire is [206, 207, 216]

$$\Delta_{\mathrm{nw}} := \frac{g\,\mu_{\mathrm{B}}\,|B_z|}{2} - \sqrt{\Delta_{\mathrm{sc}}^2 + V_{\mathrm{g}}^2} > 0, \tag{6.44a}$$

where g is the effective g-factor in the wire, μ_{B} is the Bohr magneton, $|B_z|$ is the strength of the applied magnetic field along the Cartesian axis z that is perpendicular to the plane in which the Majorana nanowires lie, Δ_{sc} is the proximity-induced superconducting gap of the Majorana nanowire, and the gate potential V_{g} sets the chemical potential in the Majorana nanowire. Physical MZMs are bound to the end points of this Majorana nanowire if and only if

$$\frac{g\mu_{\mathrm{B}}\,|B_z|}{2} > \sqrt{\Delta_{\mathrm{sc}}^2 + V_{\mathrm{g}}^2}. \tag{6.44b}$$

As the decay length for a physical MZM bound to the end points of a Majorana nanowire is

$$\xi_{\mathrm{physical}} = \frac{\hbar\, v_{\mathrm{F,nw}}}{\Delta_{\mathrm{nw}}}, \tag{6.45}$$

where $v_{\mathrm{F,nw}}$ is the Fermi velocity of the Majorana nanowire (which is equal to the spin-orbit coupling in the limit when the Zeeman energy is much smaller than the effective electron mass times the spin-orbit coupling in suitable units), the overlap between two physical MZMs is then approximately given by

$$t \sim \frac{\hbar\, v_{\mathrm{F,nw}}}{\mathfrak{a}}\,\kappa\, e^{-\kappa}, \qquad \kappa := \frac{\mathfrak{a}\,\Delta_{\mathrm{nw}}}{\hbar\, v_{\mathrm{F,nw}}}, \tag{6.46}$$

when measured in units of energy. This overlap is controlled by the dimensionless

ratio

$$\kappa = \frac{\mathfrak{a}}{\xi_{\mathrm{sc}}} \frac{\Delta_{\mathrm{nw}}}{\Delta_{\mathrm{sc}}}, \tag{6.47a}$$

where we have introduced the proximity-induced superconducting coherence length

$$\xi_{\mathrm{sc}} := \frac{\hbar\, v_{\mathrm{F,nw}}}{\Delta_{\mathrm{sc}}}. \tag{6.47b}$$

The overlap t is thus exponentially suppressed by either increasing the ratio between the length of the Majorana nanowire and the proximity-induced superconducting coherence length or the ratio between the topological gap and the proximity-induced superconducting gap.

When estimating the size of the Kekulé gap Δ_0, we assume that we can vary the gate voltages V_{g} along the nearest-neighbor bonds on the honeycomb lattice by the amount δV_{g}. To leading order in δV_{g}, the topological gap (6.44a) changes by $\Delta_{\mathrm{nw}} \to \Delta_{\mathrm{nw}} + \delta\Delta_{\mathrm{nw}}$ with

$$\delta\Delta_{\mathrm{nw}} \to -\frac{V_{\mathrm{g}}}{\sqrt{\Delta_{\mathrm{sc}}^2 + V_{\mathrm{g}}^2}}\, \delta V_{\mathrm{g}}. \tag{6.48}$$

Substituting this expression into (6.46) and expanding to leading order in δV_{g}, we obtain $t \to t + \delta t$, where

$$\frac{\delta t}{t} \approx \frac{\kappa - 1}{\kappa}\, \delta\kappa, \qquad \delta\kappa := \frac{\mathfrak{a}}{\hbar\, v_{\mathrm{F,nw}}} \frac{V_{\mathrm{g}}^2}{\sqrt{\Delta_{\mathrm{sc}}^2 + V_{\mathrm{g}}^2}} \frac{\delta V_{\mathrm{g}}}{V_{\mathrm{g}}}. \tag{6.49}$$

When expressed in units of the uniform hopping amplitude t, we arrive at the final expressions

$$\frac{\delta t}{t} \approx \frac{\kappa - 1}{\kappa} \frac{\mathfrak{a}}{\xi_{\mathrm{sc}}} \frac{V_{\mathrm{g}}^2/\Delta_{\mathrm{sc}}^2}{\sqrt{1 + V_{\mathrm{g}}^2/\Delta_{\mathrm{sc}}^2}} \frac{\delta V_{\mathrm{g}}}{V_{\mathrm{g}}} \tag{6.50a}$$

for the Kekulé perturbation (6.13) with the non-uniform hopping amplitude δt,

$$\frac{\Delta_0}{t} \sim \frac{\delta t}{t} \tag{6.50b}$$

for the Kekulé gap in Eq. (6.23), and

$$\xi_{\text{logical}} := \frac{t}{\delta t}\,\mathfrak{a} \tag{6.50c}$$

for the decay length of a logical MZM.

Let us now show that a great deal of control over the size of the logical MZMs is attainable using the same material parameters as in current experimental setups. We focus on the InSb/Al systems reviewd in [203]. The proximity induced superconducting gap is $\Delta_{\text{sc}} \sim 0.2\,\text{meV}$, while the Fermi velocity can be estimated from the quoted range of values of the spin-orbit coupling, i.e., $v_{\text{F,nw}} \sim 0.2{-}1.0\ \text{eV}\times\mathring{A}$. Hence, the proximity-induced superconducting correlation length is in the range $\xi_{\text{sc}} \sim 100 - 500\,\text{nm}$. For wires of length $\mathfrak{a} \sim 1\mu\text{m}$, one thus have ratios in the range $\mathfrak{a}/\xi_{\text{sc}} \sim 2 - 10$.

We proceed by choosing to work with $\kappa \approx 2$, which yields significant overlap between the zero modes at the endpoints of the wires (and can be selected via the magnetic field, as we clarify below). According to Eq. (6.47a), this choice gives a hopping amplitude $t \sim 0.27\,\hbar\, v_{\text{F,nw}}/\mathfrak{a} = 0.27\,(\xi_{\text{sc}}/\mathfrak{a})\,\Delta_{\text{sc}} \sim 0.027\,\Delta_{\text{sc}} - 0.14\,\Delta_{\text{sc}}$. The choice of working with $\kappa \approx 2$ corresponds to a magnetic field such that $\Delta_{\text{nw}} \approx \kappa\,(\xi_{\text{sc}}/\mathfrak{a})\,\Delta_{\text{sc}} \sim 0.2\,\Delta_{\text{sc}} - 1.0\,\Delta_{\text{sc}}$ according to Eq. (6.47a).

With the choice of $\kappa \approx 2$, the Kekulé gap (6.50b) is approximately given by

$$\frac{\Delta_0}{t} \approx \frac{1}{2}\frac{\mathfrak{a}}{\xi_{\text{sc}}}\,\frac{V_{\text{g}}^2/\Delta_{\text{sc}}^2}{\sqrt{1+V_{\text{g}}^2/\Delta_{\text{sc}}^2}}\frac{\delta V_{\text{g}}}{V_{\text{g}}}. \tag{6.51}$$

The prefactor in front of $\delta V_{\text{g}}/V_{\text{g}}$ on the right-hand side can be chosen to be of order one by choosing the ratio $V_{\text{g}}^2/\Delta_{\text{sc}}^2$ in the expression above so as to compensate the factor $\mathfrak{a}/(2\xi_{\text{sc}}) \sim 1.0 - 5.0$. (The corresponding bias V_{g} should thus be of roughly the same order as Δ_{sc}.) If so, the ratio $\Delta_0/t \approx \delta V_{\text{g}}/V_{\text{g}}$. Consequently, by using modulations with δV_{g} of the same order as V_{g}, one can make the Kekulé gap of the order of t, and hence the size of the logical MZMs as small as the length scale of the

wire size $\mathfrak{a}$.

We remark that for the scheme that we propose, the shorter the wires the larger the energies scales of the effective model. The hopping amplitude t would roughly double (if one chooses to operate at the same $\kappa \approx 2$) if one uses wires that are half as long. (This energy scale is set by $\hbar v_{\mathrm{F,nw}}/\mathfrak{a}$.) So for a 500 nm (300 nm) wire, the energy scale of $t \sim 0.054\,\Delta_{\mathrm{sc}} - 0.27\,\Delta_{\mathrm{sc}}$ ($t \sim 0.09\,\Delta_{\mathrm{sc}} - 0.45\,\Delta_{\mathrm{sc}}$) follows.

6.6 Summary

In this chapter, we presented a hierarchical architecture for building "logical" Majorana zero modes using "physical" Majorana zero modes at the Y-junctions of a hexagonal network of semiconductor nanowires. In a nutshell, the essence of our approach is that one can build Majoranas out of Majoranas that are, in turn, built of Majoranas (see Fig. 6·1). The "emergent" or "logical" Majoranas can be moved adiabatically and are not restricted to be centered at sites of a lattice, although their microscopic or "physical" constituents are. What this construction provides is the ability to program where one wants to place the "logical" Majoranas by controlling applied gate biases on the nanowires within the hexagonal network. We present in Eq. (6.1) a simple expression for the bias voltages that would place v Majoranas at the centers of Kekulé vortices at locations $\boldsymbol{R}_n(t), n = 1, \cdots, v$, which can be varied as functions of time in a prescribed way.

Within the hierarchical construction of quantum Hall states, novel quasiparticles appear as a result of condensation of other types of quasiparticles. Such a hierarchy can be viewed within the broader context of emergence, where novel excitations appear at different scales. Our scheme is a form of *engineered* emergence, where one can, by design, create novel excitations starting from simple building blocks. In our case, we have a meta-circular realization of Majoranas, for the emergent particles at

the top of the hierarchy coincide with those used as building blocks (those at the bottom level of the hierarchy). The distinction between the Majoranas at the different levels of the hierarchy is the fact that the ones on top are movable, while the ones on the bottom are static. This is an important difference, as the ability to move the Majoranas in the plane in a programmable way should permit one to braid them, providing a *direct* means to probe their non-Abelian statistics.

Chapter 7

Concluding Remarks

In this dissertation, we have studied the entanglement spectrum properties of highly entangled states, and presented novel architectures for quantum computation potentially realizable using near-term technologies.

In Part I, we showed that in general the entanglement spectrum of highly entangled states contains much richer information than the von Neumann entropy. In particular, it allows one to quantify the degree of randomness of a quantum states beyond entropic diagnostics. Chapter 2 mainly focuses on highly excited *e*igenstates of generic non-integrable Hamiltonians, which further undergo a transition from thermalizing phase to many-body localized phase upon introducing quenched disorders. We show that the density of states of the entanglement spectrum typically feature a two-component structure, with the information on the level of randomness contained in the smallest singular values part. In Chapter 3, we further extend the discussion to quantum quenches, and demonstrate that the different level spacing distributions of the entanglement spectrum defines a notion of entanglement complexity, which can be probed by the efficiency of disentangling a state without precise knowledge of the time evolution operator. Motivated by the concept of entanglement complexity, in Chapter 4 we study the dynamics of entanglement spectrum and quantify the degree of randomness generated by scrambling in different random circuits of braids. These results extend our understanding of quantum entanglement in many-body systems out of equilibrium, and provide further insights into the rapidly growing field of quantum

chaos and information scrambling.

In Part II, we present two novel architectures for quantum computation. Chapter 5 dicusses alternatives to the intensively studied quantum adiabatic algorithm, which could yield better performance for a given amount of computation time. As a direct application of the Pontryagin's minimum principle in optimal conrol theory, we show that the optimal evolution protocol is of the bang-bang form. The advantage of the optimal bang-bang protocol over the adiabatic algorithm remains even in the presence of weak external noise and coupling to a thermal bath. Chapter 6 considers the platform of topological quantum computation based on Majorana zero modes. We propose a hierarchical construction of logical qubits using semiconducting Majorana nanowire networks. This architectures allows Majorana zero modes to be adiabatically braided in a meaningful and controllable manner. Both proposals we give are promising within current experimental technologies, and are very likely realizable on near-term devices.

We close by pointing out a few promising future directions.

7.1 Entanglement spectrum and operator spreading

The earliest definition of quantum chaos was formulated in terms of the random matrix theory description of eigenenergy spectrum statistics. To resolve the exponentially small energy level spacings of generic non-integrable Hamiltonians, the total evolution time must be long accordingly. In this sense, this formulation may be viewed as a late-time description of quantum chaotic systems. Recent revival of the subject has been focusing on early-time diagnostics of quantum chaos, which leads to the notion of out-of-time ordered correlators and operator spreading.

It has been shown that there exits a characteristic velocity known as the "butterfly velocity" which governs the mutual information and local operator spreading [16,

34, 35]. Another characteristic velocity governing the rate of entanglement entropy production known as the "entanglement velocity" has also been identified [16]. It is thus natural to ask: what is the characteristic velocity or time scale governing the dynamics of the entanglement spectrum? More precisely, what is the physical meaning of the onset of level repulsion in the entanglement spectrum under time evolution? How is this velocity related to operator spreading? These questions have not been touched upon until very recently, when there is numerical evidence indicating that the onset of level repulsion in the entanglement spectrum is also governed by the butterfly velocity, and hence operator spreading [235, 236]. There is still lots of work to be done along this direction to fully understand the entanglement features of many-body systems in and out of equilibrium.

7.2 Variational quantum algorithms and implementation on near-term devices

The bang-bang protocol was first proposed by Farhi *e*t al. as an ingenious guess [46, 182] motivated by its provable scaling for certain problems. We show in this dissertation that this protocol is in fact optimal. However, there remains lots of questions that we still barely understand. For example, what is the most efficient way of implementing the outer-loop optimization algorithm classically? And more fundamentally, how does the system manage to eliminate the excitations produced during the evolution due to the lack of adiabaticity, such that the final state has large overlap with the desired ground state? Can this protocol be used for preparing topologically nontrivial states starting from trivial initial states?

Some of the above questions have been partially addressed since the work of Chapter 5 (also ref. [237]). Powerful tools from reinforcement learning have been employed to find the optimial protocol for a given problem, which also unveils the

glassiness in the landscape of controls [238, 239]. Efficient heuristic algorithms for the classical optimization step have been proposed based on an interesting finding of the pattern in the optimal protocols [240]. Besides hard computational problems, the bang-bang protocol has also been applied to preparing topologically nontrivial states [241]. In certain cases, e.g. the transverse-field Ising model, the bang-bang protocol can prepare the desired states with perfect fidelity, with the number of iterations linear in system size [241, 242]. This perfect fidelity may indicate a so-far unknown analytical solution of the protocol. Further insights can be gained along this line of work.

7.3 Engineered phases of matter with full tunability

In Chapter 6 (also ref. [243]), we give an example of constructing logical Majoranas from a network of nanowires. In a more general sense, our construction exemplifies a way of engineering nontrivial phases of matter from smaller building blocks which are themselves nontrivial. Theoretically, this philosophy has been taken in wire constructions of Abelian and non-Abelian topological phases in two and three dimensions [244–248]. Experimentally, it is also possible to simulate nontrivial properties of electronic systems using fabricated photonic crystals [249]. Engineered phases of matter also have the advantage of full tunability as compared to real world materials. While in our example, the emergent excitation has the same nature as the microscopic constituents (i.e. they are both Majoranas), theoretically it has been shown that by adding appropriate interactions, novel excitations different from the microscopic constituents can also emerge. One can thus envision a plethora of novel phases of matter not directly realizable in real world materials to be engineered artificially using simple building blocks [250].

List of Journal Abbreviations

Adv. Phys.	Advances in Physics
Ann. Phys.	Annals of Physics
Annu. Rev. Condens. Matt Phys.	Annual Review of Condensed Matter Physics
App. Phys. Lett.	Applied Physics Letters
Commun. Math. Phys.	Communications in Mathematical Physics
Front. Phys.	Frontiers in Physics
J. High Energy Phys.	Journal of High Energy Physics
J. Phys. A	Journal of Physics A
J. Phys. Soc. Jpn.	Journal of the Physical Society of Japan
J. Stat. Mech.	Journal of Statistical Mechanics: Theory and Experiment
Mod. Phys. Lett. B	Modern Physics Letters B
Nat. Commun.	Nature Communications
Nat. Mater.	Nature Materials
New J. Phys.	New Journal of Physics
Nucl. Phys. B	Nuclear Physics B
Phys. Lett. A	Physics Letters A
Phys. Rev. A	Physical Review A: Atomic, Molecular, and Optical Physics and Quantum Information
Phys. Rev. B	Physical Review B: Condensed Matter and Materials Physics
Phys. Rev. D	Physical Review D: Particles, Fields, Gravitation and Cosmology
Phys. Rev. E	Physical Review E: Statistical, Nonlinear, Biological and Soft Matter Physics
Phys. Rev. X	Physical Review X
Phys. Rev. Lett.	Physical Review Letters
Proc. IEEE	Proceedings of the IEEE
Proc. Natl. Acad. Sci. U.S.A	Proceedings of the National Academy of Sciences of the United States of America

Proc. R. Soc. Lond. A	Proceedings of the Royal Society A
Quantum Inf. Process.	Quantum Information Processing
Rep. Prog. Phys.	Reports on Progress in Physics
Rev. Mod. Phys.	Review of Modern Physics
Sci. Rep.	Scientific Reports

Bibliography

[1] J. S. Bell, *Speakable and unspeakable in quantum mechanics: Collected papers on quantum philosophy* (Cambridge University Press, 2004).

[2] A. Peres, *Quantum theory: concepts and methods*, Vol. 57 (Springer Science & Business Media, 2006).

[3] M. A. Nielsen and I. Chuang, *Quantum computation and quantum information* (Cambridge University Press, 2010).

[4] C. H. Bennett, G. Brassard, C. Crépeau, R. Jozsa, A. Peres, and W. K. Wootters, Phys. Rev. Lett. **70**, 1895 (1993).

[5] L. Amico, R. Fazio, A. Osterloh, and V. Vedral, Rev. Mod. Phys. **80**, 517 (2008).

[6] M. Levin and X.-G. Wen, Phys. Rev. Lett. **96**, 110405 (2006).

[7] A. Kitaev and J. Preskill, Phys. Rev. Lett. **96**, 110404 (2006).

[8] U. Schollwöck, Ann. Phys. **326**, 96 (2011).

[9] G. Vidal, Phys. Rev. Lett. **91**, 147902 (2003).

[10] G. Vidal, Phys. Rev. Lett. **93**, 040502 (2004).

[11] M. Levin and C. P. Nave, Phys. Rev. Lett. **99**, 120601 (2007).

[12] G. Evenbly and G. Vidal, Phys. Rev. Lett. **115**, 180405 (2015).

[13] G. Vidal, Phys. Rev. Lett. **101**, 110501 (2008).

[14] G. Evenbly and G. Vidal, Phys. Rev. B **79**, 144108 (2009).

[15] A. Nahum, J. Ruhman, S. Vijay, and J. Haah, Phys. Rev. X **7**, 031016 (2017).

[16] C. W. von Keyserlingk, T. Rakovszky, F. Pollmann, and S. L. Sondhi, Phys. Rev. X **8**, 021013 (2018).

[17] M. Srednicki, Phys. Rev. E **50**, 888 (1994).

[18] M. Rigol, V. Dunjko, and M. Olshanii, Nature **452**, 854 (2008).

[19] A. Pal and D. A. Huse, Phys. Rev. B **82**, 174411 (2010).

[20] R. Nandkishore and D. A. Huse, Annu. Rev. Condens. Matter Phys. **6**, 15 (2015).

[21] J. H. Bardarson, F. Pollmann, and J. E. Moore, Phys. Rev. Lett. **109**, 017202 (2012).

[22] H. Li and F. D. M. Haldane, Phys. Rev. Lett. **101**, 010504 (2008).

[23] C. Chamon and E. R. Mucciolo, Phys. Rev. Lett. **109**, 030503 (2012).

[24] Z.-C. Yang, S. Kourtis, C. Chamon, E. R. Mucciolo, and A. E. Ruckenstein, Phys. Rev. E **97**, 033303 (2018).

[25] S. Kourtis, C. Chamon, E. R. Mucciolo, and A. E. Ruckenstein, arXiv preprint arXiv:1805.00475 (2018).

[26] K. Meichanetzidis and S. Kourtis, arXiv preprint arXiv:1807.02119 (2018).

[27] D. N. Page, Phys. Rev. Lett. **71**, 1291 (1993).

[28] D. Shaffer, C. Chamon, A. Hamma, and E. R. Mucciolo, J. Stat. Mech. **2014**, P12007 (2014).

[29] Z.-W. Liu, S. Lloyd, E. Y. Zhu, and H. Zhu, Phys. Rev. Lett. **120**, 130502 (2018).

[30] Z.-W. Liu, S. Lloyd, E. Zhu, and H. Zhu, J. High Energy Phys. **2018**, 41 (2018).

[31] S. D. Geraedts, R. Nandkishore, and N. Regnault, Phys. Rev. B **93**, 174202 (2016).

[32] N. Regnault and R. Nandkishore, Phys. Rev. B **93**, 104203 (2016).

[33] C. Chamon, A. Hamma, and E. R. Mucciolo, Phys. Rev. Lett. **112**, 240501 (2014).

[34] A. Nahum, S. Vijay, and J. Haah, Phys. Rev. X **8**, 021014 (2018).

[35] V. Khemani, A. Vishwanath, and D. A. Huse, Phys. Rev. X **8**, 031057 (2018).

[36] E. Farhi, J. Goldstone, S. Gutmann, J. Lapan, A. Lundgren, and D. Preda, Science **292**, 472 (2001).

[37] A. Mizel, D. A. Lidar, and M. Mitchell, Phys. Rev. Lett. **99**, 070502 (2007).

[38] V. S. Denchev, S. Boixo, S. V. Isakov, N. Ding, R. Babbush, V. Smelyanskiy, J. Martinis, and H. Neven, Phys. Rev. X **6**, 031015 (2016).

[39] A. P. Young, S. Knysh, and V. N. Smelyanskiy, Phys. Rev. Lett. **104**, 020502 (2010).

[40] A. P. Young, S. Knysh, and V. N. Smelyanskiy, Phys. Rev. Lett. **101**, 170503 (2008).

[41] I. Hen and A. P. Young, Phys. Rev. E **84**, 061152 (2011).

[42] S. Knysh and V. Smelyanskiy, arXiv preprint arXiv:1005.3011 (2010).

[43] E. Farhi, D. Gosset, I. Hen, A. W. Sandvik, P. Shor, A. P. Young, and F. Zamponi, Phys. Rev. A **86**, 052334 (2012).

[44] E. Crosson, E. Farhi, C. Y.-Y. Lin, H.-H. Lin, and P. Shor, arXiv preprint arXiv:1401.7320 (2014).

[45] D. S. Steiger, T. F. Rønnow, and M. Troyer, Phys. Rev. Lett. **115**, 230501 (2015).

[46] E. Farhi, J. Goldstone, and S. Gutmann, arXiv preprint arXiv:1411.4028 (2014).

[47] A. Peruzzo, J. McClean, P. Shadbolt, M.-H. Yung, X.-Q. Zhou, P. J. Love, A. Aspuru-Guzik, and J. L. O'brien, Nat. Commun. **5**, 4213 (2014).

[48] M.-H. Yung, J. Casanova, A. Mezzacapo, J. Mcclean, L. Lamata, A. Aspuru-Guzik, and E. Solano, Sci. Rep. **4**, 3589 (2014).

[49] D. Wecker, M. B. Hastings, and M. Troyer, Phys. Rev. A **92**, 042303 (2015).

[50] D. Wecker, M. B. Hastings, and M. Troyer, Phys. Rev. A **94**, 022309 (2016).

[51] J. R. McClean, J. Romero, R. Babbush, and A. Aspuru-Guzik, New J. Phys. **18**, 023023 (2016).

[52] D. Sels and A. Polkovnikov, Proc. Natl. Acad. Sci. U.S.A **114**, E3909 (2017).

[53] D. Sherrington and S. Kirkpatrick, Phys. Rev. Lett. **35**, 1792 (1975).

[54] C. Nayak, S. H. Simon, A. Stern, M. Freedman, and S. Das Sarma, Rev. Mod. Phys. **80**, 1083 (2008).

[55] J. Alicea, Rep. Prog. Phys. **75**, 076501 (2012).

[56] L. Amico, R. Fazio, A. Osterloh, and V. Vedral, Rev. Mod. Phys. **80**, 517 (2008).

[57] J. Eisert, M. Cramer, and M. B. Plenio, Rev. Mod. Phys. **82**, 277 (2010).

[58] X. G. Wen and Q. Niu, Phys. Rev. B **41**, 9377 (1990).

[59] X.-G. Wen, Phys. Rev. Lett. **90**, 016803 (2003).

[60] L. Susskind, Fortschritte der Physik **64**, 49 (2016).

[61] J. M. Deutsch, Phys. Rev. A **43**, 2046 (1991).

[62] V. Oganesyan and D. A. Huse, Phys. Rev. B **75**, 155111 (2007).

[63] M. Serbyn, Z. Papić, and D. A. Abanin, Phys. Rev. Lett. **110**, 260601 (2013).

[64] T. Jörg, F. Krzakala, J. Kurchan, and A. C. Maggs, Phys. Rev. Lett. **101**, 147204 (2008).

[65] C. R. Laumann, A. Pal, and A. Scardicchio, Phys. Rev. Lett. **113**, 200405 (2014).

[66] C. L. Baldwin, C. R. Laumann, A. Pal, and A. Scardicchio, Phys. Rev. B **93**, 024202 (2016).

[67] M. L. Mehta, *Random matrices*, Vol. 142 (Elsevier, 2004).

[68] D. S. Rokhsar and S. A. Kivelson, Phys. Rev. Lett. **61**, 2376 (1988).

[69] C. Castelnovo, C. Chamon, C. Mudry, and P. Pujol, Ann. Phys. **318**, 316 (2005).

[70] D. J. Luitz, N. Laflorencie, and F. Alet, Phys. Rev. B **91**, 081103 (2015).

[71] A. W. Sandvik, in *AIP Conf. Proc.*, Vol. 1297 (AIP, 2010) pp. 135–338.

[72] V. A. Marchenko and L. A. Pastur, Mathematics of the USSR Sbornik **114**, 507 (1967).

[73] M. Žnidarič, Journal of Physics A: Mathematical and Theoretical **40**, F105 (2006).

[74] J. M. Deutsch, H. Li, and A. Sharma, Phys. Rev. E **87**, 042135 (2013).

[75] B. Bauer and C. Nayak, J. Stat. Mech. **2013**, P09005 (2013).

[76] B. Derrida, Phys. Rev. Lett. **45**, 79 (1980).

[77] X. Chen, X. Yu, G. Y. Cho, B. K. Clark, and E. Fradkin, Phys. Rev. B **92**, 214204 (2015).

[78] F. Verstraete, J. J. García-Ripoll, and J. I. Cirac, Phys. Rev. Lett. **93**, 207204 (2004).

[79] F. Verstraete and J. I. Cirac, arXiv preprint cond-mat/0407066 (2004).

[80] Y. Y. Atas, E. Bogomolny, O. Giraud, and G. Roux, Phys. Rev. Lett. **110**, 084101 (2013).

[81] A. Hamma, R. Ionicioiu, and P. Zanardi, Phys. Lett. A **337**, 22 (2005).

[82] S. M. Giampaolo and B. C. Hiesmayr, Phys. Rev. A **92**, 012306 (2015).

[83] S. Das, S. Shankaranarayanan, and S. Sur, arXiv preprint arXiv:0806.0402 (2008).

[84] H. Pichler, G. Zhu, A. Seif, P. Zoller, and M. Hafezi, Phys. Rev. X **6**, 041033 (2016).

[85] J. Gemmer, M. Michel, and G. Mahler, "Quantum thermodynamics: Emergence of thermodynamic behavior within composite quantum systems, volume 784 of lecture notes in physics," (2009).

[86] S. Popescu, A. J. Short, and A. Winter, Nature Physics **2**, 754 (2006).

[87] P. Reimann, Phys. Rev. Lett. **99**, 160404 (2007).

[88] S. Goldstein, J. L. Lebowitz, R. Tumulka, and N. Zanghì, Phys. Rev. Lett. **96**, 050403 (2006).

[89] E. Lieb, T. Schultz, and D. Mattis, Ann. of Phys. **16**, 407 (1961).

[90] E. Barouch, B. M. McCoy, and M. Dresden, Phys. Rev. A **2**, 1075 (1970).

[91] F. Evers and A. D. Mirlin, Rev. Mod. Phys. **80**, 1355 (2008).

[92] M. Žnidarič, T. c. v. Prosen, and P. Prelovšek, Phys. Rev. B **77**, 064426 (2008).

[93] M. V. Berry and M. Tabor, Proc. R. Soc. Lond. A **356**, 375 (1977).

[94] G. Montambaux, D. Poilblanc, J. Bellissard, and C. Sire, Phys. Rev. Lett. **70**, 497 (1993).

[95] P. Calabrese and J. Cardy, J. Stat. Mech. **2005**, P04010 (2005).

[96] T. c. v. Prosen, Phys. Rev. Lett. **106**, 217206 (2011).

[97] R. G. Pereira, V. Pasquier, J. Sirker, and I. Affleck, J. Stat. Mech. **2014**, P09037 (2014).

[98] K. Kudo and T. Deguchi, J. Phys. Soc. Jpn. **74**, 1992 (2005).

[99] D. A. Huse, R. Nandkishore, and V. Oganesyan, Phys. Rev. B **90**, 174202 (2014).

[100] M. Serbyn, Z. Papić, and D. A. Abanin, Phys. Rev. Lett. **111**, 127201 (2013).

[101] I. H. Kim, A. Chandran, and D. A. Abanin, arXiv preprint arXiv:1412.3073 (2014).

[102] L. Rademaker and M. Ortuño, Phys. Rev. Lett. **116**, 010404 (2016).

[103] A. Chandran, I. H. Kim, G. Vidal, and D. A. Abanin, Phys. Rev. B **91**, 085425 (2015).

[104] J. Yang and A. Hamma, arXiv preprint arXiv:1702.00445 (2017).

[105] M. Friesdorf, A. Werner, M. Goihl, J. Eisert, and W. Brown, New J. Phys. **17**, 113054 (2015).

[106] Z.-C. Yang, C. Chamon, A. Hamma, and E. R. Mucciolo, Phys. Rev. Lett. **115**, 267206 (2015).

[107] M. Serbyn, A. A. Michailidis, D. A. Abanin, and Z. Papić, Phys. Rev. Lett. **117**, 160601 (2016).

[108] G. Lindblad, in *Quantum Probability and Applications II* (Springer, 1985) pp. 348–360.

[109] M. C. Gutzwiller, *Chaos in classical and quantum mechanics*, Vol. 1 (Springer Science & Business Media, 2013).

[110] F. Haake, *Quantum signatures of chaos*, Vol. 54 (Springer Science & Business Media, 2013).

[111] L. D'Alessio, Y. Kafri, A. Polkovnikov, and M. Rigol, Adv. Phys. **65**, 239 (2016).

[112] A. Larkin and Y. N. Ovchinnikov, Sov. Phys. JETP **28**, 1200 (1969).

[113] J. Maldacena, S. H. Shenker, and D. Stanford, J. High Energy Phys. **2016**, 106 (2016).

[114] S. H. Shenker and D. Stanford, J. High Energy Phys. **2014**, 67 (2014).

[115] S. H. Shenker and D. Stanford, J. High Energy Phys. **2014**, 46 (2014).

[116] D. A. Roberts, D. Stanford, and L. Susskind, J. High Energy Phys. **2015**, 51 (2015).

[117] A. Kitaev, in *Talk given at the Fundamental Physics Prize Symposium*, Vol. 10 (2014).

[118] J. Maldacena and D. Stanford, Phys. Rev. D **94**, 106002 (2016).

[119] D. A. Roberts and D. Stanford, Phys. Rev. Lett. **115**, 131603 (2015).

[120] D. Stanford, J. High Energy Phys. **2016**, 9 (2016).

[121] D. Chowdhury and B. Swingle, Phys. Rev. D **96**, 065005 (2017).

[122] A. A. Patel, D. Chowdhury, S. Sachdev, and B. Swingle, Phys. Rev. X **7**, 031047 (2017).

[123] N. Lashkari, D. Stanford, M. Hastings, T. Osborne, and P. Hayden, J. High Energy Phys. **2013**, 22 (2013).

[124] P. Hosur, X.-L. Qi, D. A. Roberts, and B. Yoshida, J. High Energy Phys. **2016**, 4 (2016).

[125] C. Jonay, D. A. Huse, and A. Nahum, arXiv preprint arXiv:1803.00089 (2018).

[126] M. Kardar, G. Parisi, and Y.-C. Zhang, Phys. Rev. Lett. **56**, 889 (1986).

[127] T. Rakovszky, F. Pollmann, and C. W. von Keyserlingk, Phys. Rev. X **8**, 031058 (2018).

[128] M. Žnidarič, Phys. Rev. A **76**, 012318 (2007).

[129] M. Žnidarič, Phys. Rev. A **78**, 032324 (2008).

[130] Z.-C. Yang, A. Hamma, S. M. Giampaolo, E. R. Mucciolo, and C. Chamon, Phys. Rev. B **96**, 020408 (2017).

[131] X. Chen and A. W. W. Ludwig, Phys. Rev. B **98**, 064309 (2018).

[132] M. H. Freedman, M. Larsen, and Z. Wang, Commun. Math. Phys. **227**, 605 (2002).

[133] S. Sachdev and J. Ye, Phys. Rev. Lett. **70**, 3339 (1993).

[134] A. Kitaev, in *KITP strings seminar and Entanglement*, Vol. 12 (2015).

[135] There exits an alternative definition of the ES that commonly appears in the literature, by writing the reduced density matrix in the form $\rho_A = \exp(-H)$ and defining the eigenvalue spectrum of the "entanglement Hamiltonian" H as the ES. For our current purpose of level spacing statistics, one can show that these two definitions do not make a difference. We shall adopt the definition in the text for convenience.

[136] D. Poilblanc, Phys. Rev. Lett. **105**, 077202 (2010).

[137] M. A. Metlitski and T. Grover, arXiv preprint arXiv:1112.5166 (2011).

[138] V. Alba, M. Haque, and A. M. Läuchli, Phys. Rev. Lett. **108**, 227201 (2012).

[139] A. J. A. James and R. M. Konik, Phys. Rev. B **87**, 241103 (2013).

[140] V. Alba, M. Haque, and A. M. Läuchli, Phys. Rev. Lett. **110**, 260403 (2013).

[141] F. Kolley, S. Depenbrock, I. P. McCulloch, U. Schollwöck, and V. Alba, Phys. Rev. B **88**, 144426 (2013).

[142] I. Pižorn, F. Verstraete, and R. M. Konik, Phys. Rev. B **88**, 195102 (2013).

[143] A. Chandran, V. Khemani, and S. L. Sondhi, Phys. Rev. Lett. **113**, 060501 (2014).

[144] An exception is found in excited states of many-body localized states, which show a power-law decay in the entanglement spectrum while exhibiting area-law entanglement. See: M. Serbyn, A. A. Michailidis, D. A. Abanin, and Z. Papić, Phys. Rev. Lett. **117**, 160601 (2016).

[145] J. Cotler, N. Hunter-Jones, J. Liu, and B. Yoshida, J. High Energy Phys. **2017**, 48 (2017).

[146] C. Nayak and F. Wilczek, Nucl. Phys. B **479**, 529 (1996).

[147] G. Moore and N. Read, Nucl. Phys. B **360**, 362 (1991).

[148] N. Read and D. Green, Phys. Rev. B **61**, 10267 (2000).

[149] L. H. Kauffman, *Knots and physics*, Vol. 1 (World scientific, 2001).

[150] D. A. Ivanov, Phys. Rev. Lett. **86**, 268 (2001).

[151] S. Bravyi, Phys. Rev. A **73**, 042313 (2006).

[152] N. E. Bonesteel, L. Hormozi, G. Zikos, and S. H. Simon, Phys. Rev. Lett. **95**, 140503 (2005).

[153] L. Hormozi, G. Zikos, N. E. Bonesteel, and S. H. Simon, Phys. Rev. B **75**, 165310 (2007).

[154] N. Read and E. Rezayi, Phys. Rev. B **59**, 8084 (1999).

[155] A. Feiguin, S. Trebst, A. W. W. Ludwig, M. Troyer, A. Kitaev, Z. Wang, and M. H. Freedman, Phys. Rev. Lett. **98**, 160409 (2007).

[156] A. Chandran, M. D. Schulz, and F. J. Burnell, Phys. Rev. B **94**, 235122 (2016).

[157] W. Fu and S. Sachdev, Phys. Rev. B **94**, 035135 (2016).

[158] J. Sonner and M. Vielma, J. High Energy Phys. **2017**, 149 (2017).

[159] C. Liu, X. Chen, and L. Balents, arXiv preprint arXiv:1709.06259 (2017).

[160] Y. Huang and Y. Gu, arXiv preprint arXiv:1709.09160 (2017).

[161] I. Kourkoulou and J. Maldacena, arXiv preprint arXiv:1707.02325 (2017).

[162] A. Eberlein, V. Kasper, S. Sachdev, and J. Steinberg, Phys. Rev. B **96**, 205123 (2017).

[163] The Page entropy for the Fibonacci chain with contrained Hilbert space has a correction $\Delta S \approx 0.513595$, which is slightly larger than 1/2 for the unconstrained case. See: S. C. Morampudi, A. Chandran, and C. R. Laumann, arXiv: 1810.04157. However, this correction is very small and is thus negligible for our choice of the system size.

[164] L. H. Kauffman and S. J. Lomonaco Jr, in *Proceedings Of The Conference In Honor Of CN Yang's 85th Birthday: Statistical Physics, High Energy, Condensed Matter and Mathematical Physics* (World Scientific, 2008) pp. 277–295.

[165] C. Delaney, E. C. Rowell, and Z. Wang, Revista Colombiana de Matemáticas **50**, 211 (2016).

[166] T. Kadowaki and H. Nishimori, Phys. Rev. E **58**, 5355 (1998).

[167] E. Farhi, J. Goldstone, S. Gutmann, and M. Sipser, arXiv preprint quant-ph/0001106 (2000).

[168] A. Perdomo-Ortiz, S. E. Venegas-Andraca, and A. Aspuru-Guzik, Quantum Inf. Process. **10**, 33 (2011).

[169] T. Singal and S. Ghosh, J. Phys. A **49**, 165304 (2016).

[170] Q. Zhuang, Phys. Rev. A **90**, 052317 (2014).

[171] A. T. Rezakhani, W.-J. Kuo, A. Hamma, D. A. Lidar, and P. Zanardi, Phys. Rev. Lett. **103**, 080502 (2009).

[172] B. Heim, T. F. Rønnow, S. V. Isakov, and M. Troyer, Science **348**, 215 (2015).

[173] W. Rohringer, R. Buecker, S. Manz, T. Betz, C. Koller, M. Goebel, A. Perrin, J. Schmiedmayer, and T. Schumm, Appl. Phys. Lett. **93**, 264101 (2008).

[174] S. Rosi, A. Bernard, N. Fabbri, L. Fallani, C. Fort, M. Inguscio, T. Calarco, and S. Montangero, Phys. Rev. A **88**, 021601 (2013).

[175] A. Rahmani, T. Kitagawa, E. Demler, and C. Chamon, Phys. Rev. A **87**, 043607 (2013).

[176] A. Rahmani, Mod. Phys. Lett. B **27**, 1330019 (2013).

[177] J. R. McClean, M. E. Kimchi-Schwartz, J. Carter, and W. A. de Jong, Phys. Rev. A **95**, 042308 (2017).

[178] Y. Shen, X. Zhang, S. Zhang, J.-N. Zhang, M.-H. Yung, and K. Kim, Phys. Rev. A **95**, 020501 (2017).

[179] C. Eichler, J. Mlynek, J. Butscher, P. Kurpiers, K. Hammerer, T. J. Osborne, and A. Wallraff, Phys. Rev. X **5**, 041044 (2015).

[180] P. J. J. O'Malley, R. Babbush, I. D. Kivlichan, J. Romero, J. R. McClean, R. Barends, J. Kelly, P. Roushan, A. Tranter, N. Ding, B. Campbell, Y. Chen, Z. Chen, B. Chiaro, A. Dunsworth, A. G. Fowler, E. Jeffrey, E. Lucero, A. Megrant, J. Y. Mutus, M. Neeley, C. Neill, C. Quintana, D. Sank, A. Vainsencher, J. Wenner, T. C. White, P. V. Coveney, P. J. Love, H. Neven, A. Aspuru-Guzik, and J. M. Martinis, Phys. Rev. X **6**, 031007 (2016).

[181] E. Farhi, J. Goldstone, and S. Gutmann, arXiv preprint arXiv:1411.4028 (2014).

[182] E. Farhi and A. W. Harrow, arXiv preprint arXiv:1602.07674 (2016).

[183] C. Y.-Y. Lin and Y. Zhu, arXiv preprint arXiv:1601.01744 (2016).

[184] A. E. Bryson, *Applied optimal control: optimization, estimation and control* (Routledge, 2018).

[185] L. S. Pontryagin, *Mathematical theory of optimal processes* (Routledge, 2018).

[186] R. F. Stengel, *Optimal control and estimation* (Courier Corporation, 1994).

[187] C. Brif, M. D. Grace, M. Sarovar, and K. C. Young, New J. Phys. **16**, 065013 (2014).

[188] K. J. Astrom, Proc. IEEE **75**, 185 (1987).

[189] C. Brif, R. Chakrabarti, and H. Rabitz, New J. Phys. **12**, 075008 (2010).

[190] D. Dong and I. R. Petersen, IET Control Theory & Applications **4**, 2651 (2010).

[191] A. Lucas, Front. Phys. **2**, 5 (2014).

[192] T. Karzig, A. Rahmani, F. von Oppen, and G. Refael, Phys. Rev. B **91**, 201404 (2015).

[193] A. Rahmani, B. Seradjeh, and M. Franz, Phys. Rev. B **96**, 075158 (2017).

[194] H. Pichler, J. Schachenmayer, A. J. Daley, and P. Zoller, Phys. Rev. A **87**, 033606 (2013).

[195] A. Rahmani, Phys. Rev. A **92**, 042110 (2015).

[196] H.-P. Breuer, F. Petruccione, *et al.*, *The theory of open quantum systems* (Oxford University Press on Demand, 2002).

[197] A. Dutta, A. Rahmani, and A. del Campo, Phys. Rev. Lett. **117**, 080402 (2016).

[198] R. Barends, A. Shabani, L. Lamata, J. Kelly, A. Mezzacapo, U. Las Heras, R. Babbush, A. G. Fowler, B. Campbell, Y. Chen, *et al.*, Nature **534**, 222 (2016).

[199] M. H. S. Amin, C. J. S. Truncik, and D. V. Averin, Phys. Rev. A **80**, 022303 (2009).

[200] T. Albash, S. Boixo, D. A. Lidar, and P. Zanardi, New J. Phys. **14**, 123016 (2012).

[201] S. Boixo, V. N. Smelyanskiy, A. Shabani, S. V. Isakov, M. Dykman, V. S. Denchev, M. H. Amin, A. Y. Smirnov, M. Mohseni, and H. Neven, Nat. Commun. **7**, 10327 (2016).

[202] M. Mohseni, P. Read, H. Neven, S. Boixo, V. Denchev, R. Babbush, A. Fowler, V. Smelyanskiy, and J. Martinis, Nature News **543**, 171 (2017).

[203] R. M. Lutchyn, E. P. A. M. Bakkers, L. P. Kouwenhoven, P. Krogstrup, C. M. Marcus, and Y. Oreg, Nature Reviews Materials , 1 (2018).

[204] J. D. Sau, R. M. Lutchyn, S. Tewari, and S. Das Sarma, Phys. Rev. Lett. **104**, 040502 (2010).

[205] J. Alicea, Phys. Rev. B **81**, 125318 (2010).

[206] R. M. Lutchyn, J. D. Sau, and S. Das Sarma, Phys. Rev. Lett. **105**, 077001 (2010).

[207] Y. Oreg, G. Refael, and F. von Oppen, Phys. Rev. Lett. **105**, 177002 (2010).

[208] S. B. Chung, H.-J. Zhang, X.-L. Qi, and S.-C. Zhang, Phys. Rev. B **84**, 060510 (2011).

[209] M. Duckheim and P. W. Brouwer, Phys. Rev. B **83**, 054513 (2011).

[210] A. C. Potter and P. A. Lee, Phys. Rev. B **85**, 094516 (2012).

[211] L. Fu and C. L. Kane, Phys. Rev. Lett. **100**, 096407 (2008).

[212] L. Fu and C. L. Kane, Phys. Rev. B **79**, 161408 (2009).

[213] A. Cook and M. Franz, Phys. Rev. B **84**, 201105 (2011).

[214] H.-H. Sun, K.-W. Zhang, L.-H. Hu, C. Li, G.-Y. Wang, H.-Y. Ma, Z.-A. Xu, C.-L. Gao, D.-D. Guan, Y.-Y. Li, C. Liu, D. Qian, Y. Zhou, L. Fu, S.-C. Li, F.-C. Zhang, and J.-F. Jia, Phys. Rev. Lett. **116**, 257003 (2016).

[215] H. Zhang, C.-X. Liu, S. Gazibegovic, D. Xu, J. A. Logan, G. Wang, N. Van Loo, J. D. Bommer, M. W. De Moor, D. Car, *et al.*, Nature **556**, 74 (2018).

[216] J. Alicea, Y. Oreg, G. Refael, F. Von Oppen, and M. P. A. Fisher, Nature Physics **7**, 412 (2011).

[217] A. Kitaev, Annals of Physics **321**, 2 (2006).

[218] I. Affleck, A. Rahmani, and D. Pikulin, Phys. Rev. B **96**, 125121 (2017).

[219] C.-Y. Hou, C. Chamon, and C. Mudry, Phys. Rev. Lett. **98**, 186809 (2007).

[220] C. Chamon, C.-Y. Hou, R. Jackiw, C. Mudry, S.-Y. Pi, and G. Semenoff, Phys. Rev. B **77**, 235431 (2008).

[221] T. Iadecola, T. Schuster, and C. Chamon, Phys. Rev. Lett. **117**, 073901 (2016).

[222] F. D. M. Haldane, Phys. Rev. Lett. **61**, 2015 (1988).

[223] C. Chamon, Phys. Rev. B **62**, 2806 (2000).

[224] S. Ryu, C. Mudry, C.-Y. Hou, and C. Chamon, Phys. Rev. B **80**, 205319 (2009).

[225] M. F. Atiyah and I. M. Singer, Bulletin of the American Mathematical Society **69**, 422 (1963).

[226] R. Jackiw and P. Rossi, Nucl. Phys. B **190**, 681 (1981).

[227] E. J. Weinberg, Phys. Rev. D **24**, 2669 (1981).

[228] C.-K. Chiu, J. C. Y. Teo, A. P. Schnyder, and S. Ryu, Rev. Mod. Phys. **88**, 035005 (2016).

[229] S. Nadj-Perge, I. K. Drozdov, B. A. Bernevig, and A. Yazdani, Phys. Rev. B **88**, 020407 (2013).

[230] S. Nadj-Perge, I. K. Drozdov, J. Li, H. Chen, S. Jeon, J. Seo, A. H. MacDonald, B. A. Bernevig, and A. Yazdani, Science , 1259327 (2014).

[231] M. Ruby, F. Pientka, Y. Peng, F. von Oppen, B. W. Heinrich, and K. J. Franke, Phys. Rev. Lett. **115**, 197204 (2015).

[232] D. Chevallier and J. Klinovaja, Phys. Rev. B **94**, 035417 (2016).

[233] M. J. Yoo, T. A. Fulton, H. F. Hess, R. L. Willett, L. N. Dunkleberger, R. J. Chichester, L. N. Pfeiffer, and K. W. West, Science **276**, 579 (1997).

[234] J. Li, T. Neupert, B. A. Bernevig, and A. Yazdani, Nat. Commun. **7**, 10395 (2016).

[235] P.-Y. Chang, X. Chen, S. Gopalakrishnan, and J. Pixley, arXiv preprint arXiv:1811.00029 (2018).

[236] T. Rakovszky, S. Gopalakrishnan, S. Parameswaran, and F. Pollmann, arXiv preprint arXiv:1901.04444 (2019).

[237] Z.-C. Yang, A. Rahmani, A. Shabani, H. Neven, and C. Chamon, Phys. Rev. X **7**, 021027 (2017).

[238] M. Bukov, A. G. R. Day, D. Sels, P. Weinberg, A. Polkovnikov, and P. Mehta, Phys. Rev. X **8**, 031086 (2018).

[239] A. G. R. Day, M. Bukov, P. Weinberg, P. Mehta, and D. Sels, Phys. Rev. Lett. **122**, 020601 (2019).

[240] L. Zhou, S.-T. Wang, S. Choi, H. Pichler, and M. D. Lukin, arXiv preprint arXiv:1812.01041 (2018).

[241] W. W. Ho and T. H. Hsieh, arXiv preprint arXiv:1803.00026 (2018).

[242] W. W. Ho, C. Jonay, and T. H. Hsieh, arXiv preprint arXiv:1810.04817 (2018).

[243] Z.-C. Yang, T. Iadecola, C. Chamon, and C. Mudry, arXiv preprint arXiv:1808.04825 (2018).

[244] P.-H. Huang, J.-H. Chen, P. R. S. Gomes, T. Neupert, C. Chamon, and C. Mudry, Phys. Rev. B **93**, 205123 (2016).

[245] P.-H. Huang, J.-H. Chen, A. E. Feiguin, C. Chamon, and C. Mudry, Phys. Rev. B **95**, 144413 (2017).

[246] J.-H. Chen, C. Mudry, C. Chamon, and A. M. Tsvelik, Phys. Rev. B **96**, 224420 (2017).

[247] T. Iadecola, T. Neupert, C. Chamon, and C. Mudry, Phys. Rev. B **93**, 195136 (2016).

[248] T. Iadecola, T. Neupert, C. Chamon, and C. Mudry, arXiv preprint arXiv:1703.03418 (2017).

[249] Y. Plotnik, M. C. Rechtsman, D. Song, M. Heinrich, J. M. Zeuner, S. Nolte, Y. Lumer, N. Malkova, J. Xu, A. Szameit, *et al.*, Nat. Mater. **13**, 57 (2014).

[250] Y. Hu and C. L. Kane, Phys. Rev. Lett. **120**, 066801 (2018).

CURRICULUM VITAE